University of South Wales
2064870

Bound by
ABBEY BOOKBINDING & PRINTING
Unit 3 Gabalfa Workshops Excelsior Ind. Est. Cardiff CF14 3AY
Tel: (029) 2062 3290 Fax: (029) 2062 5420
Email: info@abbeybookbinding.co.uk
Web: www.abbeybookbinding.co.uk

University of South Wales

Numerical Modelling of Plasmonic Waveguides

Ahmed Mahmoud El-Dsoky Saleh Heikal

A submission presented in partial fulfilment of the requirements of the
University of Glamorgan/Prifysgol Morgannwg

for the degree of Doctor of Philosophy

June 2013

UNIVERSITY OF • PRIFYSGOL
Glamorgan
Morgannwg
CARDIFF • PONTYPRIDD • CAERDYDD

Graduate Research Office
Swyddfa Ymchwil Graddedigion

R10

Approval for Submission of a Thesis

Student Name: Ahmed Mahmoud El-Dsoky Saleh Heikal

Award: PhD

This is to confirm that the thesis entitled:

Numerical Modelling of Plasmonic Waveguides

has been approved for submission by the student's supervisory team and can therefore be forwarded to the examiners.

Signed ....

Director of Studies

Date *01-05-2013*

R11

Certificate of Research

This is to certify that, except where specific reference is made, the work described in this thesis is the result of the candidate's research. Neither this thesis, nor any part of it, has been presented, or is currently submitted, in candidature for any degree at any other University.

Signed Ahmed Heikal ....
Candidate

Date *01-05-2013*

Signed ....
Director of Studies

Date *01-05-2013*

Table of Contents

Acknowledgements

In the name of ALLAH, the most Beneficent, the most Merciful, the most Compassionate.

I would like to express my gratitude to my thesis supervisor Prof. S. S. A. Obayya, whose mentorship and support made my graduate career a truly remarkable experience. Despite his busy schedule, he has always made time for discussion. In addition to the scientific side, he has also provided me with invaluable help in carefully planning and managing the different steps of my research. I have truly learned a lot during my PhD.

I would like to express my warm thanks to Dr. Mohamed Farahat for his continuous and invaluable guidance. I shall always remember him for his kindness and all the support that he has given me through my study.

I am forever indebted to the greatest man in my life, my beloved father, whose unconditional love and support at each time of my life made me that man that I am today. His deep faith, his prayers, and supreme trust are always the most efficient motivation to accomplish my ultimate goal. No word can describe what you have done for me. Thank you for your selfless and endless love.

My beloved, my wife, Sahar, her prayers, patience, hard work, energy, dedication, enthusiasm, passion, support, and, most of all, her love; to these I owe where I stand today.

To my lovely rose, my daughter Layan, who has decorated my life and made it full of happiness and joy.

I wish to mention all my other brothers and sister, who have all had a great influence in keeping me motivated throughout this PhD journey, when things made no sense, they made the PhD life look all the brighter and gave me the extra push when I needed one.

Lastly, I would like to offer my regards and blessing to all of those who supported me in any respect during the completion of this work as well as expressing my apologies that I could not mention them personally one by one.

To my lovely home country Egypt

Abstract

Plasmonics play an essential role now in the area of compact on chip optical systems; this is due to their unique characteristics and the ability of guiding light below the diffraction limit. Moreover, the integration between optical systems and electronic systems can be realised using those nanostructures. Since the advent of these devices, there is an urgent need to have an accurate numerical model for plasmonic structures. Numerical simulations play an important role for the design and modeling of plasmonics. In this thesis, the conventional full vectorial finite difference method (FVFDM) and a nine node based full vectorial finite difference method for linear oblique and curved interfaces (FVFDM-LOCI) are used.

In this dissertation, new plasmonic structures for manipulating light at the nanoscale are explored. The modal analysis of a novel design of three trenched single mode channel plasmon polaritons is introduced and analysed using the full-vectorial finite difference method for linear oblique and curved interfaces. The analysed parameters are the real effective index, propagation length, and lateral mode radius r_{3dB}. In addition, the figure of merit (FOM), defined as the ratio between propagation length and lateral mode radius, is also studied. The analysis is performed for different channel plasmon polariton (CPP) waveguides; trenched-groove, V-groove and the suggested three trenched structure over a specific spectral range (200 – 550 THz). The selected frequency band is chosen to ensure the existence of the CPP fundamental mode. The reported design offers a very high FOM at a low frequency band of (200-350 THz) compared to the well-known V-groove structure. However, the lateral mode radius r_{3dB} of the suggested three trenched structure is slightly smaller than that of the V-groove structure. For a high frequency band of (350 – 550 THz), the FOM is still higher than that of the V-groove structure while the lateral mode radius r_{3dB} is slightly greater than that of the V-groove structure.

Moreover, the modal analysis of a novel design of hybrid long-range plasmonic waveguide is introduced and analysed using the full-vectorial finite difference method as well. The analysed parameters are the real effective index, propagation length, and coupling loss. In addition, the bending analysis of that waveguide has been included. The coupling has been performed between three different waveguides. A straight dielectric waveguide couples through a straight hybrid long-range plasmon waveguide to a uniformly bent hybrid one. Using the high index materials as a cap for the hybrid waveguides reduce the propagation loss and optimum bending radius as well.

List of Figures

List of Abbreviations

1D	One Dimension
2D	Two Dimensions
3D	Three Dimension
Ag	Silver
Au	Gold
BCB	Benzocyclobutene
DMD	Dielectric Metal Dielectric
EM	Electromagnetic
FD	Frequency Domain
FDFD	Finite Difference Frequency Domain
FDM	Finite Difference Method
FDTD	Finite Difference Time Domain
FEM	Finite Element Method
FVFD	Full Vectorial Finite Difference Method
FVFD-LOCI	Full Vectorial Finite Difference Method for Linear Oblique and Curved Interface
FOM	Figure Of Merit
p-SP	Propagating Surface Plasmon

IDBPM	Imaginary Distance Beam Propagation Method
IMI	Insulator-Metal-Insulator
l-SP	Localized Surface Plasmon
LRSP	Long Range Surface Plasmon
MDM	Metal Dielectric Metal
MIM	Metal-Insulator-Metal
PML	Perfect Matching Layer
Si	Silicon
SP	Surface Plasmon
SRSP	Short Range Surface Plasmon mode
SPP	Surface Plasmon Polariton
SiO_2	Silicon Dioxide
SOI	Silicon On Insulator
TD	Time Domain
TM	Transverse Magnitic Mode
TE	Transverse Electric Mode

Chapter 1

Introduction

1.1 Introduction

The development of information technology increases the need for faster information processing. Since the invention of the transistor, the new area of silicon electronics technology has appeared, and our data-hungry society continuously drives electronic devices to become smaller, faster, and more efficient. However, further increases in electronic processing speed are at present limited by delays depending on electronic interconnections [1, 2]. Because of this, the integration of modern electronic devices for information processing is rapidly reaching a fundamental speed limitation.

However, the photon velocity is much higher than that of an electron in a dielectric material. Conventional photonic devices cannot be integrated as densely as their electronic peers. In fact, the diffraction limit of light in dielectric media for conventional dielectric devices does not allow light to be confined in a region smaller than the wavelength of light. Consider an air-silicon-air dielectric slab waveguide (Fig. 1.1). Such a wave guiding structure always supports a fundamental optical mode for any silicon core thickness. When the thickness of the silicon core w is ~ $0.68\lambda_0/n$, the fundamental mode can be effectively guided in such a waveguide. In other words, the modal field is highly confined in the silicon core. Here, λ_0 is the free-space wavelength, and n is the refractive index of silicon.

If the thickness w decreases, the fundamental guided mode starts to go out into the surrounding air cladding region (Fig. 1.1). Therefore, decreasing the core thickness of the waveguide does not lead to sub wavelength guiding of the optical mode.

It is clear from Fig. 1.1 that the restriction comes with the diffraction limit of light in conventional dielectric waveguides, and reveals that the problem appears when attempting to reach chip-scale integration of optical devices. Therefore, traditional dielectric waveguides cannot act as highly-compact waveguides. Moreover, the large size mismatch between electronic and optical devices indicates that there is no way to integrate these two technologies in the same chip. In short, the speed of electronics is limited by delays of electrons, whereas the dense integration of traditional dielectric devices is restricted by the diffraction limit.

Therefore, the information processing needs the development of a new generation of devices those combine the size of nanoscsale electronics and the speed of photonics, and thus breakdown the gap between nanoscale electronics and mircoscale photonics. The most efficient way to overcome the diffraction limit and confine light into nanoscale regions much smaller than the wavelength of light is to use materials with negative dielectric permittivity, such as metals. More specifically, the interface between a metal and a dielectric supports the so-called surface plasmon-polariton (SPP) modes. These SPPs are electromagnetic waves coupled to the collective oscillations of the electron plasma in the metal [3]. When the operating frequency reaches the surface plasmon frequency, the field profile of these modes is highly confined in a deep subwavelength region at the metal-dielectric interface. Therefore, plasmonics guide light at the nanosacle, and could perfectly solve the technical difficulties mentioned previously. Plasmonics could provide ultra-fast and ultra-compact optical waveguides.

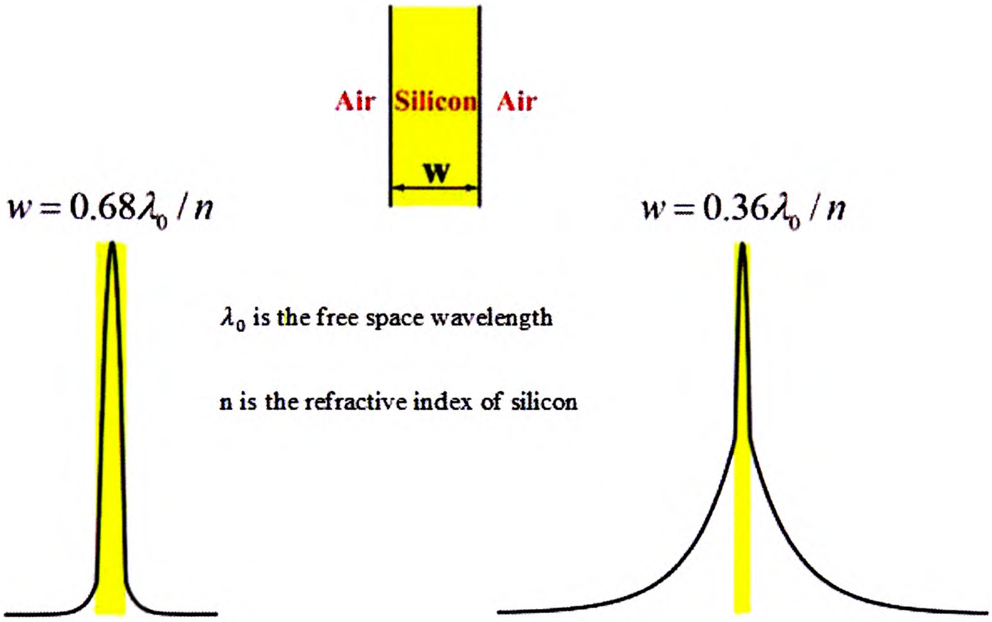

Figure 1.1 Shows the air-silicon-air dielectric slab waveguide.

Different plasmonic applications have been presented. Near-field scanning optical microscopy (NSOM) is one of most early plasmonic applications. Plasmonic devices also include the invention of plasmonic structures that support SPP modes, like nanogaps drilled in metal [4], arrays of nanometallic particles [5, 6], metal grooves [7, 8], metal wedges [9, 10], and metal-insulator-metal (MIM) waveguides [11]. Among these, MIM plasmonic waveguides attract great interest because they support modes with deep subwavelength scale over a very wide range of frequencies from DC to visible [4].

1.2 Motivation

The novel characteristics of surface plasmons enable a wide range of practical applications [12-15]. This provides compact photonic circuits that have a size much smaller than those presented in [13, 14]. Using metallic nanostructures to manipulate light at nanometric length scales has opened huge opportunities.

Plasmonic is used in subwavelength optics, data storage, light generation, microscopy and biophotonics [12-14]. However, exploration of functional nanoplasmonic structures and devices, including active plasmonic devices, is still in a very early stage. The realisation of such devices would enable, for the first time, controlling light and enhancing light-matter interactions at the nanoscale, beyond the diffraction limit. This would be fundamentally impossible to achieve with dielectric-based device components. This in turn would have profound implications for computing, communications, and energy applications. The development of these nanoscale devices and their integration will be challenging. It is therefore important to theoretically and computationally explore this area and to identify the most promising structures for specific device applications such as sensing and switching.

1.3 Aim and Objectives

The aim of this work is to create a novel accurate and numerically efficient Full Vectorial Finite Difference (FVFD) for linear oblique and curved interfaces mode solver. This mode solver is to analyse the challenging surface plasmon waveguides. To achieve this aim, the following objectives have been set:

a. Develop a novel graded nonuniform orthogonal mesh that enables accurate meshing of very thin metal nanostructures that require very fine mesh, embedded in dielectric microstructures.

b. Develop a full-vectorial finite difference mode solver that can deal with linear oblique and curved interfaces.

c. Investigate the ability of the mode solver to deal with plasmonic structures and calculate different nanostructures' parameters such as; electromagnetic field component, effective index n_{eff}, propagation length L_{prop} and attenuation.

d. Study bent plasmonic waveguides, obtain the bending loss in that structure and calculate the optimum bending radius at which minimum bending loss occurs.

e. Study coupling mechanism between the plasmonic waveguide and conventional dielectric waveguide.

f. Present a novel plasmonic waveguide that enable guiding light in subwavelength region based on metal grooves and has good confinement and moderate loss.

g. Present a novel hybrid plasmonic waveguide with a small bending radius that will be a promising device for compact optical systems.

1.4 Outline of The Thesis

The remainder of this thesis is organised as follows. In Chapter 2, the basic concept concerning the surface plasmon phenomena is presented. In Chapter 3, the finite-difference frequency-domain technique and its application in simulating plasmonic devices has been discussed. In Chapter 4, nonuniform meshing techniques for plasmonic waveguides have been discussed. In Chapter 5, a novel channel plasmon polariton based on a three-trenched groove waveguide is introduced. In Chapter 6, a novel hybrid long-range plasmonic waveguide including bends is presented and the coupling characteristic is studied. Finally, in Chapter 7, I summarise my conclusions, and provide suggestions for future work.

1.5 Contributions to Knowledge

The contributions of this work to knowledge can be summarised as follow:

1) Develop a novel full vectorial finite difference method for linear oblique and curved interface that can overcome the staircase problem that appears with the conventional finite difference method. This is necessary to decrease the numerical modelling error that appears from staircase meshing for oblique and curved interfaces.
2) Develop a novel graded mesh that can be used to model nano metallic structures embedded in micro dielectric materials. This graded mesh provides very fine mesh at metal/dielectric interface while mesh size increases gradually when

moving away from the interface. Graded mesh enables using less mesh points and therefore, reduces the computational time.

3) Present a novel plasmonic channel waveguide called the three trenched groove plasmonic waveguide. This structure can confine light as good as the famous V-groove while it has a better propagation length. This waveguide can be used in optical switches, interferometers and optical interconnectors.
4) Present a novel hybrid plasmonic waveguide that can be bent into a small radius with low damping metallic loss. Such a device would be essential for the integration process between traditional dielectric waveguide and electronic devices.

1.6 List of Publication

Journal Papers

1- A. M. Heikal, M. F. O. Hameed, S. S. A. Obayya, "Improved Trenched Channel Plasmonic Waveguide", accepted for publication in IEEE J. Lightwave Technology.

2- A. M. Heikal, M. F. O. Hameed, S. S. A. Obayya, "Coupling Characteristic for Novel Hybrid Long-Range Plasmonic Waveguide including Bends", accepted for publication in IEEE Journal of Quantum Electronics.

Conference Papers

1- A. M. Heikal, M.F.O. Hameed, S.S.A.Obayya,"Accurate Finite Difference Analysis of Novel Trenched Channel Plasmonic Waveguides " presented at MTA'13, the 4th International Conference on Metamaterials, Photonic Crystals and Plasmonics, 18-22 March 2013, Sharjah, United Arab Emirates.

2- A. M. Heikal, M.F.O. Hameed, S.S.A.Obayya, '' Coupling characteristic for novel hybrid long-range plasmonic waveguide including bends '' presented at OWTNM'XXI, the 21th international Workshop on Optical Wave and Waveguide Theory and Numerical Modelling, 19-20 April 2013, Enschede, The Netherlands.

Chapter 2

Surface Plasmon Waveguides

2.1 Definition of Plasmonics

`Plasmonics' is a relatively new term in photonics which refers to applications or phenomena in which the surface plasmons (SP) is introduced [3, 12]. SPs can be defined as the interaction of surface electrons of metals with electromagnetic waves. However, the difference between the characteristics of surface electrons and those in the bulk of metals has been known for a long time, only recently have the surface plasmons phenomena attracted the attention of scientist and engineers from varying disciplines. The Great development in technology enables the fabrication and implementation of nano-metallic structures. SPs are of either propagating or localised type.

2.1.1 Propagating Surface Plasmons (p-SPs)

The optical field is confined in higher refractive index region in dielectric waveguides. Surface plasmons travel along dielectric and metal interfaces. For a planar interface of a metal and a dielectric the electromagnetic field is confined at the interface [16]. The field decays exponentially in both metal and dielectric in the direction perpendicular to the interface. The interfaces can be complicated geometries or even be periodic (grating). For certain geometries the electromagnetic field of surface plasmon waveguides can be confined in a few nanometres. An example is a very thin dielectric film embedded between metal claddings (Metal-Insulator-Metal MIM structure) [17]. Since electromagnetic field components decay in metal much faster than in dielectric, the effective thickness of this type of waveguide is just a few nanometres. Moreover, dielectric waveguides have a fundamental limit for the mode size, the diffraction limit. The diffraction limit principle states that the dimensions of optical mode of a dielectric waveguide cannot be smaller than half the wavelength in the core [18]. However, SP waveguides led to more compact optical systems instead of the conventional dielectric waveguides.

2.1.2 Localised Surface Plasmons (l-SPs)

If light is incident on a metallic nanoparticle, free electrons of the nanoparticle respond to the electromagnetic field. When the diameter of the particle is much smaller than the wavelength of field, the free electrons move in phase and oscillate with a certain frequency. This frequency depends on the shape, size and material of the particle. Moreover, the properties of the surrounding cladding and the wavelength of the exciting light have a great effect on the oscillation of these free electrons. The electric dipole model can be used to implement theoretically, the electron oscillation over a very small localised distance. Energy builds up in the dipole field to a level that the near field of the dipole could be enhanced by several orders of magnitude compared to the exciting field. The confinement of free electrons to a very small volume leads to electromagnetic field enhancement. This phenomenon is the main idea for a number of applications including single molecule detection [19], microscopy [20] and small particle manipulation [5]. The nanoparticle strong near field encourages nonlinear effects that can be used for novel applications such as all optical switching.

When metallic nanoparticles are arranged close enough to interact with each other. Each particle can be modelled by an electric dipole that couples to the next one. A single dimensional array of particles has been used as a waveguide [21] with a very small cross section. Sharp bends have also been presented [22]. Two dimensional arrays of particles can be adjusted to form gratings with different capabilities [23].

2.2 Single-Interface Surface Plasmon Waveguide

Consider two different dielectrics as shown in Fig. 2.1.

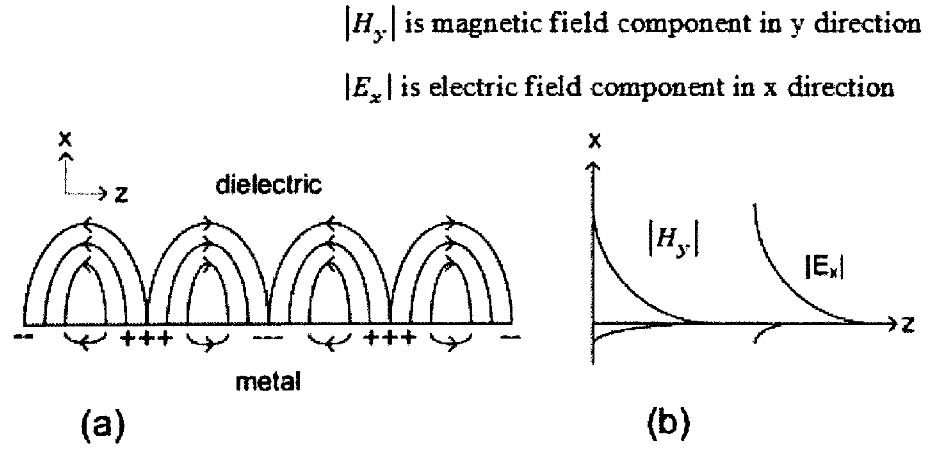

Figure 2.1 (a) Single interface SPWG schematic showing the electric field lines. (b) Amplitudes of magnetic and normal electric fields above and below the interface indicating the penetration depth in each region.

Using Maxwell equations (Appendix A.1 and A.2 in appendix), by assuming a sinusoidal plane-wave ($\partial/\partial t = j\omega$) with no charge ($\rho = 0$), no current ($J = 0$) and $\partial/\partial y = 0$

$$\nabla \times E = -j\omega\mu H \tag{2.1}$$

$$\nabla \times H = j\omega\varepsilon E \tag{2.2}$$

decouple equations (2.1) and (2.2) into two sets of equations

Transverse Electric (TE) mode (no z component for the electric field):

$$\frac{\partial E_y}{\partial z} = j\omega\mu H_x \tag{2.3}$$

$$\frac{\partial E_y}{\partial x} = -j\omega\mu H_z \tag{2.4}$$

$$\frac{\partial H_x}{\partial z} - \frac{\partial H_z}{\partial x} = j\omega\varepsilon E_y \tag{2.5}$$

Transverse Magnetic (TM) mode (no z component for the magnetic field):

$$\frac{\partial H_y}{\partial z} = -j\omega\varepsilon E_x \tag{2.6}$$

$$\frac{\partial H_y}{\partial x} = j\omega\varepsilon E_z \tag{2.7}$$

$$\frac{\partial E_x}{\partial z} - \frac{\partial E_z}{\partial x} = -j\omega\mu H_y \tag{2.8}$$

In the TE case for a guided mode with propagation constant β we separate the z coordinate dependence as

$$\mathrm{E}_y(x,z) = E_y(x)e^{-j\beta z} \tag{2.9}$$

Equations (2.3) to (2.5) result in the wave equation

$$\frac{d^2E_y}{dx^2} + (\omega^2\mu\varepsilon - \beta^2)E_y = 0 \tag{2.10}$$

The solutions to the wave equation are exponential functions. Considering that a physical solution cannot contain unbounded growth as distance increases from the interface [16] then

$$E_y = \begin{cases} A_1 e^{-k_{x1}x} \ , & x > 0 \\ A_2 e^{-k_{x2}x} \ , & x < 0 \end{cases} \tag{2.11}$$

where A_1 and A_2 are constants and k_x is the x component of the wave vector given by

$$\beta^2 - k_{x\,1,2}^2 = \omega^2\mu\varepsilon_0\varepsilon_{1,2} \tag{2.12}$$

The interface conditions rule that E_y and H_z (or equivalently $\frac{\partial E_y}{\partial x}$) must be continuous at x = 0. The first condition leads to $A_1 = A_2$ which makes the second condition unsatisfiable. This means that a single planar interface between two media cannot support TE modes. For the case of TM waves, however, things turn out to be different. Here we have

$$\frac{d^2H_y}{dx^2} + (\omega^2\mu\varepsilon - \beta^2)H_y = 0 \tag{2.13}$$

with the solution

$$H_y = \begin{cases} A_1 e^{-k_{x1}x} \ , & x > 0 \\ A_2 e^{-k_{x2}x} \ , & x < 0 \end{cases} \tag{2.14}$$

with $k_{x\ 1,2}$ given by (2.12). Interface conditions demand H_y and $\frac{1}{\varepsilon}\frac{\partial H_y}{\partial x}$ be continuous across the interface leading to $A_1 = A_2$ and

$$\frac{k_{x1}}{\varepsilon_1} = -\frac{k_{x2}}{\varepsilon_2} \tag{2.15}$$

First, we notice that (2.15) requires ε_1 and ε_2 have different signs (if they are real). Using (2.12) in (2.15) we find the dispersion equation

$$\beta = k_0 \left(\frac{\varepsilon_1 \varepsilon_2}{\varepsilon_1 + \varepsilon_2}\right)^{\frac{1}{2}} \tag{2.16}$$

where $k_0 = \omega\sqrt{\mu\varepsilon_0}$, wave number of vacuum is used. In practice ε_1 is commonly a dielectric material with small or negligible loss and $\varepsilon_2 = \varepsilon_2' - j\varepsilon_2''$ is a metal with $\varepsilon_2' < 0$ and $|\varepsilon_2'| > \varepsilon_2''$. In this case real and imaginary parts of the propagation constant in (2.16) can be written as [16]

$$\beta' = k_0 \left(\frac{\varepsilon_1 \varepsilon_2'}{\varepsilon_1 + \varepsilon_2'}\right)^{\frac{1}{2}} \tag{2.17}$$

$$\beta'' = k_0 \left(\frac{\varepsilon_1 \varepsilon_2'}{\varepsilon_1 + \varepsilon_2'}\right)^{\frac{3}{2}} \frac{\varepsilon_2''}{2(\varepsilon_2')^2} \tag{2.18}$$

For β' to be real we must have $|\varepsilon_1'| > \varepsilon_1''$. β'' is defined as the decay of the guided mode due to the loss of metal represented by ε_2''. In a metal and dielectric interface oscillation of free electrons of metal at the surface (surface plasmons) is the main reason of the guided SP mode. Electric field lines at the surface are shown in Fig. 2.1. Maximum of the field occurs at the interface and decays exponentially. If metal has no damping loss, the decay constant in the dielectric $k_{x1} < \beta$, but in the metal $k_{x2} > \beta$. This means that the fields decay faster in metal than they do in dielectric.

The dispersion of single interface surface plasmon waveguide for an interface between air and a metal is shown in Fig. 2.2. The dielectric permittivity of the lossless metal can be obtained from Drude model:

$$\varepsilon_2 = 1 - \left(\frac{\omega_p}{\omega}\right)^2 \tag{2.19}$$

in which ω_p is the plasma frequency for silver ($\omega_p = 2\pi \times 2.18 \times 10^{15} rad/s$). In the dielectric, the light line can be calculated by $\omega = \frac{kc}{n_d}$ where c is the speed of light in free space, k is the wavenumber in the dielectric and n_d is the dielectric refractive index. This line represented by a dotted line in Fig. 2.2. Due to momentum (k) mismatch, any field whose dispersion curve comes below the dotted line cannot propagate in that dielectric and is called non-radiative field. However, fields whose dispersion curves fall in the left side of light line can propagate into the dielectric region ('radiative' fields). The dispersion curve of single interface surface plasmon waveguide has two regions, the nonradiative zone and the radiative zone.

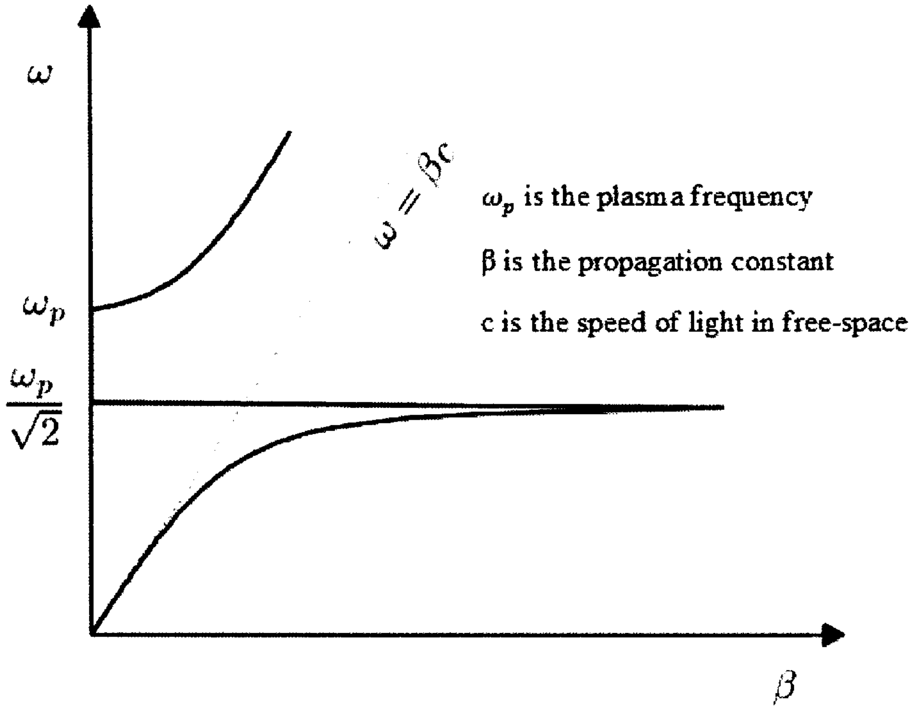

Figure 2.2 Shows the dispersion curve for single-interface surface plasmon waveguide

There is a discontinuity at $\omega = \frac{\omega_p}{\sqrt{2}}$ where $|\varepsilon_2| = \varepsilon_1 = 1$. In the ideal case (lossless) when frequency increases and reaches the discontinuity frequency propagation constant becomes very large and phase and group velocities approach zero. In the practical case (losses are included), the propagation constant is bounded and it reaches a maximum which depends on the loss value.

As mentioned before, the maximum of fields of the surface plasmon mode occurs at the interface and decays exponentially into the surrounding zone. Skin depth (x_d) can be defined as the distance at which the dominant field component approach 1/e times its maximum.

$$x_d = \begin{cases} \dfrac{1}{k_{x1}} = \dfrac{1}{k_0}\left(\dfrac{\varepsilon_1 + \varepsilon_2'}{-\varepsilon_1^2}\right)^{\frac{1}{2}} & , \quad x > 0 \\ \dfrac{1}{k_{x2}} = \dfrac{1}{k_0}\left(\dfrac{\varepsilon_1 + \varepsilon_2'}{-\varepsilon_2^2}\right)^{\frac{1}{2}} & , \quad x < 0 \end{cases} \tag{2.20}$$

At λ=1.55 µm, using equation (2.20) where $k_0 = \frac{2\pi}{\lambda}$ and ε_1, ε_2 can be obtained using the Drude model [14]. The skin depth in air (silver/air interface is considered) is x_{d1} = 2.66 µm however in silver it is x_{d2} = 22.82 nm. Therefore, the field expansion into the dielectric is over hundred times of that in metal.

The main disadvantage of the single interface surface plasmon waveguide is the very short propagation length due to metal loss. The imaginary part of the metal permittivity leads to a complex propagation constant and fields decrease exponentially by $\exp(-|\beta''|z)$. The propagation length can be defined as the distance by which the intensity of electromagnetic field attenuates to 1/e from its maximum value. However, intensity is proportional to $\exp(-2|\beta''|z)$, the propagation length is $L = \frac{1}{2|\beta''|}$ where $\beta''$is imaginary part of complex propagation constant. Also, $\alpha = 2|\beta''|$ is called the attenuation constant. For silver/air interface at the wavelength of 1.55 µm the propagation length is about 299 µm and the attenuation constant is 32 cm^{-1}. The very small propagation of field into the metal is enough to cause a large attenuation value that limits the application of single interface surface plasmon waveguide at visible and near infrared wavelengths.

2.3 Thin Metallic Film Surface Plasmon Waveguide

Now, consider the existence of guided modes for insulator-metallic-insulator (MIM) structure as shown in Fig. 2.3.

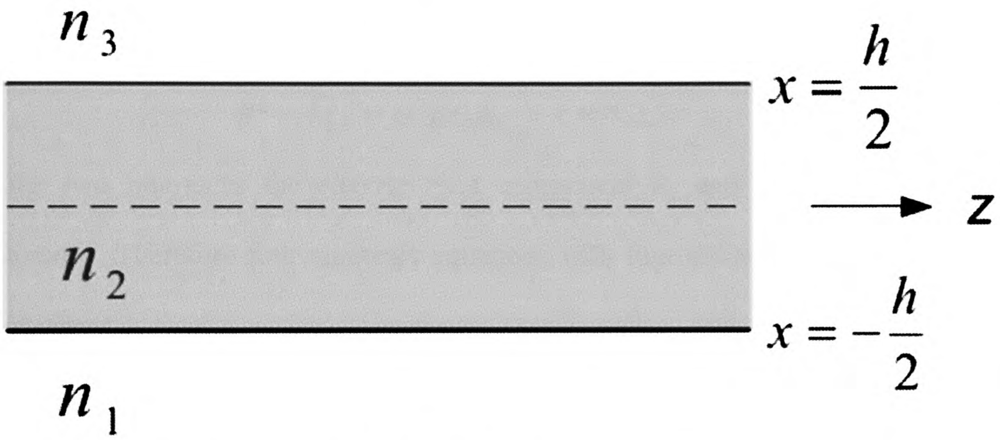

Figure 2.3 Shows thin film surface plasmon waveguide.

The film of thickness h is embedded between two dielectrics and z is the direction of propagation. Dielectrics in zones 1 and 3 have refractive indices n_1 and n_3, respectively. For the TE mode, the solution to the eigenvalue equation (2.10), applying the radiation boundary condition for regions 1 and 3 is [24]

$$E_y = \begin{cases} A_1 e^{k_{x1} x} & x \leq -\frac{h}{2} \\ A_2 \cosh(k_{x2} x) + A_3 \sinh(k_{x2} x) & \frac{-h}{2} \leq x \leq \frac{h}{2} \\ A_4 e^{-k_{x3} x} & x \geq \frac{h}{2} \end{cases} \tag{2.21}$$

where A_1 to A_4 are constants and wavenumbers k_{x1}, k_{x2} and k_{x3} in the x direction are calculated, as before, from

$$\beta^2 - k_{x\,i}^2 = \omega^2 \mu \varepsilon_0 \varepsilon_i, \qquad i = 1,2,3 \tag{2.22}$$

At the two interfaces the electric field component E_y and its derivative must be continuous. Therefore four algebraic equations with four unknown constants A_1 to A_4 are obtained:

$$\begin{aligned} A_1 e^{-k_{x1}\frac{h}{2}} - \mathrm{A}_2 \cosh\left(-k_{x2}\frac{h}{2}\right) - \mathrm{A}_3 \sinh\left(-k_{x2}\frac{h}{2}\right) &= 0 \\ A_1 k_{x1} e^{-k_{x1}\frac{h}{2}} - \mathrm{A}_2 k_{x2} \sinh\left(-k_{x2}\frac{h}{2}\right) - \mathrm{A}_3 k_{x2} \cosh\left(-k_{x2}\frac{h}{2}\right) &= 0 \\ -A_4 e^{-k_{x3}\frac{h}{2}} + \mathrm{A}_2 \cosh\left(k_{x2}\frac{h}{2}\right) + \mathrm{A}_3 \sinh\left(k_{x2}\frac{h}{2}\right) &= 0 \\ A_4 k_{x1} e^{-k_{x3}\frac{h}{2}} + \mathrm{A}_2 k_{x2} \sinh\left(k_{x2}\frac{h}{2}\right) + \mathrm{A}_3 k_{x2} \cosh\left(k_{x2}\frac{h}{2}\right) &= 0 \end{aligned} \tag{2.23}$$

Since the equations are homogenous, in order to have nontrivial solutions for the constants, the determinant of the system of equations must be zero:

$$D = \begin{vmatrix} e^{-k_{x1}\frac{h}{2}} & -\cosh\left(-k_{x2}\frac{h}{2}\right) & -\sinh\left(-k_{x2}\frac{h}{2}\right) & 0 \\ k_{x1}e^{-k_{x1}\frac{h}{2}} & -k_{x2}\sinh\left(-k_{x2}\frac{h}{2}\right) & -k_{x2}\cosh\left(-k_{x2}\frac{h}{2}\right) & 0 \\ 0 & \cosh\left(k_{x2}\frac{h}{2}\right) & \sinh\left(k_{x2}\frac{h}{2}\right) & -e^{-k_{x3}\frac{h}{2}} \\ 0 & k_{x2}\sinh\left(k_{x2}\frac{h}{2}\right) & k_{x2}\cosh\left(k_{x2}\frac{h}{2}\right) & k_{x1}e^{-k_{x1}\frac{h}{2}} \end{vmatrix} = 0 \tag{2.24}$$

After simplification we have

$$\tanh(k_{x2}h)\left(1+\frac{k_{x1}k_{x3}}{k_{x2}^2}\right)+\left(\frac{k_{x1}}{k_{x2}}+\frac{k_{x3}}{k_{x2}}\right)=0 \tag{2.25}$$

or

$$\tanh(k_{x2}h)(1+s_1s_3)+(s_1+s_3)=0 \tag{2.26}$$

where

$$s_1=\frac{k_{x1}}{k_{x2}} \quad , \quad s_3=\frac{k_{x3}}{k_{x2}} \tag{2.27}$$

For lossless waveguides (neither metallic nor dielectric loss), where β is real and positive, there is no solution for eq. (2.26) for β. Therefore, TE guided modes cannot exist in a thin film surface plasmon waveguide.

Now, consider TM guided modes supported by the thin film structure. Here,

$$H_y = \begin{cases} A_1 e^{k_{x1}x} & x \leq -\frac{h}{2} \\ A_2 \cosh(k_{x2}x) + A_3 \sinh(k_{x2}x) & \frac{-h}{2} \leq x \leq \frac{h}{2} \\ A_4 e^{-k_{x3}x} & x \geq \frac{h}{2} \end{cases} \tag{2.28}$$

with the x-direction wavenumbers given by

$$\beta^2 - k_{x\,i}^2 = \omega^2 \mu \varepsilon_0 \varepsilon_i, \qquad i = 1,2,3 \tag{2.29}$$

Applying the boundary conditions at the two interfaces. These are the continuity of H_y and $\frac{1}{\varepsilon}\frac{dH_y}{dy}$ which generate four equations:

$$\begin{aligned} &A_1 e^{-k_{x1}\frac{h}{2}} - A_2\cosh\left(-k_{x2}\frac{h}{2}\right) - A_3\sinh\left(-k_{x2}\frac{h}{2}\right) && = 0 \\ &A_1\frac{k_{x1}}{\varepsilon_1}e^{-k_{x1}\frac{h}{2}} - A_2\frac{k_{x2}}{\varepsilon_2}\sinh\left(-k_{x2}\frac{h}{2}\right) - A_3\frac{k_{x2}}{\varepsilon_2}\cosh\left(-k_{x2}\frac{h}{2}\right) && = 0 \\ &-A_4 e^{-k_{x3}\frac{h}{2}} + A_2\cosh\left(k_{x2}\frac{h}{2}\right) + A_3\sinh\left(k_{x2}\frac{h}{2}\right) && = 0 \\ &A_4\frac{k_{x3}}{\varepsilon_3}e^{-k_{x3}\frac{h}{2}} + A_2\frac{k_{x2}}{\varepsilon_2}\sinh\left(k_{x2}\frac{h}{2}\right) + A_3\frac{k_{x2}}{\varepsilon_2}\cosh\left(k_{x2}\frac{h}{2}\right) && = 0 \end{aligned} \tag{2.30}$$

Setting the determinant of the above equations to zero brings us to the same dispersion equation given by (2.26) [24]:

$$\tanh(k_{x2}h)(1 + s_1 s_3) + (s_1 + s_3) = 0 \tag{2.31}$$

But with the following definition

$$s_1 = \frac{\varepsilon_2}{\varepsilon_1}\frac{k_{x1}}{k_{x2}}, \quad s_3 = \frac{\varepsilon_2}{\varepsilon_3}\frac{k_{x3}}{k_{x2}} \tag{2.32}$$

From this equation, s_1 and s_3 are negative real numbers. Therefore, the first term of (2.31) is positive, however, the second term is negative and hence there are solutions to that equation. Specifically, there are one or two solutions which relay on the structure parameters. Before considering the general case, we take a look at two special cases,

Case 1) Very thick film ($h \rightarrow \infty$)

From (2.31) as $k_{x2}h$ is very large, $\tanh(k_{x2}h)$ is replaced with unity. As a result, the equation becomes

$$(1 + s_1)(1 + s_2) = 0 \tag{2.33}$$

with the solution $s_1 = -1$ or $s_3 = -1$. Using (2.29) and (2.32) we obtain

$$\beta = k_0 \left(\frac{\varepsilon_1 \varepsilon_2}{\varepsilon_1 + \varepsilon_2}\right)^{\frac{1}{2}} \tag{2.34}$$

Or

$$\beta = k_0 \left(\frac{\varepsilon_3 \varepsilon_2}{\varepsilon_3 + \varepsilon_2}\right)^{\frac{1}{2}} \tag{2.35}$$

which are the dispersion relations for a single MI interface given in (2.16). Therefore, for a very thick metal film there are two independent surface plasmon modes at each interface. Each mode decays exponentially into the film, therefore, for very thick films; the two modes cannot be coupled. When the film becomes thinner coupling occurs and give rise to two `super modes' (see Fig. 2.2).

Case 2) Symmetric structure, ($\varepsilon_1 = \varepsilon_3$)

The dispersion equation (2.31) becomes

$$\tanh(k_{x2}h) = \frac{-2s_1}{1+s_1^2} \tag{2.36}$$

which after some algebraic manipulation changes to

$$\left(\tanh\left(\frac{k_{x2}h}{2}\right) + s_1\right)\left(s_1 \tanh\left(\frac{k_{x2}h}{2}\right) + 1\right) = 0 \tag{2.37}$$

giving two equations

$$\tanh\left(\frac{k_{x2}h}{2}\right) = -s_1 \tag{2.38}$$

$$\tanh\left(\frac{k_{x2}h}{2}\right) = -\frac{1}{s_1} \tag{2.39}$$

Fig. 2.4 shows symmetric and asymmetric modes in thin film surface plasmon waveguide formed by coupling of SPP modes. It is clear that by putting A_3 = 0 in the equation (2.30), equation (2.38) is obtained, which is the dispersion equation of a mode at A_3 = 0. This mode is a symmetric mode. However, eq. (2.39) is the dispersion relation of the asymmetric mode at A_2 = 0.

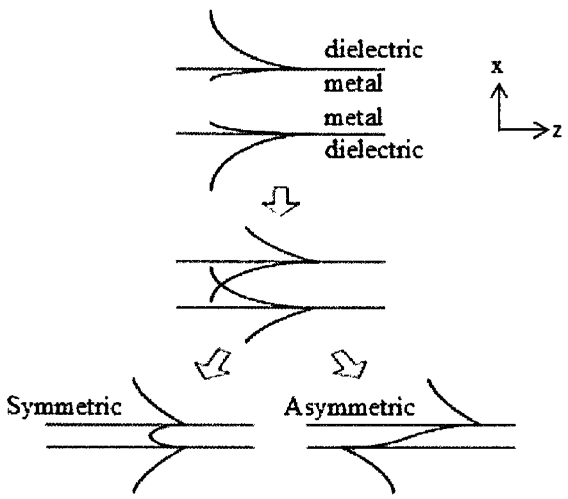

Figure 2.4 Shows symmetric and asymmetric modes in thin film surface plasmon waveguide.

Fig. 2.5 shows the effect of changing the film thickness on real and imaginary parts of the propagation constants of symmetric and asymmetric mode. However the values shown are the normalised to the free space wavenumber (the effective indices of guided modes). In the simulation we assumed, $\varepsilon_1 = \varepsilon_3 = 10.23$ and $\varepsilon_2 = -115.37\text{-}j11.14$ (dielectric constant of silver at λ=1550 nm, two decimal places is efficient to obtain accurate results [24]). At small metal thicknesses h, the real part of effective index of the symmetric mode converges to the refractive index of dielectric claddings. It is clear from the mode profile of the symmetric mode in Fig. 2.2; as the film thickness reaches zero the symmetric mode becomes similar to a plane wave propagating in the dielectric medium surrounding the film. Moreover, the symmetric mode loss which is proportional to the imaginary part of the effective index reaches zero. However, in asymmetric mode case, the real effective index increases unboundedly as film thickness decreases to zero. Therefore, the mode becomes more and more confined inside the film. The asymmetric mode cannot be supported by the dielectric region when film thickness approaches zero as the sign of H_y field component should be changed suddenly. Therefore, the asymmetric mode is compressed inside the film. It is clear that asymmetric mode loss is larger than that of the symmetric mode. The symmetric and asymmetric modes are also called long range and short range surface plasmon modes (LRSP and SRSP), respectively.

When the film thickness increases, propagation constants of the modes get closer and in the limit of thick film they degenerate, as previously explained.

Fig. 2.6 shows the frequency dispersion of the LRSP and SRSP modes for a 20 nm thick film embedded in dielectric materials of $\varepsilon_1 = \varepsilon_3 = 1$.

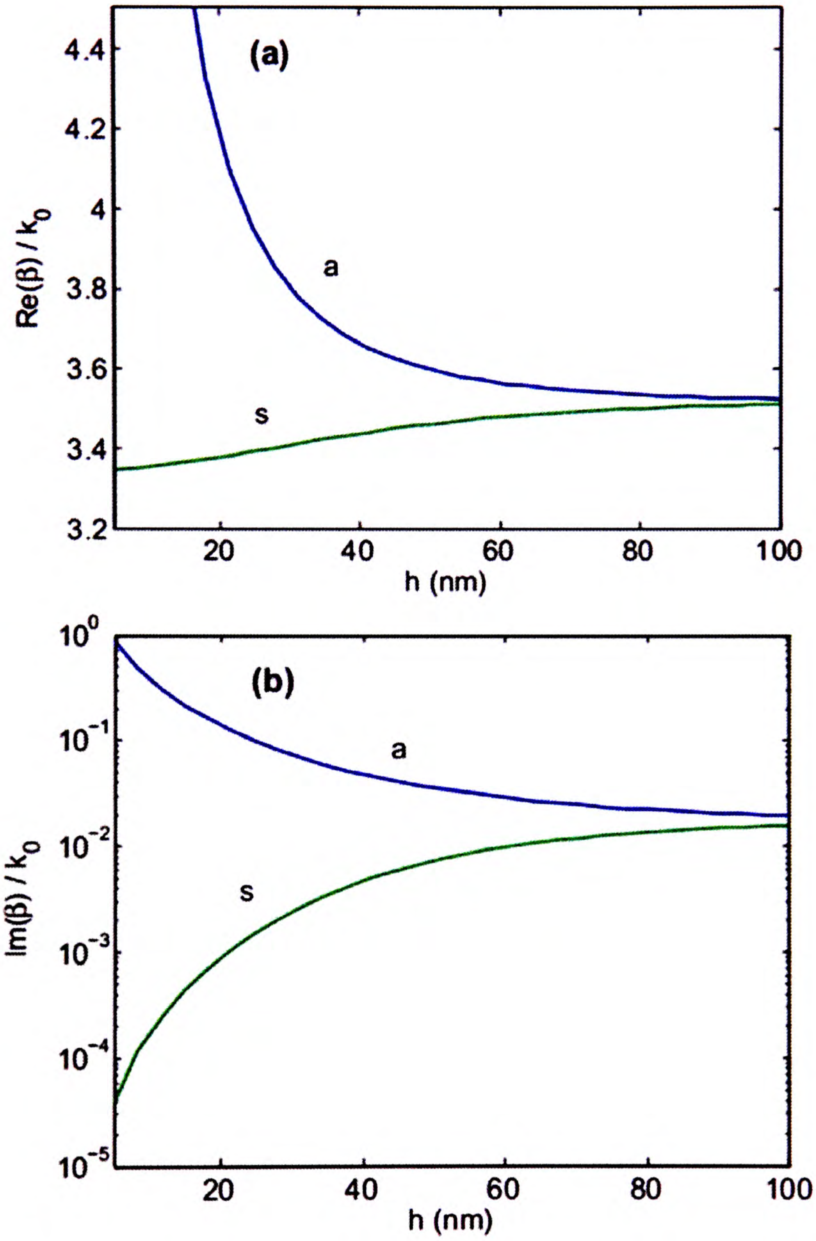

Figure 2.5 Shows the variation of propagation constant (a) Real part and (b) imaginary parts of the two modes of thin surface plasmon waveguide, symmetric (s curve) and asymmetric (a curve), with film thickness h.

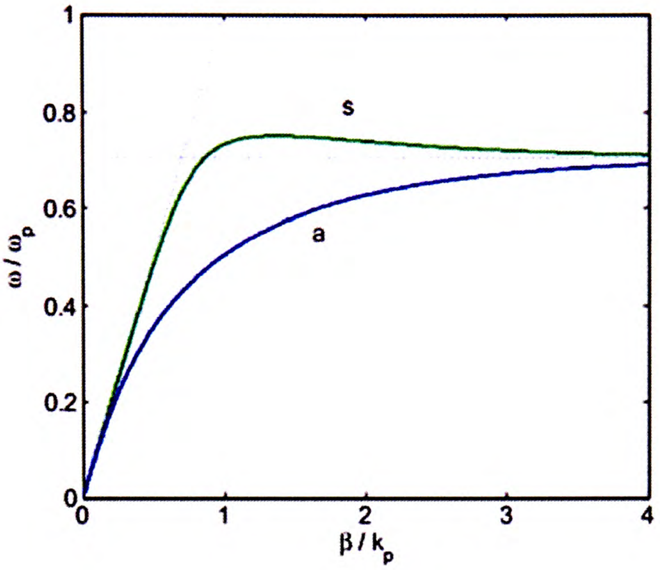

Figure 2.6 Shows the dispersion curves for symmetric and asymmetric modes of thin film SP waveguide.

(Drude) model is assumed for the dielectric constant of metal with a plasma frequency$\omega_p = 2\pi \times 2.19 \times 10^{15} rad/s$. Frequencies are normalised to the plasma frequency and propagation constants to the free space wavenumber at the plasma frequency (k_p). As the two modes are below the light line, they cannot travel in the dielectric zones and are bound to the metal interface. At large values of propagation constants the two modes become constant and reach a frequency called the surface plasmon frequency. It is clear that the dispersion equations (2.29) and (2.30). When $\beta \to \infty,\ tanh\left(\frac{k_{x2}h}{2}\right) \to 1$ and $s_1 \to \frac{\varepsilon_2}{\varepsilon_1}$ and both dispersion equations give $\omega_\infty = \frac{\omega_p}{\sqrt{1+\varepsilon_1}}$ which is the surface plasmon frequency of single interface surface plasmon waveguide. This is because at very large propagation constants the guided wavelength is very small and the film appears as a very thick to the modes.

In the general case of $\varepsilon_1 \neq \varepsilon_3$ the two modes are quasi symmetric and quasi asymmetric. Fig. 2.7 shows the mode profiles for an asymmetric structure with $\varepsilon_1 < \varepsilon_3$. The major difference between symmetric and asymmetric thin film surface plasmon waveguides is the existence of a cutoff film thickness for the symmetric mode in an asymmetric structure [24]. For metal films thinner than the cutoff value, the symmetric mode stops propagating. Similarly, there is a cutoff wavelength above which the symmetric mode stops propagating. Fig. 2.8 shows the real and imaginary parts of the propagation constant of an asymmetric surface plasmon waveguide. The parameters of the surface plasmon waveguide are similar to those used for Fig. 2.5 except that $\varepsilon_3 = 11$. At cutoff, if $\varepsilon_1 < \varepsilon_3$, the lateral wavenumber (k_x) in region 3 is zero applying (2.29) gives

$$\beta = k_0\sqrt{\varepsilon_3} \tag{2.40}$$

Therefore, for lossless dielectrics the propagation constant at cutoff is real. This is confirmed by Fig. 2.8, as waveguide loss drops dramatically near cutoff. Other lateral wavenumbers are obtained as follow:

$$k_{x1} = k_0(\varepsilon_3 - \varepsilon_1)^{\frac{1}{2}} \tag{2.41}$$

$$k_{x2} = k_0(\varepsilon_3 - \varepsilon_2)^{\frac{1}{2}} \tag{2.42}$$

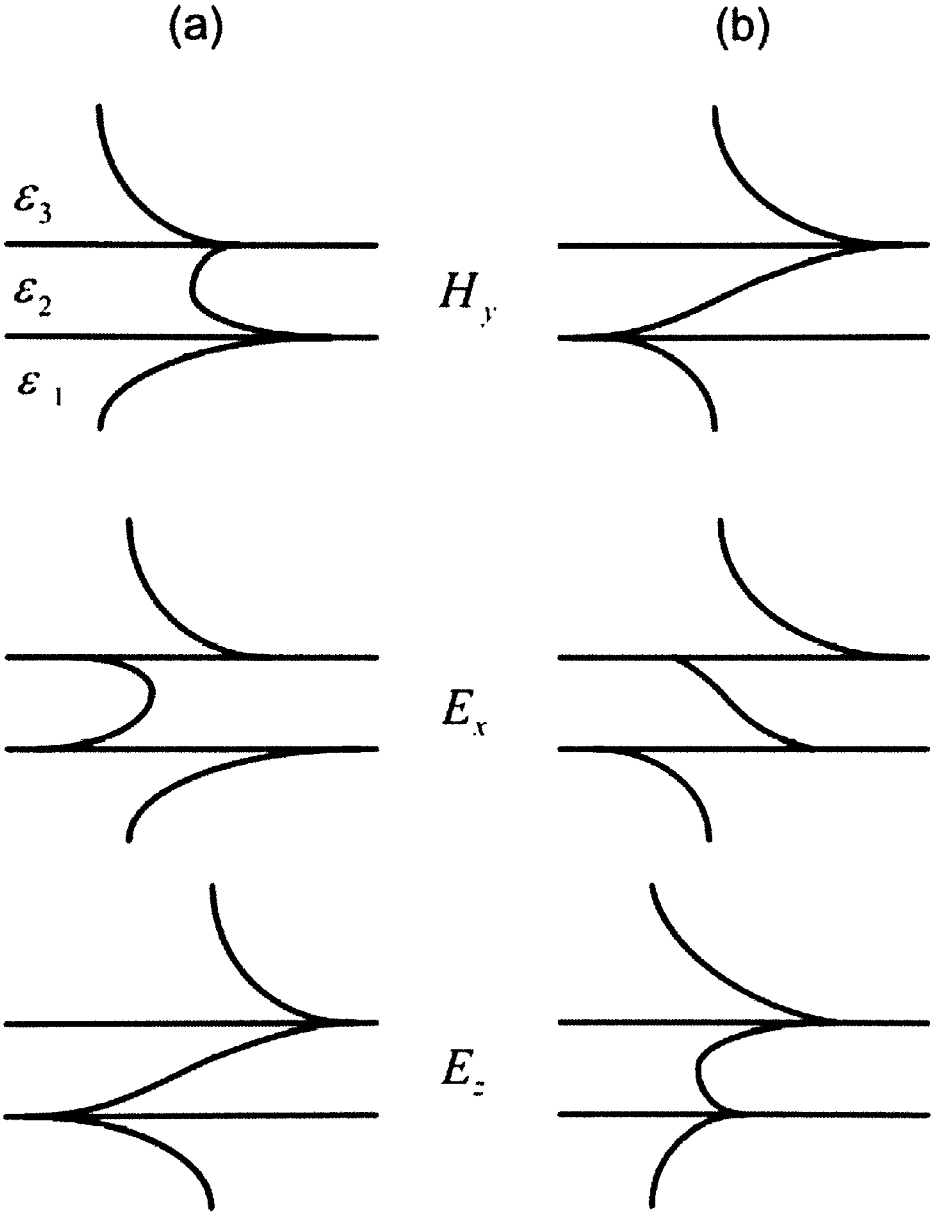

Figure 2.7 Shows (a) quasi symmetric mode and (b) quasi asymmetric mode for asymmetric thin film surface plasmon waveguide

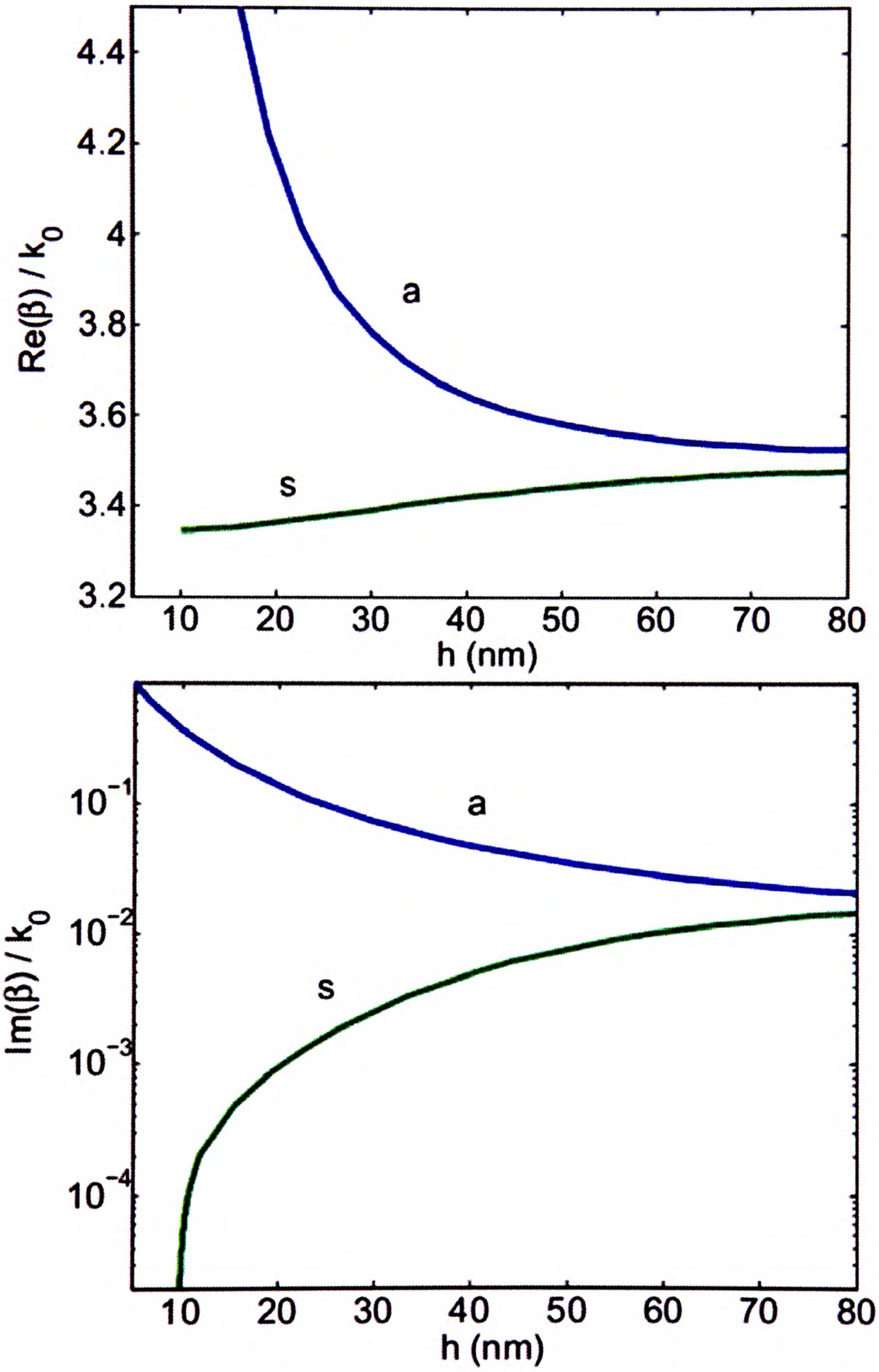

Figure 2.8 Shows the variation of propagation constant with thickness h for asymmetric film

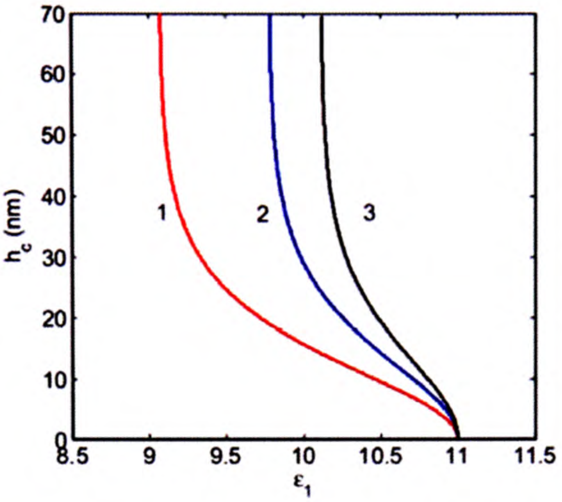

Figure 2.9 Shows the variation of the cutoff thickness h_c with the permittivity of the dielectric in region 1 for asymmetric thin film.

Using these relations in the dispersion equation (2.31) an analytical formula is obtained for the cutoff film thickness provided metal loss is neglected [27]

$$h_c = \frac{1}{2k_0(\varepsilon_3 - \varepsilon_2)^{\frac{1}{2}}} ln\left(\frac{\varepsilon_1(\varepsilon_3 - \varepsilon_2)^{\frac{1}{2}} - \varepsilon_2(\varepsilon_3 - \varepsilon_1)^{\frac{1}{2}}}{\varepsilon_1(\varepsilon_3 - \varepsilon_2)^{\frac{1}{2}} + \varepsilon_2(\varepsilon_3 - \varepsilon_1)^{\frac{1}{2}}}\right) \tag{2.43}$$

which is valid when

$$\frac{|\varepsilon_2|}{\varepsilon_1}\left(\frac{\varepsilon_3 - \varepsilon_1}{\varepsilon_3 - \varepsilon_2}\right)^{\frac{1}{2}} < 1 \tag{2.44}$$

Symmetric modes of thin film tolerate only a small amount of structural asymmetry, especially, at longer wavelengths. For a surface plasmon waveguide with ε_3= 11 and a Drude metal with plasma frequency of $\omega_p = 1.36 \times 10^{16} rad/s$, Fig. 2.9 shows the cutoff film thickness as a function of ε_1. Curves 1, 2 and 3 are corresponding to wavelengths 1 µm, 1.3 µm and 1.55µm, respectively.

2.4 Metal-Insulator-Metal (MIM) Surface Plasmon Waveguide

The planer MIM structure similar to the IMI structure does not support TE mode. However, it supports two TM SP modes; one symmetric and one asymmetric. Moreover, there are ordinary TE/TM modes of the conventional type considered in the introductory waveguide theory (where the structure is usually called the parallel plates waveguide). Unlike surface modes, the ordinary modes do not decay away from metal interfaces into the dielectric region and metal claddings act merely as reflectors. The energy carried by them is concentrated in the dielectric region rather than metal surfaces and as a result the dielectric layer should be reasonably thick, these type of modes depend on the geometry of the structure for metal grooves. These are called channel plasmon polariton modes CPPs. Now consider surface modes, for a symmetric structure with $\varepsilon_1 = \varepsilon_3 = -116.37 - j11.12$ and $\varepsilon_2 = 11.3$ at λ=1.55 μm, Fig. 2.10 shows the variation of propagation constant with dielectric film thickness. It is clear that from Figs. (2.10) and (2.5), there are a number of differences between MIM and IMI surface plasmon waveguides. A lower cutoff thickness for the asymmetric mode of MIM structure exists even for a symmetric structure. Second, the symmetric mode loss is huge and increases as the dielectric layer thickness decreases. This makes the structure impractical for many applications. For a very thick dielectric layer the propagation constants and losses of the two modes reach their corresponding values of a single interface structure. Therefore, the propagation losses of both modes are always larger than the loss of a single-interface surface waveguide. Since the electromagnetic field decays much faster in metal than it does in dielectric, the spatial extent of the surface plasmon modes in the MIM configuration can be dramatically less compared to mode sizes in the IMI counterpart. This makes the MIM structure attractive for subwavelength and nanophotonic applications. But as a waveguide, its use is restricted to very short distances.

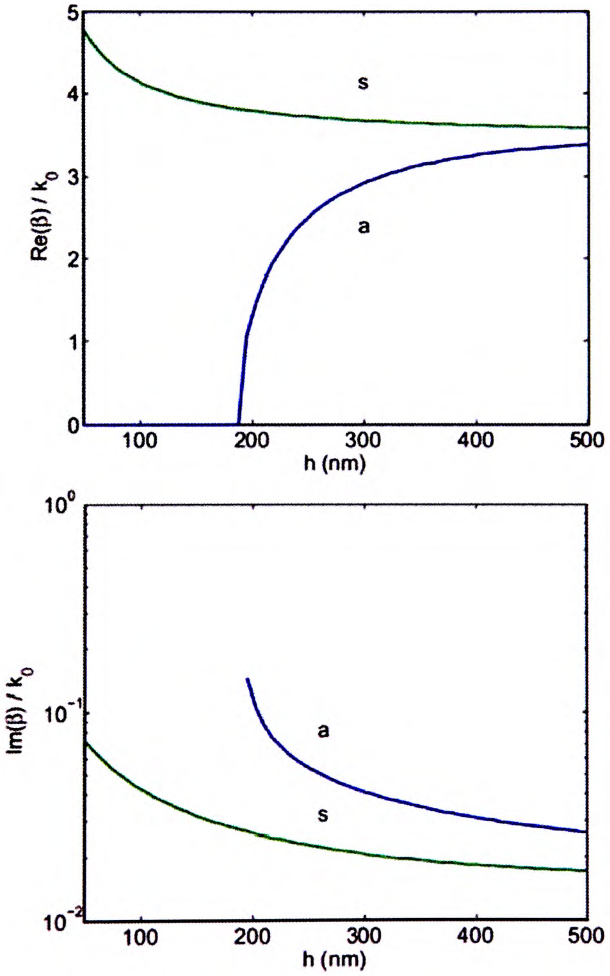

Figure 2.10 Shows the variations of real and imaginary parts of propagation constant of MIM structure modes with dielectric thickness h.

2.5 Other Types of Surface Plasmon Waveguide

Other than the three simple geometries considered in the previous sections numerous types of surface plasmon waveguides with more complex geometries have been proposed, characterised and measured. Fig. 2.11 shows various kinds of surface plasmon waveguides. The main purpose of these structures is to achieve one with low loss and well confined long range surface plasmon modes. Such structures are the backbone to implementation of a high density optical and optoelectronic integrated systems. Ease of in- and out- coupling of SPP modes to free space, optical fibres or other waveguides is another important design consideration.

From Fig. 2.11 the first three surface plasmon waveguides are called nanowires. The cylindrical shell nanowire (b) compared to the solid cylinder in (a) has the advantage of low loss when the radius is large [25, 26]. The waveguide has one LRSP mode and when the radius is large it becomes similar to the LRSP mode of an IMI structure. The square cross section SPWG in (c) not only supports low loss LRSP modes, but also couples favourably to fibre and the planar feature makes the fabrication easier compared to (a) and (b). This waveguide is a limiting case of (g) with the metal width and thickness being equal. Therefore, the modes of (c) are the evolved versions of those of (g). Because of its symmetry the square cross section waveguide has two degenerate TE and TM modes polarised perpendicularly. Modal power loss as low as 0.14 dB/mm with a coupling loss of 3 dB to single mode fibre is expected computationally [27]. Waveguides in (d)-(f) are 1D geometries, all shown to support

LRSP modes [28-34]. (d) and (f) contain high index dielectric slabs close to the metal slab. Individually, these dielectric slabs have their well-known conventional modes and therefore, when they get closer to the metal slab their conventional modes couple to SPP modes of metal slab to form hybrid modes. Since part of the field is guided outside the metal slab, their LRSP modal loss is lower than the loss of metal slab LRSP mode provided the structural parameters are selected properly.

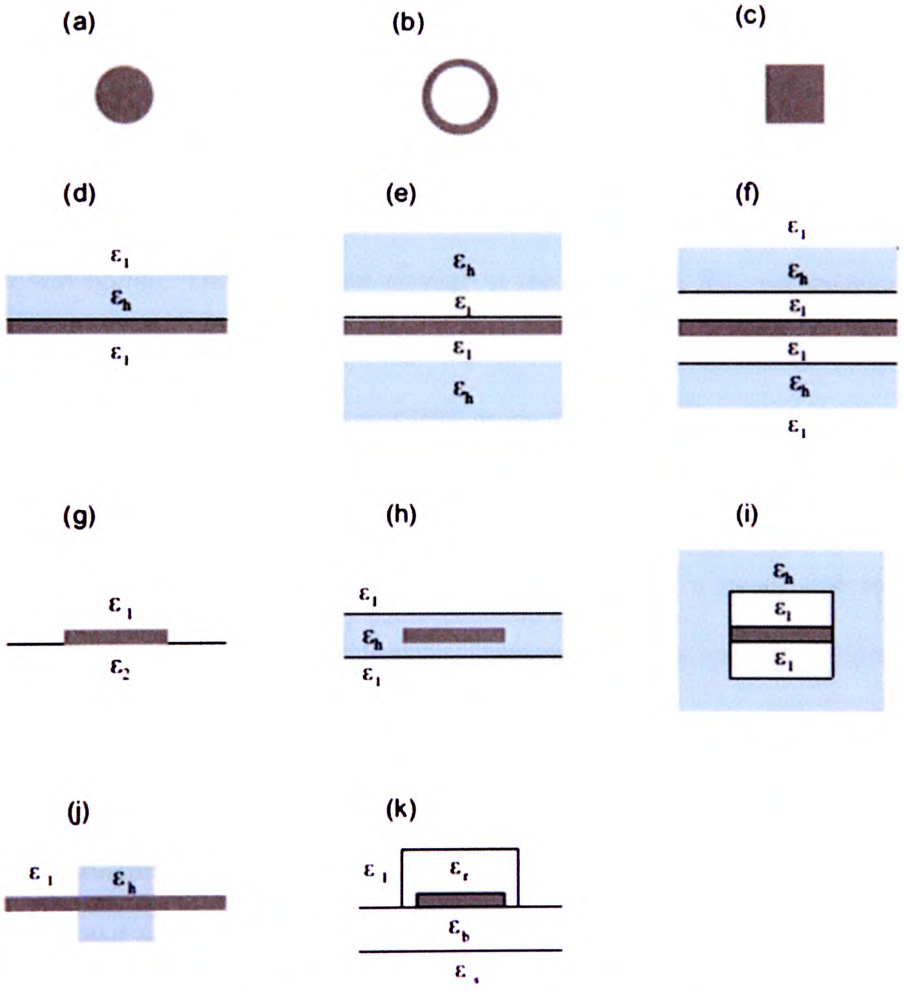

Figure 2.11 Various types of surface plasmon waveguides.

The low index gaps adjacent to the metal slab in (e) and (f) push the LRSP of those structures toward cutoff. Near cutoff, the loss decreases dramatically. The structural parameters, therefore, should be selected in the way that the waveguide is operating near cutoff. The problem, however, is the sensitivity to layer thicknesses as a slight offset leaves the LRSP mode in cutoff. In (e), when the low index slabs are filled with a high index material and the high index claddings are replaced with a low index material, loss increases compared to the IMI system, but modal confinement improves, again indicating the loss-confinement tradeoff.

For confinement in both transverse directions structures (g)-(k) have been introduced. SPWG in (j) comprises a metal slab passing through a buried rectangular dielectric waveguide. The modes are similar to the modes of IMI waveguide, except they are laterally confined due to the higher index of the buried channel. If the slab is thin enough the waveguide supports an LRSP mode [35].

The thin metal stripe SPWG in Fig. 2.11(g) is the most extensively studied one among the two dimensional SPWGs. Reducing the width of a metal slab to a finite value makes the modal loss smaller, but also changes the mode spectrum, dramatically. Unlike its metal slab counterpart, the propagation characteristics of metal stripe SPWG cannot be calculated analytically and the computational effort involved is considerably greater. The structure supports four fundamental bounded modes [36, 37] as opposed to only two bounded modes of the IMI structure. There can also exist higher order modes depending on the structural parameters. One of the fundamental modes referred to as ss_b^0 acquires a large propagation length provided the structure is symmetric ($\varepsilon_1 = \varepsilon_2$) and the film thickness is reasonably small. The mode is, accordingly, named LRSP mode. Similar to the metal slab structure there is a loss-confinement tradeoff as the film thickness varies. However, the loss in the finite width stripe can be orders of magnitude lower than the loss of metal slab waveguide. Another advantage is that its LRSP mode can be excited efficiently using end-recoupling to dielectric waveguides including the optical fibre [38, 39]. Reference [40] demonstrated propagation of the LRSP in an SPWG comprising an 8 μm wide, 20 nm thick gold stripe embedded in SiO2 at the communications wavelength of 1550 nm with a modal loss of 0.9 dB/mm. Modal losses of smaller than 0.1 dB/mm at the same wavelength have been predicted theoretically.

The structure of Fig. 2.11(h) is obtained by embedding a metal stripe in a dielectric slab waveguide. The modes are hybrid SPP-dielectric modes. The structure is shown to alleviate the attenuation-confinement trade-off compared to Fig. 2.11(g) [41]. The propagation length of a 6 μm wide and 10 nm thick gold stripe in BCB material was measured to be several millimetres at the 1550 nm wavelength [44].

The waveguide of Fig. 2.11(i) can be seen as the 2D generalisation of waveguide (e) and is meant to add the lateral confinement to the benefits of the former [42, 43]. Reference [42] reports the simulation results of a structure with a gold stripe of 1 μm×20 nm cross section, $\varepsilon_l = (1.45)^2$, $\varepsilon_h = (1.6)^2$ operating at $\lambda_0 = 850$ nm. Without the low index nanolayers the LRSP mode size was 1.76 μm and the 1/e propagation length was 935 μm. With 25 nm thick nanolayers the mode swelled to a size of 7.18 μm while the propagation range reached 2.65 cm. Further increasing the nanolayers thickness pushes the mode toward cutoff. At a critical thickness the mode stops being bounded to the film and the mode size is infinitely large much the same way as the waveguide (e).

Finally, the asymmetric structure shown in (k) can be designed in such a way to support a tightly confined long range SPP mode. Reference [44] calculated and showed that at $\lambda_0 = 1.55$ µm a propagation length of over 3 mm with a mode size of 1.6 µm.

Most of structures shown in Fig. 2.11 are very complicated structures to get an accurate analytical solution for the mode guided through. Therefore, a numerical model for those structures is needed in order to investigate their characteristic.

2.6 Summary

In this chapter the definition of surface plasmons was presented. It is the interaction between surface electrons at metal/dielectric interface and the electromagnetic wave of light. Plasmonic waveguide can be considered as a metal-insulator-metal (MIM) or insulator-metal-insulator (IMI) waveguide. Plasmonic waveguides enable the propagation of light behind the diffraction limit. However, plasmonic waveguides suffer from metal damping losses. The traditional planer MIM and IMI waveguides have been studied. Both of them can support symmetric and asymmetric plasmonic modes. However, MIM waveguide has a high confinement; it has also a high metal damping losses compared to IMI waveguide. Also different geometries of plasmonic waveguides have been presented. Such waveguides are designed for different proposes depending on the application.

Chapter 3

Finite-Difference Frequency-Domain Technique for Plasmonic Waveguides

3.1 Introduction

During the last few years, various accurate modelling methods have been developed for modal analysis of optical waveguides. These methods included the finite difference method (FDM) [45], finite element method (FEM) [46] and multipole method [47]. However, the modal solution techniques based on the finite difference method are very popular due to their simple implementations. In this thesis, the full vectorial finite difference method (FVFDM) [45] is used for analysing the optical waveguides successfully. An overview of the modelling methods is presented thoroughly in this chapter. In addition, the formulation of the FVFDM [45] with perfect boundary conditions capabilities is explained in detail.

3.2 Overview of Modelling Methods

Numerical simulations play an important role for the design and modelling of optical waveguides. So far, various modelling methods in which not only a full-vector model but also an approximate scalar model is used have been developed. An approximate-scalar model [48] is a valuable tool for aiding fabrication efforts because it is easy to use and provides good qualitative information. However, in order to model optical waveguides accurately, it is crucial to use a full-vector model. In particular, a complete vector model is necessary for predicting sensitive quantities such as dispersion and birefringence. The FEM [46] can provide high accuracy by means of flexible triangular and curvilinear meshes to represent the waveguide cross section. However, this results in an algorithm that is complex to implement. Also, the finite element based imaginary distance beam propagation method (IDBPM) has been suggested as a "mode solver" for optical waveguides [49]. Although accurate and versatile, IDBPM may sometimes lack convergence if a suitable initial field distribution is not chosen. Moreover, if higher order modes are needed, successive running of the iterative IDBPM code is required, which is not computationally efficient. On the contrary, the mode solvers based on the FDM [45] and multipole method [46] are very attractive because of their simple implementations. The FDM is probably the most widely used technique for the numerical modelling of optical waveguides. The appropriate algorithms for a rough finite difference solution to a structure with a very general geometry can be programmed very quickly. At the same time, FDMs offer a degree of flexibility with non-uniform meshing and also are applicable to all of the common modelling problems, including modal and propagation analyses.

The FDM is a procedure for transforming a partial differential equation into a finite set of linear equations. To do this, a rectangular mesh composed of lines parallel to the coordinate axis is superimposed on the problem space. The mesh points lie at the intersection of the mesh lines and form the discrete set of points at which the function values are stored. A portion of a two-dimensional finite-difference mesh is shown in Fig.3.1. In the figure the mesh steps Δx, and Δy are the distances between any two adjacent mesh points, in x and y directions, respectively. For each mesh point i *and* j with corresponding coordinates x_i and y_j, an approximate expression (or difference equation) $\varphi_{i,j} = \varphi(x_i, y_j)$ for the partial differential equation is formed that involves the function value at i, j, and at some of the surrounding points. This is normally done by expanding the field at various neighbouring points as a Taylor series to produce expressions for the derivatives occurring in the partial differential equation at i *and* j. Once this process has been performed for each point in the problem space, the complete set of linear equations relating the function values at all points is solved to give an approximate solution to the partial differential equation.

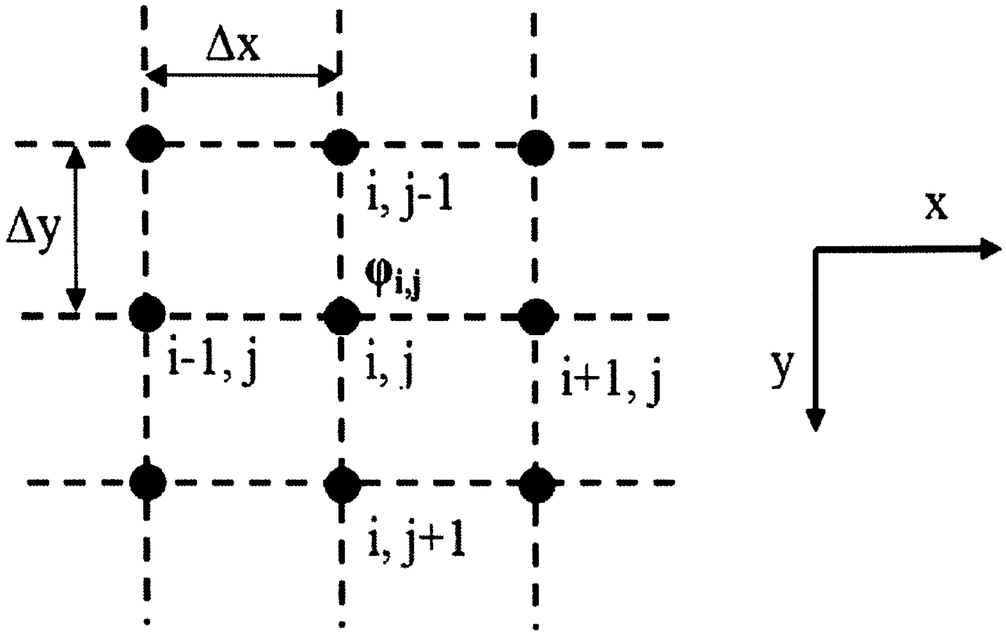

Figure 3.1 A part of typical uniform finite difference mesh

3.3 Introduction to the Simulation of Plasmonic Devices

The Finite-Difference Frequency-Domain (FDFD) technique is a general-purpose numerical technique for the solution of Maxwell's equations of electromagnetism in the frequency domain. It can be applied to structures of any length scale and for sources of electromagnetic radiation of any frequency. Here, however, the focus is on the use of this technique in nanooptics, and in particular plasmonics. Plasmonic is a rapidly evolving field of science and technology based on surface plasmons. Surface plasmons are electromagnetic waves that propagate along the interface of a metal and a dielectric. In surface plasmons, light interacts with the free electrons of the metal, which oscillate collectively in response to the applied field. Recently, nanometre scale metallic devices have shown the potential to manipulate light at the subwavelength scale using surface plasmons [50]. This could lead to photonic circuits of nanoscale dimensions.

Surface plasmons can be described by macroscopic electromagnetic theory, i.e., Maxwell's equations, if the electron mean free path in the metal is much shorter than the plasmon wavelength [51]. This condition is usually fulfilled at optical frequencies [51]. In macroscopic electromagnetic theory, bulk material properties, such as dielectric constant, are used to describe objects irrespective of their size. Here, all materials are assumed to be nonmagnetic ($\mu = \mu_0$) and are characterised by their bulk dielectric constant $\epsilon(r, \omega)$, where $r = (x, y, z) = x\hat{x} + y\hat{y} + z\hat{z}$, and ω is the angular frequency. However, for particles of nanometre dimensions a more fundamental description of their optical and electronic properties may be required [52].

Analytical methods, such as Mie theory [53], can only be applied to planar geometries or to objects of specific shapes (spheres, cylinders) and have therefore, limited importance in the analysis of plasmonic devices and structures. Numerical simulation techniques are therefore, very important for the analysis and design of plasmonic devices. Numerical modelling of plasmonic devices involves several challenges which need to be addressed. First, as mentioned above, plasmonic devices can have arbitrary geometries. Several techniques are specific for one type of geometrical configuration and are therefore not appropriate for modelling arbitrary plasmonic devices.

Second, the dielectric constant of metals at optical wavelengths is complex, i.e., $\epsilon_r(\omega) = Re\{\epsilon_r(\omega)\} + jIm\{\epsilon_r(\omega)\}$ and is a complicated function of frequency [54]. Thus, several simulation techniques that are limited to lossless, nondispersive materials are not applicable to plasmonic devices. In addition, in time-domain methods the dispersion properties of metals have to be approximated by suitable analytical expressions [55]. In most cases, the Drude model is invoked to characterise the frequency dependence of the metallic dielectric function [56]

$$\epsilon_{r,Drude}(\omega) = 1 - \frac{\omega_p^2}{\omega(\omega + i\gamma)} \tag{3.1}$$

where ω_p and γ are frequency-independent parameters. However, the Drude model approximation is valid over a limited wavelength range [56]. The range of validity of the Drude model can be extended by adding Lorentzian terms to Eq. (3.1) to obtain the Lorentz-Drude model [56]

$$\epsilon_{r,LD}(\omega) = \epsilon_{r,Drude}(\omega) + \sum_{j=1}^{k} \frac{f_j \omega_j^2}{\left(\omega_j^2 - \omega^2\right) - i\omega\gamma_j} \tag{3.2}$$

where ω_j and γ_j stand for the oscillator resonant frequencies and bandwidths, respectively, and f_j are weighting factors. Physically, the Drude and Lorentzian terms are related to intraband (free-electron) and interband (bound-electron) transitions, respectively [56]. Even though the Lorentz-Drude model extends the range of validity of analytical approximations to metallic dielectric constants, it is not suitable for description of sharp absorption edges observed in some metals, unless a very large number of terms are used [56]. In particular, the Lorentz-Drude model cannot approximate well the onset of interband absorption in noble metals (Ag, Au, and Cu), even if five Lorentzian terms are used [56]. In Fig. 3.2, the Drude and Lorentz- Drude models are compared with experimental data for silver. It is observed that even a five-term Lorentz-Drude model with optimal parameters results in a factor of two error at certain frequencies.

In surface plasmons propagating along the interface of a metal and a dielectric, the field is concentrated at the interface, and decays exponentially away from the interface in both the metal and dielectric regions [12]. Thus, for numerical methods based on discretisation of the fields on a numerical grid, a very fine grid resolution is required at the metal-dielectric interface to adequately resolve the local fields. In addition, several plasmonic devices are based on components of subwavelength dimensions [12]. In fact, most of the potential applications of surface plasmons are related to subwavelength optics. The nanoscale feature sizes of plasmonic devices pose an extra challenge to numerical simulation techniques.

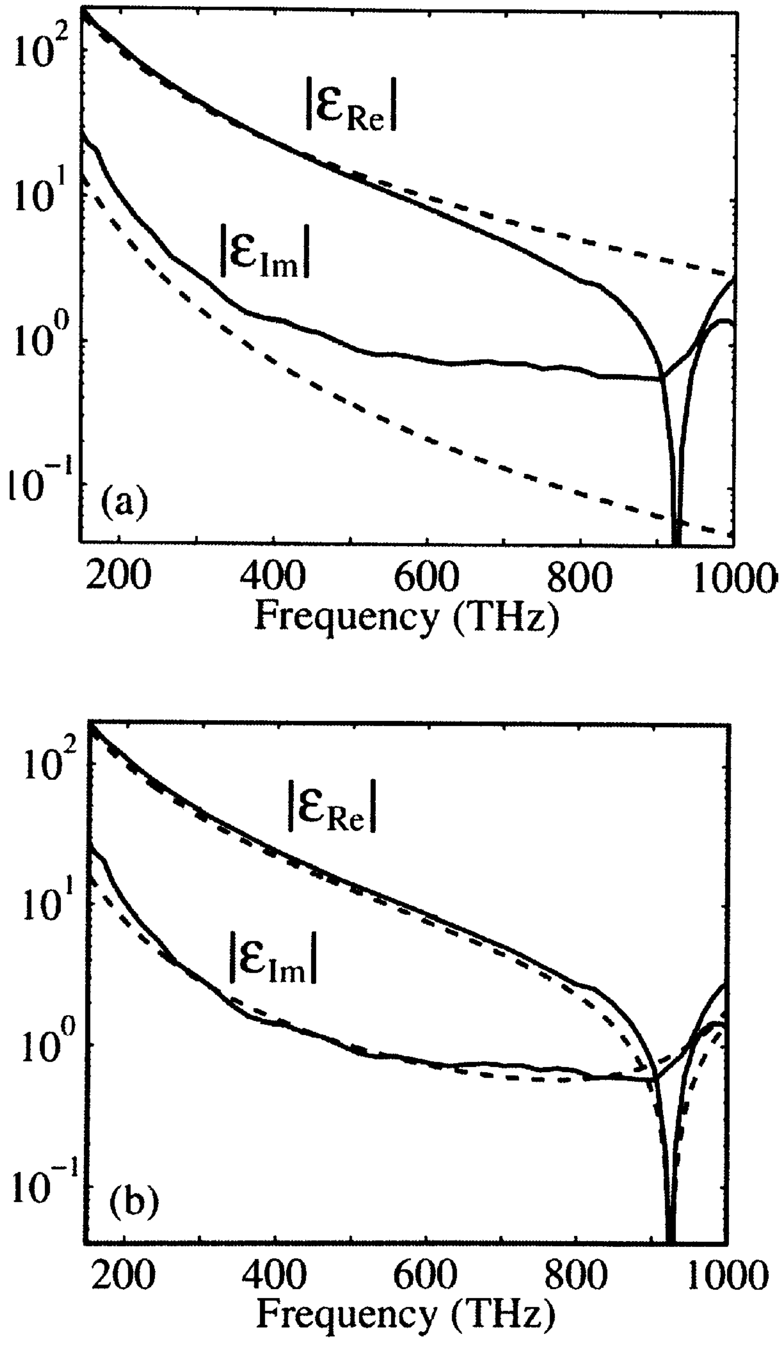

Figure 3.2 Real and imaginary part of the dielectric constant of silver at optical frequencies. The solid lines show experimental data [54]. The dashed lines show values calculated using (a) the Drude model and (b) the Lorentz-Drude model with five Lorentzian terms. The parameters of the models are optimal and obtained through an optimization procedure [56].

The challenges involved in modelling plasmonic devices will be illustrated here using a simple example: an infinite periodic array of silver cylinders illuminated by a plane wave at normal incidence (inset of Fig. 3.3(a)). The FDFD method, which is described in detail below, is used to calculate the transmission of the periodic array. This method allows one to directly use experimental data for the frequency-dependent dielectric constant of metals, including both the real and imaginary parts, with no approximation. The fields are discretised on a uniform two-dimensional (2-D) grid with grid size $\Delta x = \Delta y = \Delta l$. The calculated transmission as a function of frequency is shown in Fig. 3.3(a). Also shown is the transmission of the structure calculated with the Drude model of equation (3.1). It is observed that the use of the Drude model results in substantial error. In general, the Drude model parameters are chosen to minimise the error in the dielectric function in a given frequency range [57]. However, this approach gives accurate results in a limited wavelength range, as illustrated in this example. In general, the complicated dispersion properties of metals at optical frequencies pose a challenge in modelling of plasmonic devices not encountered in modelling of low- or high-index contrast dielectric devices.

The calculated transmission at a specific wavelength as a function of the spatial grid size Δl is shown in Fig. 3.3(b). It is observed that a grid size of $\Delta l \approx 1nm$ is required in this case to yield reasonably accurate results. The required grid resolution is directly related to the decay length of the fields at the metal-dielectric interface. In general, modelling of plasmonic devices requires much finer gird resolution than modelling of low- or high-index-contrast dielectric devices, due to the high localisation of the field at metal-dielectric interfaces of plasmonic devices. The required grid size depends on the shape and feature size of the modelled plasmonic device, the metallic material used, and the operating frequency.

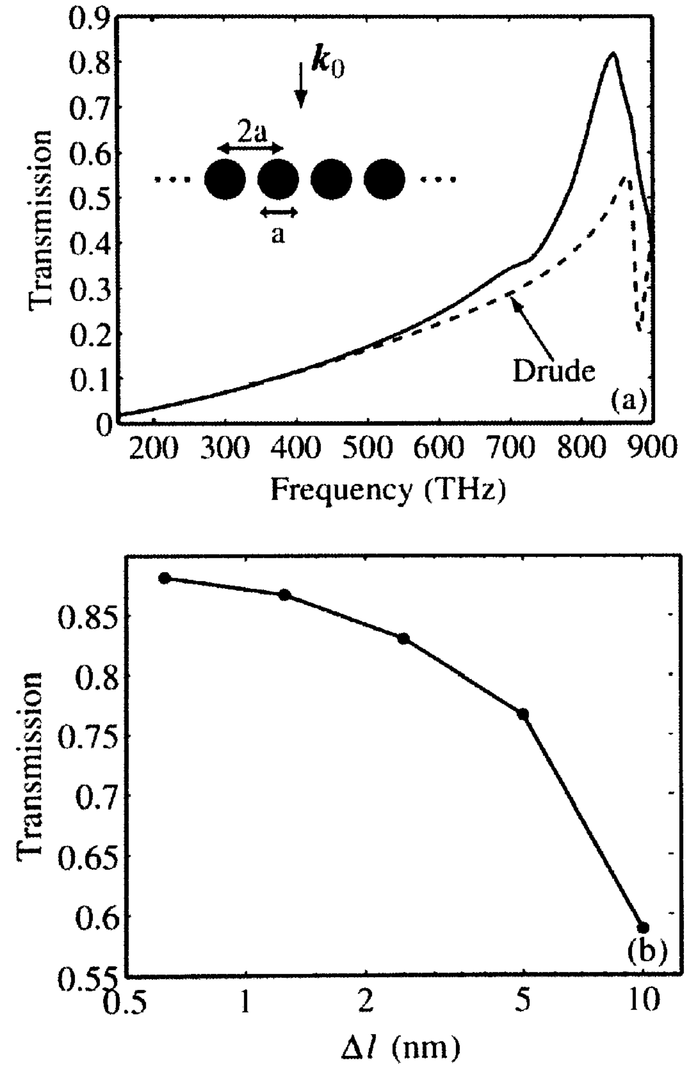

Figure 3.3 (a) transmission spectrum of an infinite array of silver cylinders (shown in the inset) for normal incidence and transverse magnetic (TM) polarization (involving only the E_x, E_y *and* H_z vector field components). Results are shown for a diameter $a = 100\,nm$. The dashed line shows the transmission spectrum calculated using the Drude model equation (3.1) with parameters $\omega_p = 1.36 \times 10^{16} s^{-1}$ and $\gamma = 7.28 \times 10^{13} s^{-1}$. (b) Calculated transmission at 855 THz as a function of the spatial grid size Δl.

3.4 Introduction to Finite-Difference Methods

FDFD is based on approximating the derivatives in Maxwell's equations by finite differences. A brief overview of the main features of finite-difference methods is therefore first provided here. In finite-difference methods, derivatives in differential equations are approximated by finite differences. To approximate the derivative $df/dx|_{x_0}$ Taylor series expansions of $f(x)$ about the point x_0 at the points $x_0 + \Delta x$ and $x_0 - \Delta x$ are used to obtain [55]

$$\left.\frac{df}{dx}\right|_{x_0} = \frac{f(x_0 + \Delta x) - f(x_0 - \Delta x)}{2\Delta x} + O[(\Delta x)^2] \tag{3.3}$$

Here, the notation $O[(\Delta x)^2]$ (to be read as "order $(\Delta x)^2$") denotes the remainder term and indicates its dependence on Δx, i.e., that it approaches zero as the second power of Δx. Thus, Eq. (3.3) shows that a central-difference approximation of the first derivative is second-order accurate, meaning that the remainder term in Eq. (3.3) approaches zero as the square of Δx.

In finite-difference methods a continuous problem is approximated by a discrete one. Field quantities are defined on a discrete grid of nodes. The rectangular grid with node coordinates $r_{ijk} = (x_i, y_j, z_k)$ is the simplest and most commonly-used. A field quantity at nodal location r_{ijk} is denoted for convenience as $f_{ijk} = f(r_{ijk})$. Based on Eq. (3.3), the first derivative can be approximated by the following central-difference formula

$$\left.\frac{df}{dx}\right|_i \cong \frac{f_{i+1} - f_{i-1}}{2\Delta x} \tag{3.4}$$

which is second-order accurate, based on the discussion above, if the rectangular grid is uniform, i.e. $x_i = i\Delta x$. For example, if the numerical resolution in the x direction is increased by a factor of 10 ($\Delta x' = \Delta x/10$), then the error introduced by the finite-difference formula in Eq. (3.4) reduces roughly by a factor of $10^2 = 100$.

Similarly, the second derivative can be approximated by the formula

$$\left.\frac{d^2 f}{dx^2}\right|_i \cong \frac{f_{i+1} - 2f_i + f_{i-1}}{(\Delta x)^2} \tag{3.5}$$

which is also second-order accurate on a uniform grid [55].

By replacing derivatives in differential equations with their finite-difference approximations, we obtain algebraic equations which relate the value of the field at a specific node to the values at neighboring nodes. By applying the finite-difference approximation to all nodes of the grid, a system of linear equations of the form $Ax = b$ is obtained. Since the equation for the field at each point involves only the fields at the four (six in three dimensions, two in one dimension) adjacent points, the resulting system matrix is extremely sparse. Such problems can be solved efficiently if direct or iterative sparse matrix techniques are used.

3.5 Maxwell's Equations

Maxwell's equations are a set of four partial differential equations (see appendix A) that describe the properties of the electric and magnetic fields through the medium. In the frequency domain, the propagation of electromagnetic waves through the waveguide is governed by Maxwell's equations which can be written as follows (assuming sinusoidal plane-wave ($\partial/\partial t = j\omega$) with no charge ($\rho = 0$) and no current ($J = 0$))

$$\nabla \times E = -j\omega\mu H \tag{3.6}$$

$$\nabla \times H = j\omega\varepsilon E \tag{3.7}$$

$$\nabla.(\varepsilon E) = 0 \tag{3.8}$$

$$\nabla.(\mu H) = 0 \tag{3.9}$$

where the vector quantities E and H are electric and magnetic field vectors, respectively, $\varepsilon = \varepsilon_0\varepsilon_r$ and $\mu = \mu_0\mu_r$. The quantities ε and μ define the electromagnetic properties of the medium and are the permittivity tensor and the permeability of the waveguide material, respectively. $\varepsilon_0=8.854\times10^{-12}$ F/m is the permittivity of free space, and $\mu_0 = 4\pi\times10^{-7}$H/m is the permeability of free space. ε_r and μ_r are the relative permittivity and permeability of the waveguide material. In this study for nonmagnetic waveguides, μ_r is taken as unity.

3.6 Wave Equation

The total electromagnetic field that is supported by a waveguide can be expressed in terms of only the electric or magnetic field components to produce wave equations. In this section the derivation that models the magnetic field is considered. In this case, the electric field is removed from the derivation by taking the curl of equation (3.7) and substituting using (3.6). The vector wave equation for the magnetic field vector, H, can be written as

$$\nabla \times (\varepsilon_r^{-1} \nabla \times H) - k_0^2 H = 0 \tag{3.10}$$

where k_0 is the free space wave number $k_0^2 = \omega^2 \mu_0 \varepsilon_0$. The anisotropic material is assumed to have one of its principal axes points in the direction of the waveguide. Under this assumption, the permittivity tensor takes the form

$$\varepsilon = \varepsilon_0 \varepsilon_r = \varepsilon_0 \begin{bmatrix} \varepsilon_{xx} & \varepsilon_{xy} & 0 \\ \varepsilon_{yx} & \varepsilon_{yy} & 0 \\ 0 & 0 & \varepsilon_{zz} \end{bmatrix} \tag{3.11}$$

For isotropic waveguides, $\varepsilon_{xx}=\varepsilon_{yy}=\varepsilon_{zz}$ and $\varepsilon_{xy}=\varepsilon_{yx}=0$, in this work all materials will be considered isotopic materials. Using the vector identity $\nabla \times (AB) = \nabla A \times B + A\nabla \times B$, the vector wave equation (3.10) can be rewritten as follows

$$\nabla^2 H + k_0^2 \varepsilon_r H = -\varepsilon_r^{-1} \nabla \varepsilon_r \times (\nabla \times H) \tag{3.12}$$

The transverse component of the vector wave equation (3.12) can be expressed as

$$\nabla^2 H_t + k_0^2 \varepsilon_{rt} H_t = -\varepsilon_{rt}^{-1} \nabla_t \varepsilon_{rt} \times (\nabla_t \times H_t) \tag{3.13}$$

where the subscript "t" stands for the transverse components and ε_{rt} is the transverse components of the relative dielectric tensor and can be defined such that

$$\varepsilon_{rt} = \begin{bmatrix} \varepsilon_{xx} & \varepsilon_{xy} \\ \varepsilon_{yx} & \varepsilon_{yy} \end{bmatrix} \tag{3.14}$$

Assuming a z dependence of $e^{-j\beta z}$ for all fields, the longitudinal component H_z can be computed from the transverse component H_x and H_y by applying the divergence relation $\nabla . H = 0$.

$$H_z = \frac{1}{j\beta}\left(\frac{\partial H_x}{\partial x} + \frac{\partial H_y}{\partial y}\right) \tag{3.15}$$

where β is the propagation constant of the propagated mode. Using the vector wave equation (3.13), (3.15) and the divergence relation $\nabla . H = 0$, one can obtain, after some algebraic treatment, the following full vector eigenvalue equation

$$\begin{bmatrix} A_{xx} & A_{xy} \\ A_{yx} & A_{yy} \end{bmatrix} \begin{bmatrix} H_x \\ H_y \end{bmatrix} = \beta^2 \begin{bmatrix} H_x \\ H_y \end{bmatrix} \tag{3.16}$$

where A_{xx}, A_{xy}, A_{yx} and A_{yy} are the differential operators which can be defined such that [45]

$$A_{xx}H_x = \frac{\partial^2 H_x}{\partial x^2} + \frac{\varepsilon_{yy}}{\varepsilon_{zz}}\frac{\partial^2 H_x}{\partial y^2} + \frac{\varepsilon_{yx}}{\varepsilon_{zz}}\frac{\partial^2 H_x}{\partial y \partial x} + k^2 \varepsilon_{yy} H_x \tag{3.17}$$

$$A_{xy}H_y = \left(1 - \frac{\varepsilon_{yy}}{\varepsilon_{zz}}\right)\frac{\partial^2 H_y}{\partial x \partial y} - \frac{\varepsilon_{yx}}{\varepsilon_{zz}}\frac{\partial^2 H_y}{\partial x^2} - k^2 \varepsilon_{yx} H_y \tag{3.18}$$

$$A_{yx}H_x = \left(1 - \frac{\varepsilon_{xx}}{\varepsilon_{zz}}\right)\frac{\partial^2 H_x}{\partial x \partial y} - \frac{\varepsilon_{xy}}{\varepsilon_{zz}}\frac{\partial^2 H_x}{\partial y^2} - k^2 \varepsilon_{xy} H_x \tag{3.19}$$

$$A_{yy}H_y = \frac{\partial^2 H_y}{\partial y^2} + \frac{\varepsilon_{xx}}{\varepsilon_{zz}}\frac{\partial^2 H_y}{\partial x^2} + \frac{\varepsilon_{xy}}{\varepsilon_{zz}}\frac{\partial^2 H_y}{\partial x \partial y} + k^2 \varepsilon_{xx} H_y \tag{3.20}$$

The differential operators can be approximated by using the finite difference methods [45] as illustrated in Appendix A. Equation (3.16) is a full-vector eigenvalue equation, which describes the modes of propagation for anisotropic optical waveguides. The two transverse field components H_x and H_y are the eigenvectors, and the corresponding eigenvalue is β^2.

Once all three components of the magnetic field H are known, the electric flux density D can be found by applying $\nabla \times H = j\omega D$, which gives

$$D_x = \frac{-1}{\omega\beta}\left(\frac{\partial^2 H_x}{\partial y \partial x} + \frac{\partial^2 H_y}{\partial y^2}\right) + \frac{\beta}{\omega} H_y \tag{3.21}$$

$$D_y = \frac{1}{\omega\beta}\left(\frac{\partial^2 H_y}{\partial x \partial y} + \frac{\partial^2 H_x}{\partial x^2}\right) - \frac{\beta}{\omega} H_x \tag{3.22}$$

$$D_z = \frac{j}{\omega}\left(\frac{\partial H_x}{\partial y} - \frac{\partial H_y}{\partial x}\right) \tag{3.23}$$

And the electric field can be computed from D by using $\mathrm{E} = \varepsilon^{-1}\mathrm{D}$ as follows

$$\begin{bmatrix} E_x \\ E_y \end{bmatrix} = \frac{1}{\varepsilon_0\left(\varepsilon_{xx}\varepsilon_{yy} - \varepsilon_{xy}\varepsilon_{yx}\right)} \begin{bmatrix} \varepsilon_{yy} & -\varepsilon_{xy} \\ -\varepsilon_{yx} & \varepsilon_{xx} \end{bmatrix} \begin{bmatrix} D_x \\ D_y \end{bmatrix} \tag{3.24}$$

$$E_z = \frac{1}{\varepsilon_0 \varepsilon_{zz}} D_z = \frac{j}{\omega \varepsilon_0 \varepsilon_{zz}}\left(\frac{\partial H_x}{\partial y} - \frac{\partial H_y}{\partial x}\right) \tag{3.25}$$

3.7 The FDFD Method in One Dimension

The FDFD equations will now be derived by approximating the spatial derivatives in Maxwell's equations with finite differences. Assuming an $exp(i\omega t)$ harmonic time dependence for all field quantities, Maxwell's curl equations, shown in Appendix A, in the frequency domain take the form (assume no charge ($\rho = 0$) and current source is polarized in z direction ($J = J_z$))

$$\nabla \times E(r) = -i\omega\mu_0 H(r) \tag{3.26}$$

$$\nabla \times H(r) = J(r) + i\omega\epsilon E(r) \tag{3.27}$$

It should be noted that the field vectors $E(r,t), H(r,t)$ are real (measurable) quantities that can vary with time, whereas the vectors $E(r,\omega), H(r,\omega)$ are complex phasors that do not vary with time. The former can be obtained from the latter by multiplying by $exp(i\omega t)$ and taking the real part. For example,

$$E(r,t) = Re\{E(r)e^{i\omega t}\} \tag{3.28}$$

It should also be noted that in most cases, for simplicity, the frequency dependence of the complex phasor is not explicitly shown, e.g., $E(r)$ is used instead of $E(r,\omega)$. Maxwell's equations can be simplified by considering electromagnetic fields and systems with no variations in two dimensions, namely, both y and z. By dropping all the y and z derivatives in Eqs. (3.26) and (3.27), and assuming a current source polarised in the z direction ($J = J_z\hat{z}$), Maxwell's equations simplify to

$$\frac{\partial E_z}{\partial x} = i\omega\mu_0 H_y \tag{3.29}$$

$$\frac{\partial H_y}{\partial x} = J_z + i\omega\epsilon E_z \tag{3.30}$$

In the Finite-Difference Time-Domain (FDTD) technique a staggered spatial grid, known as the Yee grid [55], is used for interleaved placement of the electric and magnetic fields. The Yee grid enables the approximation of the continuous derivatives in space by second-order-accurate two-point centered finite differences. Since the spatial derivatives involved in Maxwell's equations in the frequency domain are exactly the same as those in the time domain, the Yee grid can also be used in FDFD. The placement of the electric and magnetic fields on a one-dimensional (1-D) Yee grid for FDFD is identical to the one for FDTD, and is shown in Fig. 3.4.

$$\frac{E_z|_{i+1} - E_z|_i}{\Delta x} = i\omega\mu_0 H_y\big|_{i+1/2} \tag{3.31}$$

$$\frac{H_y\big|_{i+1/2} - H_y\big|_{i-1/2}}{\Delta x} = J_z|_i + i\omega\epsilon|_i E_z|_i \tag{3.32}$$

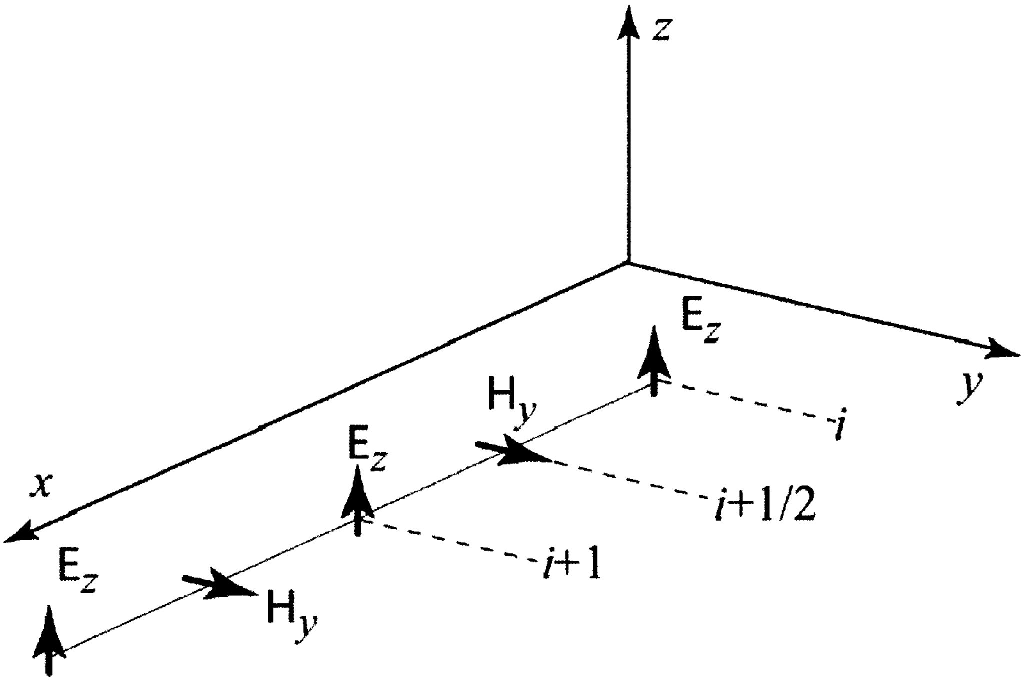

Figure 3.4 The placement of electric and magnetic field vectors in FDFD for Maxwell's equations in one dimension.

As mentioned above, by applying Eqs. (3.31) and (3.32) at all points in the Yee grid, a system of linear equations is obtained, which can be solved to find the electromagnetic fields. If the system obtained from Eqs. (3.31) and (3.32) was directly solved, all electric fields $\left(E_z|_1, E_z|_2, \ldots, E_z|_{N_x+1}\right)$, and all magnetic fields $\left(H_y\big|_{1+1/2}, H_y\big|_{2+1/2}, \ldots, H_y\big|_{N_x+1/2}\right)$ would have to be included in the vector of unknown fields. (A 1-D Yee grid terminated at electric field positions was assumed here). Thus, the system of linear equations would have a total of $2N_x + 1$ unknowns. However, in the system of equations obtained from the FDFD algorithm, it is straightforward to eliminate either all the electric or all the magnetic fields. To see this, Eq. (3.31) is applied at two adjacent grid points:

$$\frac{1}{i\omega\mu_0}\frac{E_z|_i - E_z|_{i-1}}{\Delta x} = H_y\Big|_{i-1/2} \tag{3.33}$$

$$\frac{1}{i\omega\mu_0}\frac{E_z|_{i+1} - E_z|_i}{\Delta x} = H_y\Big|_{i+1/2} \tag{3.34}$$

Equations (3.33) and (3.34) are now substituted into Eq. (3.32) to obtain

$$\frac{1}{\Delta x}\left[\frac{1}{i\omega\mu_0}\frac{E_z|_{i+1} - E_z|_i}{\Delta x} - \frac{1}{i\omega\mu_0}\frac{E_z|_i - E_z|_{i-1}}{\Delta x}\right] = J_z|_i + i\omega\epsilon|_i E_z|_i \tag{3.35}$$

which can also be written as

$$\frac{1}{\mu_0}\frac{E_z|_{i+1} - E_z|_i}{(\Delta x)^2} - \frac{1}{\mu_0}\frac{E_z|_i - E_z|_{i-1}}{(\Delta x)^2} + \omega^2\epsilon|_i E_z|_i = i\omega J_z|_i \tag{3.36}$$

Thus, application of finite-difference approximations at the node location x_i results in a linear algebraic equation which relates the field $E_z|_i$ to the fields at the two adjacent nodes $E_z|_{i-1}$ and $E_z|_{i+1}$. By applying the finite-difference approximation to all internal nodes of the grid, a system of linear equations of the form $Ax = b$ is obtained, where b is determined by the source current :

$$\begin{aligned} a_{ii-1} &= a_{ii-1} = \frac{1}{(\Delta x)^2} \\ a_{ii} &= \frac{-2}{(\Delta x)^2} + \omega^2\epsilon|_i\mu_0 \\ b_i &= i\omega\mu_0 J_z|_i \\ x_i &= E_z|_i \end{aligned} \tag{3.17}$$

The FDFD equations for the boundary nodes depend on the boundary conditions at the boundary of the simulation domain. Typically, they involve only the two outermost nodes, e.g., $a_{11}x_1 + a_{12}x_2 = 0$. Thus, in the 1-D case the linear system matrix A is tri-diagonal, and it is straightforward to eliminate the magnetic fields, and obtain a system of equations which only involves the electric fields $\left(E_z|_1, E_z|_2, \dots, E_z|_{N_x+1}\right)$ and has a total of $N_x + 1$ unknowns.

Finally, if Eqs. (3.29) and (3.30) are combined, the Helmholtz equation in 1-D is obtained:

$$\frac{\partial^2 E_z}{\partial x^2} + \omega^2 \epsilon \mu_0 E_z = i\omega\mu_0 J_z \qquad (3.38)$$

When the spatial derivatives in this equation are approximated by centered finite differences, Eq. (3.36) above is obtained. In other words, the FDFD equations can be directly obtained by discretising the Helmholtz equation for the electric field.

3.8 The FDFD Method in Two and Three Dimensions

For the 2-D case, it is assumed that there are no variations of either the fields or the excitation in one of the directions, say the z direction. Thus, all derivatives with respect to z drop out from the two curl equations (3.26) and (3.27). A current source polarised in the z direction ($J = J_z\hat{z}$) is also assumed, so that only the transverse electric (TE) polarisation (involving only the $H_x, H_y\ and\ E_z$ vector field components) is excited [55] and Maxwell's equations simplify to

$$\begin{aligned} \frac{\partial E_z}{\partial y} &= -i\omega\mu_0 H_x \\ \frac{\partial E_z}{\partial x} &= i\omega\mu_0 H_y \\ \frac{\partial H_y}{\partial x} - \frac{\partial H_x}{\partial y} &= J_z + i\omega\epsilon E_z \end{aligned} \tag{3.39}$$

If the above equations are combined, the 2-D Helmholtz equation is obtained

$$\frac{\partial^2 E_z}{\partial x^2} + \frac{\partial^2 E_z}{\partial y^2} + \omega^2 \epsilon\mu_0 E_z = i\omega\mu_0 J_z \tag{3.40}$$

As mentioned in the previous section, the exact same FDTD Yee grid can be used in FDFD. A portion of the Yee grid for the TE case is depicted in Fig. 3.5. The FDFD equations can be obtained by discretising Eq. (3.39). It is then straightforward to eliminate H_x and H_y to obtain the FDFD equations which only involve the E_z field. Here, however, the 2-D Helmholtz equation (3.40) is discretised to directly obtain the FDFD equations which only involve the E_z field. Once Ez is calculated by solving the FDFD equations, the H_x and H_y fields can be calculated by using the discretised versions of Eq. (3.39).

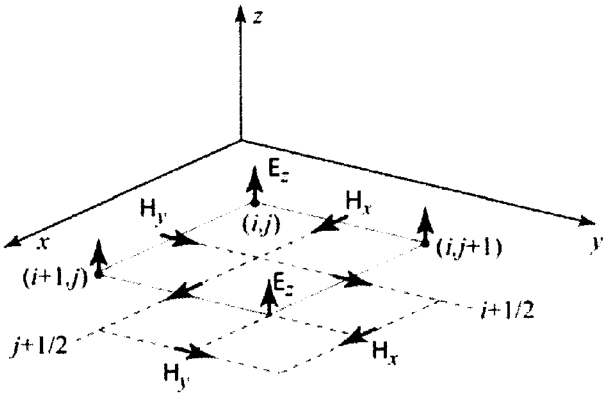

Figure 3.5 An FDFD unit cell for transverse electric (TE) waves. The small vectors with thick arrows are placed at the point in the grid at which they are defined. For example, Ez is defined at grid points (i,j), while Hy is defined at grid points $(i + 1/2,j)$.

For simplicity a uniform rectangular grid with $x_i = i\Delta x$ and $y_i = i\Delta y$ is considered, and the derivatives in Eq. (3.40) are replaced with their finite-difference approximations to obtain

$$\frac{E_z|_{i+1,j} - 2E_z|_{i,j} + E_z|_{i-1,j}}{(\Delta x)^2} + \frac{E_z|_{i,j+1} - 2E_z|_{i,j} - E_z|_{i,j-1}}{(\Delta y)^2} + \omega^2\epsilon|_{i,j}\mu_0 E_z|_{i,j} = i\omega\mu_0 J_z|_{i,j} \tag{3.41}$$

Thus, application of finite-difference approximations at the node location $r_{ij} = (x_i, y_j)$ results in a linear algebraic equation which relates the field $E_z|_{i,j}$ to the fields at the four adjacent nodes $E_z|_{i-1,j}$, $E_z|_{i+1,j}$, $E_z|_{i,j+1}$ and $E_z|_{i,j-1}$. In the end, the finite-difference approximation is applied to all nodes of the grid to obtain one FDFD equation at each grid point (i,j). These equations form a system of linear equations $Ax = b$ with $(N_x + 1) \times (N_y + 1)$ equations and unknowns. The vector of unknown fields x will include the electric fields at all mesh points (i,j), where $i = 1,2,\dots,N_x + 1$, and $j = 1,2,\dots,N_y + 1$. Note that x is a one-dimensional vector. We should therefore construct a one-to-one mapping between the two-dimensional electric field $E_z|_{i,j}$, $i = 1, 2, \dots, N_x + 1$, $j = 1, 2, \dots, N_y + 1$ and the one-dimensional vector of unknown fields $x_m, m = 1, 2, \dots, (N_x + 1) \times (N_y + 1)$. Choosing the right mapping is in general important and can affect the convergence of the system of linear equations. One simple mapping function in the two-dimensional case is:

$$m(i,j) = (i-1)(N_y+1) + j \tag{3.42}$$

Using this one-to-one mapping function, the following system of linear equations is obtained:

$$\begin{aligned}
a_{m(i,j)m(i-1,j)} &= a_{m(i,j)m(i+1,j)} = \frac{1}{(\Delta x)^2} \\
a_{m(i,j)m(i,j-1)} &= a_{m(i,j)m(i,j+1)} = \frac{1}{(\Delta y)^2} \\
a_{m(i,j)m(i,j)} &= \frac{-2}{(\Delta x)^2} - \frac{2}{(\Delta y)^2} + \omega^2 \epsilon|_{i,j} \mu_0 \\
b_{m(i,j)} &= i\omega\mu_0 J_z|_{i,j} \\
x_{m(i,j)} &= E_z|_{i,j}
\end{aligned} \tag{3.43}$$

The same approach can be applied to obtain the FDFD equations for the 2-D TM case as well as for the 3-D case.

3.9 Numerical Dispersion of the FDFD Algorithm

A single plane wave propagating in a uniform medium has a simple dispersion relation connecting the angular frequency ω and the wave number k : $\omega = ck$ [58], where c is the speed of light in the medium. Numerical techniques such as the FDFD technique introduce numerical dispersion. To derive the dispersion properties of the FDFD algorithm, a single wave or Fourier mode in space is considered. The dispersive properties of FDFD are assessed by obtaining the dispersion relation of the scheme, relating the frequency of a Fourier mode on the grid to a particular wavelength λ (or wave number k):

$$\omega = f_{FDFD}(k, \Delta x) \tag{3.44}$$

In the 1-D case, a plane wave propagating in a uniform medium is considered

$$E(x) = e^{jkx} \tag{3.45}$$

and its discretised version is

$$E|_i = e^{jki\Delta x} \tag{3.46}$$

In a uniform medium with no sources the FDFD equation (3.36) becomes

$$\frac{E_z|_{i+1} - 2E_z|_i + E_z|_{i-1}}{(\Delta x)^2} + \omega^2 \epsilon|_i \mu_0 E_z|_i = 0 \tag{3.47}$$

Equation (3.46) is substituted into Eq. (3.47) to find

$$\frac{e^{jki\Delta x}\left(e^{jk\Delta x} - 2 + e^{-jk\Delta x}\right)}{(\Delta x)^2} + \omega^2 \epsilon|_i \mu_0 e^{jki\Delta x} = 0 \tag{3.48}$$

from which one obtains

$$\omega = ck\left(\frac{sin\left(\frac{k\Delta x}{2}\right)}{\frac{k\Delta x}{2}}\right) \tag{3.49}$$

Eq. (3.49) is the dispersion relation of 1-D FDFD. It is observed that, in the limit $\Delta x \rightarrow 0$, Eq. (3.49) reduces to the exact dispersion relation $\omega = ck$. Using Eq. (3.49), the numerical phase velocity $\tilde{v}_p \equiv \frac{\omega}{k}$ and group velocity $\tilde{v}_g \equiv \frac{\partial\omega}{\partial k}$ of the FDFD scheme can be derived. The numerical phase velocity of 1-D FDFD as a function of the numerical resolution $\Delta x/\lambda$ is shown in Fig. 3.6. It is observed, for example, that for a spatial resolution of 20 grid points per wavelength ($\Delta x/\lambda = 0.05$) the numerical error in the phase velocity is less than 1%.

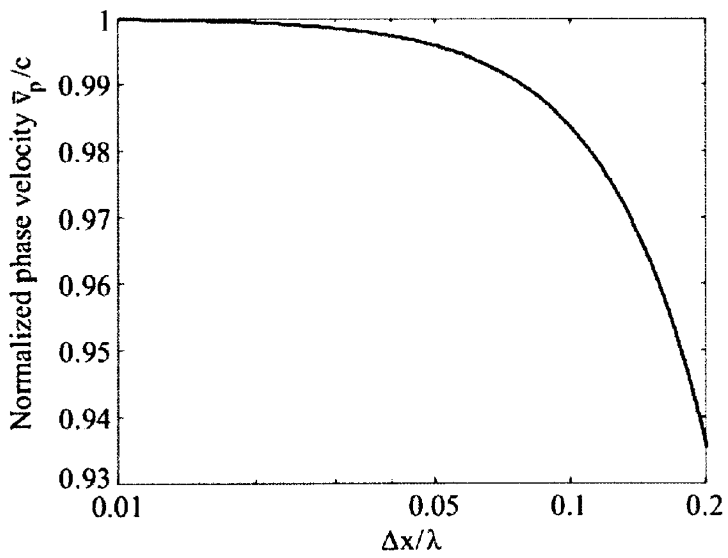

Figure 3.6 Dispersion of 1-D FDFD. Variation of numerical phase velocity with numerical resolution $\Delta x/\lambda$ in 1-D FDFD.

In the 2-D case, wave-like modes propagating in both x and y directions are considered

$$E(x, y) = e^{\sqrt{-1}(k_x x + k_y y)} \tag{3.50}$$

and their discretised version is

$$E|_{i,j} = e^{\sqrt{-1}(k_x i\Delta x + k_y j\Delta y)} \tag{3.51}$$

where k_x and k_y are the wave numbers in the x and y directions, respectively.

In a uniform medium with no sources, the 2-D FDFD equation (3.41) becomes

$$\frac{E_z|_{i+1,j} - 2E_z|_{i,j} + E_z|_{i-1,j}}{(\Delta x)^2} + \frac{E_z|_{i,j+1} - 2E_z|_{i,j} + E_z|_{i,j-1}}{(\Delta x)^2} + \omega^2 \epsilon|_{i,j}\mu_0 E_z|_{i,j} \\ = 0 \tag{3.52}$$

Equation (3.51) is substituted into Eq. (3.52) to find after some manipulation:

$$\omega^2 = c^2 \left[k_x^2 \left(\frac{sin\left(\frac{k_x \Delta x}{2}\right)}{\frac{k_x \Delta x}{2}} \right)^2 + k_y^2 \left(\frac{sin\left(\frac{k_y \Delta y}{2}\right)}{\frac{k_y \Delta y}{2}} \right)^2 \right] \tag{3.53}$$

It is observed again that, in the limit $\Delta x \rightarrow 0$, $\Delta y \rightarrow 0$, Eq. (3.53) reduces to the exact dispersion relation $\omega^2 = c^2(k_x^2 + k_y^2)$.

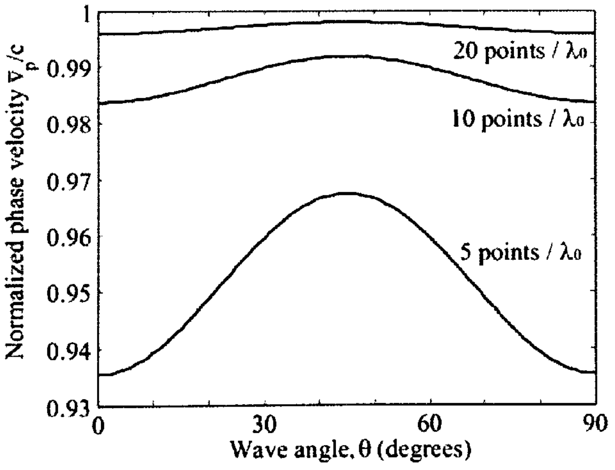

Figure 3.7 Dispersion of 2-D FDFD. Variation of numerical phase velocity with wave-propagation angle in a 2-D FDFD grid for three different cases of numerical resolution.

It can be seen from Eq. (3.53) that the numerical phase velocity $\tilde{v}_p$ for the 2-D case is a function of angle of propagation through the FDFD grid. To see this, wave propagation at an angle θ with respect to the positive x axis is assumed, in which case $k_x = k\cos(\theta)$ and $k_y = k\sin(\theta)$, where $k = \sqrt{k_x^2 + k_y^2}$ is the wave number. Fig. 3.7 shows a plot of normalised numerical phase velocity as a function of propagation angle θ. The dependence is, in general, relatively small (compared to dispersion errors due to the discretised grid), with $\tilde{v}_p/c$ varying by only a few percent between $\theta = 45^\circ$ and $\theta = 0^\circ$, even for very coarse (e.g., $\Delta x = \Delta y = \lambda_0/5$) spatial grids. The dependence of $\tilde{v}_p/c$ on propagation angle θ is known as grid anisotropy and is a source of additional numerical dispersion effects.

Finally, it is noted that, unlike FDTD, in FDFD only the spatial derivatives are approximated by finite differences. In fact, for time-harmonic sources and fields the FDTD equations reduce to the FDFD equations in the limit of $\Delta t \rightarrow 0$.

3.10 Boundary Conditions

To create a practical solver, the effects of the simulation boundaries should be considered. Basic beam propagation method (BPM) and FDM boundary conditions set the field just outside the simulation area to zero, simulating a perfectly conducting metal box. The perfect matched layer (PML) [60] is an artificial absorbing layer for wave equations, commonly used to truncate computational regions in numerical methods to simulate problems with open boundaries, especially in the FDM and FEM methods. The key property of a PML that distinguishes it from an ordinary absorbing material is that it is designed so that the waves incident upon the PML from a non-PML medium do not reflect at the interface. This property allows the PML to strongly absorb outgoing waves from the interior of a computational region without reflecting them back into the interior.

The PML was originally formulated by Berenger in 1994 [60] for use with Maxwell's equations, and since that time there have been several related reformulations of PML for both Maxwell's equations and for other wave equations. Berenger's original formulation is called a split-field PML, because it splits the electromagnetic fields into two non-physical fields in the PML region. A later formulation that has become more popular because of its simplicity and efficiency is called uniaxial PML or UPML [61], in which the PML is described as an artificial anisotropic absorbing material. Both Berenger's formulation and UPML were initially derived by manually constructing the conditions under which incident plane waves do not reflect from the PML interface from a homogeneous medium. However, both formulations were later shown to be equivalent to a much more elegant and general approach: stretched-coordinate PML [62, 63]. In particular, PMLs were shown to correspond to a coordinate transformation in which one (or more) coordinates are mapped to complex numbers. More technically, this is actually an analytic continuation of the wave equation into complex coordinates, replacing propagating (oscillating) waves by exponentially decaying waves. This viewpoint allows PMLs to be derived for inhomogeneous media such as waveguides, as well as for other coordinate systems and wave equations.

As an example for a PML designed to absorb waves propagating using the stretched coordinate system in the x direction, the following transformation is included in the wave equation. Wherever an x derivative $\partial/\partial x$ appears in the wave equation, it is replaced by [63]:

$$\frac{\partial}{\partial x}=\frac{1}{1+\frac{i\sigma(x)}{\omega}}\frac{\partial}{\partial x} \tag{3.54}$$

where ω is the angular frequency and σ is some function of x. This can be obtained by applying the following transformation to complex coordinates:

$x \rightarrow x+\frac{i}{\omega}\int \sigma(x)dx$ or equivalently $dx \rightarrow dx\left(1+\frac{i\sigma(x)}{\omega}\right)$. Therefore, wherever σ is positive, propagating waves are attenuated because:

$$e^{i(kx-\omega t)} \rightarrow e^{i(kx-\omega t)-\frac{k}{\omega}\int \sigma(x)dx} \tag{3.55}$$

where a plane wave propagating have been taken in the $+x$ direction (for $k > 0$).

3.11 Comparison to Other Numerical Techniques

FDFD is a frequency-domain technique, and can thus treat arbitrary material dispersion. Non-uniform and/or non-orthogonal grids are required in FDFD for efficient treatment of curved surfaces and rapid field variations at material interfaces. In FDFD, as in all other methods which are based on discretisation of the differential form of Maxwell's equations in a finite volume, absorbing boundary conditions (ABCs) are required, so that waves are not artificially reflected at the boundaries of the computational domain. Very efficient and accurate ABCs, such as the perfectly matched layer (PML) [55, 59] have been demonstrated for FDFD. As mentioned above, FDFD results in extremely sparse systems of linear equations. Such problems can be solved efficiently if direct or iterative sparse matrix techniques are used.

FDTD is also a finite-difference method, so its performance in modeling plasmonic devices is similar to the performance of FDFD. There are many similarities between the two techniques. Both can be used to model structures with arbitrary geometries. In addition, many of the methods used in combination with FDTD (total field/scattered field method, etc.) can also be used with FDFD. However, there are some major differences. First, as mentioned above, in time-domain methods the dispersion properties of metals have to be approximated by suitable analytical expressions which introduce substantial error in broadband calculations. In addition, the implementation of methods for dispersive materials in FDTD requires additional computational cost and extra memory storage [55, 64]. On the other hand, in FDTD it is possible to obtain the entire frequency response with a single simulation by exciting a broadband pulse and calculating the Fourier transform of both the excitation and the response [55].

The Finite-Element Frequency-Domain (FEFD) method is a more powerful technique than FDFD, especially for problems with complex geometries. However, FDFD is conceptually simpler and easier to programme. The main advantage of FEFD is that complex geometric structures can be discretised using a variety of elements of different shapes, while in FDFD a rectangular grid is typically used leading to staircase approximations of particle shapes [59, 65]. In addition, in FEFD fields within elements are approximated by shape functions, typically polynomials, while in FDFD a simpler piecewise constant approximation is used [65]. In short, FEFD is more complicated than FDFD but achieves better accuracy for a given computational cost [65].

3.12 Summary

In this chapter different computational techniques used to model plasmonic waveguide. These techniques can be divided into two types: frequency domain methods and time domain methods. In modelling of plasmonic waveguide it is preferred to use one of frequency domain methods. This is because permittivity of metal is complex and it depends on frequency. A novel nine node based full vectorial finite difference frequency domain method for linear oblique and curved interface has been presented. This method overcomes the staircase problem associated with conventional finite difference methods and also it gives better convergence and less computational time.

Chapter 4

Nonuniform Meshing Techniques for Plasmonic Waveguides

4.1 Introduction

The FDFD method as had been described in chapter 3 involves a regular, orthogonal grid of identical cells with dimensions $\Delta x, \Delta y, and\ \Delta z$ in Cartesian coordinates. Cylindrical and spherical coordinates can be used when the simulation space (and/or scattering structures) lends themselves more accurately to those coordinates. The resulting grids in cylindrical and spherical coordinates are orthogonal, but non-uniform, since the sizes of the grid cells varied with φ and θ. In addition, grids can be non-orthogonal or even unstructured. Many of these grid techniques can be used in the FDFD method; for example, an orthogonal, non-uniform grid, as described in the next subsection, can be easily implemented in FDFD. However, the more advanced techniques of non-orthogonal or unstructured grids become cumbersome in FDFD, and it is in those circumstances that finite volume or finite element methods are a better choice.

4.2 Nonuniform Orthogonal Grids

The FDFD algorithm lends itself to orthogonal grids, as the Yee difference equations are simplest to describe in the standard orthogonal coordinate systems. However, the grids can be made nonuniform quite easily. For example, while the Cartesian coordinate system is uniform, the cylindrical and spherical systems are nonuniform, as the grid cell sizes in φ and θ vary with distance. Other types of nonuniform, orthogonal grids are possible. The simplest example is a grid in Cartesian coordinates where the grid sizes $\Delta x,\ \Delta y, and/or\, \Delta z$ vary in their respective dimensions; an example is shown in Fig. 4.1. In this example, each spatial grid size varies along its respective direction, but each of the cells is still abutting rectangles. However, the usual centered difference approximations to the spatial derivatives in Maxwell's equations are no longer valid. To see this, notice that in the expanded cell in Fig. 4.1, the E_z component at the cell corner is no longer equidistant from the pairs of H_x and H_y components, so the "centred" nature of the difference equation is lost.

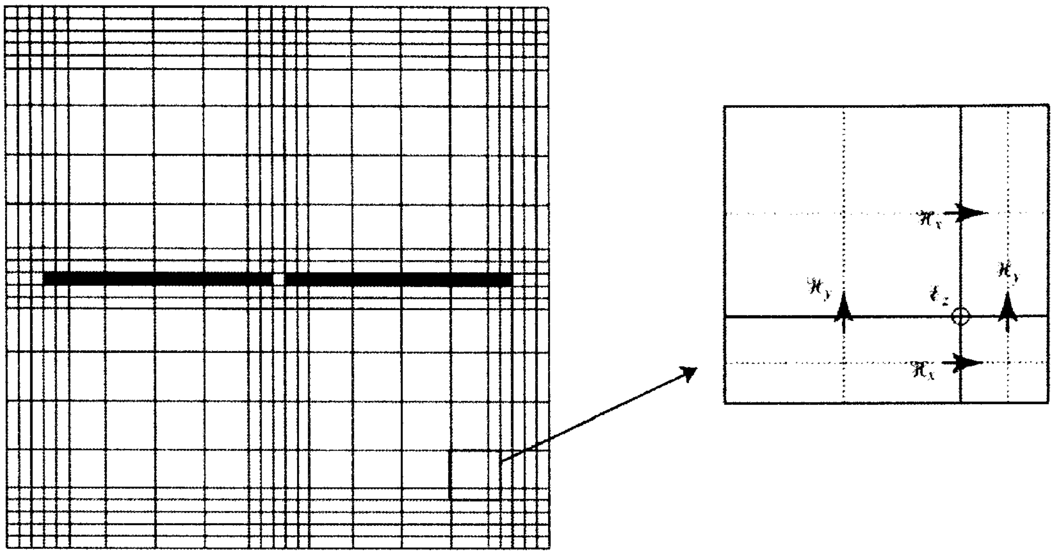

Figure 4.1 Nonuniform orthogonal mesh surrounding a two metallic thin films.

These types of cells require special handling through a new derivation of the difference equations, this takes into account the changing cell size and assigns $\Delta x_i \; and \; \Delta y_j$ to each location in the grid [66, 67]. This method reduces the simulation to first-order accuracy in these transition regions; however, Monk [66, 67] has shown that second-order accuracy is maintained globally.

4.3 Novel Graded Nonuniform Orthogonal Grids

Other types of nonuniform grids can be imagined; for example, one might use a grid of rectangular cells, but as the distance grows from the scattering object, larger rectangular cells size can be a factor of smaller cells size such that these cells form a geometric series with base Δx_0 and Δy_0in x and y direction respectively. The step size of cell i can be determined through equation (4.1):

$$\Delta x_i = \Delta x_0 (f_x)^i \\ \Delta y_j = \Delta y_0 (f_y)^j \tag{4.1}$$

Where f_x and f_y are arbitrary factors greater than one. Using this kind of meshing reduce the number of nodes in computational domain and thus reduce the computational time.

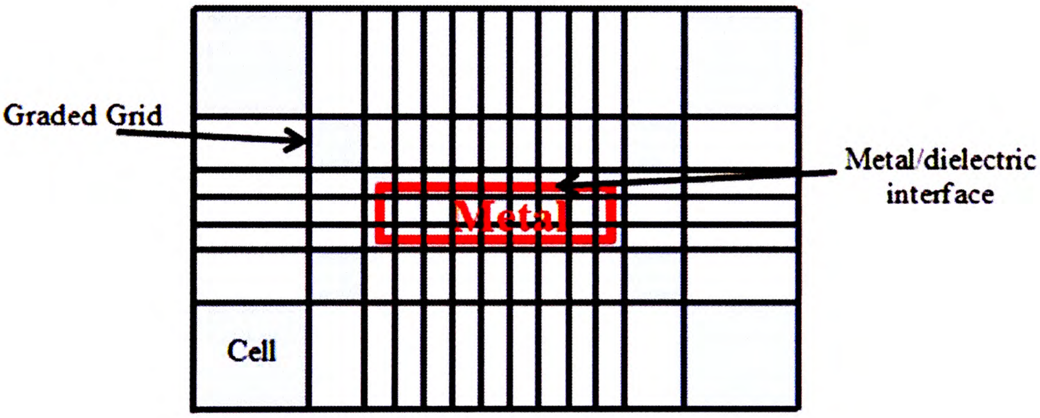

Figure 4.2 Nonuniform orthogonal graded mesh surrounding metallic thin film.

4.4 Adaptive Mesh Refinement

One highly advanced version of a nonuniform but orthogonal grid can be described through adaptive mesh refinement (AMR). In this method, the grid cell sizes are adapted as the fields propagate, so that where high gradients in the field (i.e., high frequencies) exist, smaller grid cells are used, but where the fields are zero or have low gradients (low frequencies), larger grid cells can be used. This is illustrated in Fig. 4.3. In this method, the grid is now dynamic, where until now we have discussed only static grids. In either the static, irregular grid or the dynamic AMR grid, one must treat the interfaces between coarse and fine grid cells carefully, as shown in Fig. 4.3. A number of different methods for interface interpolation have been used with success in different AMR algorithms [68].

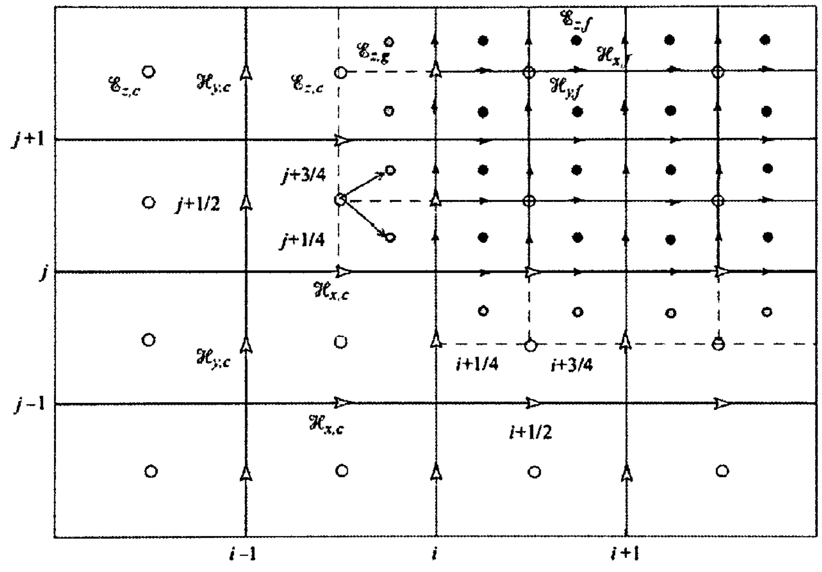

Figure 4.3 Grid-level boundaries in AMR. Interpolation and averaging of fields are required at the interface of different grid levels.

4.5 Nonorthogonal Structured Grids

One can easily devise a grid that is structured, but not orthogonal; furthermore, the grid does not need to be regular, in that adjacent cells are not the same shape as shown in Fig. 4.4. For example, the grid cells might be arbitrary parallelepipeds, the coordinates of which are the unit vectors along the edges of the cell. Such a grid structure can be easily conformed to structures within the simulation space. These types of grids are still structured, however, in that the vertices of the grid cells can be described by ordered arrays $x(i,j,k), y(i,j,k), and\ z(i,j,k)$ [69].

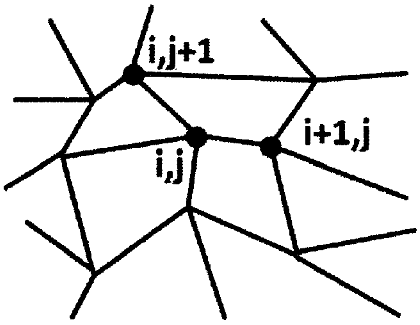

Figure 4.4 Nonorthogonal structured grid [69]

4.6 Unstructured Grids

In any discretised grid, consider the nodes of the grid to have locations (i,j,k). Fundamentally, a grid is considered structured if the nodes can be ordered; for example, (i,j,k) and $(i,j,k+1)$ are neighbors. This means that only the node locations themselves need to be defined, and it is assumed that each is connected to its nearest neighbours. In an unstructured grid, however, this assumption is not valid. As such, not only must the node locations be defined, but information about how they are connected must be provided. Unstructured grids provide complete freedom in conforming to material surfaces, and as such they provide the most powerful method for simulating detailed structures [69].

4.7 Novel Full Vectorial Finite-Difference Frequency Domain Method for Linear Oblique and Curved Interface

For the plasmonic waveguides, it is quite usual that the structure is piecewise homogeneous and thus contains a step refractive index profile. A general cross-sectional view of the structure is shown in Fig. 4.5 (a). The complete solution of the electromagnetic fields for such a problem is generally vectorial rather than scalar or semivectorial. Since the differential equations are approximated with their corresponding finite-difference equations in the FDM, the efficiency and accuracy of the FDM are greatly affected by its finite-difference (FD) formulae.

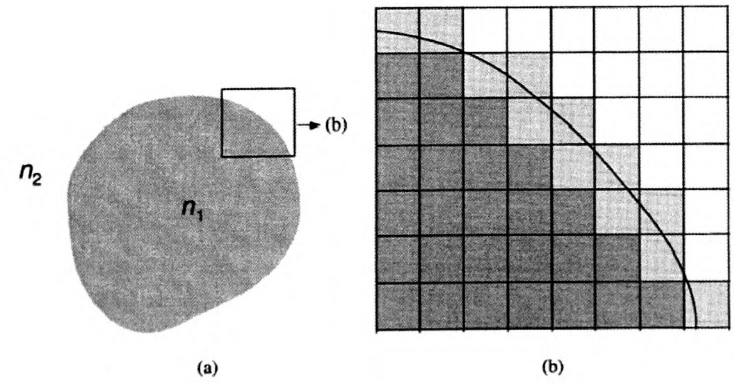

Figure 4.5 (a) Cross section of step index waveguide (b) Stair-case approximation for the oblique interface.

The simplest FD formula is based on the scalar approximation and it may not be sufficiently accurate when the polarisation-dependent characteristics of the structure need to be taken into account. Over the years, many approaches have been proposed to improve the efficiency and accuracy of the FDM, including semivectorial [70, 72] and full-vectorial [73, 71] formulations. In those formulations, the vectorial analysis usually starts from the following equation derived from Maxwell's equations:

$$\begin{bmatrix} a_{xx} & a_{xy} \\ a_{yx} & a_{yy} \end{bmatrix} \begin{bmatrix} E_x \\ E_y \end{bmatrix} = \beta^2 \begin{bmatrix} E_x \\ E_y \end{bmatrix} \tag{4.2}$$

where the differential operators are defined as

$$\begin{aligned}
a_{xx}E_x &= \frac{\partial}{\partial x}\left(\frac{1}{n^2}\frac{\partial(n^2E_x)}{\partial x}\right) + \frac{\partial^2 E_x}{\partial y^2} + n^2k_0^2E_x \\
a_{yy}E_y &= \frac{\partial}{\partial y}\left(\frac{1}{n^2}\frac{\partial(n^2E_y)}{\partial y}\right) + \frac{\partial^2 E_y}{\partial x^2} + n^2k_0^2E_y \\
a_{xy}E_y &= \frac{\partial}{\partial x}\left(\frac{1}{n^2}\frac{\partial(n^2E_y)}{\partial y}\right) - \frac{\partial^2 E_y}{\partial x\partial y} \\
a_{yx}E_x &= \frac{\partial}{\partial y}\left(\frac{1}{n^2}\frac{\partial(n^2E_x)}{\partial x}\right) - \frac{\partial^2 E_x}{\partial x\partial y}
\end{aligned} \tag{4.3}$$

where β is the modal propagation constant, n is the transverse refractive-index function, and is the free-space wavenumber. Note that $a_{xx} \neq a_{yy}$ causes the polarisation dependence, whereas $a_{xy} \neq 0$ or $a_{xy} \neq 0$ induce polarisation coupling between E_x and E_y. Conventional FD schemes are obtained by directly discretising equations (4.3) with the graded-index approximation at the interface. The graded-index approximation assumes that the transverse refractive-index function is graded varying and continuous across the interface. The conventional FDMs are generally arranged in such a way that the fields are continuous in the first partial differential operation in order to avoid the discontinuity problem at the interface. However, the second-order partial differential operation still can only be approximated by the graded-index assumption. Recently, some modified treatments have been presented to deal with optical waveguides with step-index profiles [70-78]. Most of the improved formulae have been constrained to semivectorial cases. Although some of them are full-vectorial in nature, in those formulations the improved FD formulae were still substituted back into the above equations based on the graded-index approximation in order to evaluate the coupling term between the two polarization components of the field [71].

Besides the step-index interface problem, the rectangular meshes usually used in the FDM cause another problem in the FDM when the structure contains oblique or curved interfaces, as shown in Fig. 4.5 (b). The conventional treatment is to use either the graded-index approximation or the staircase index approximation. Vassallo [71] derived an improved FD formulation considering an oblique interface, but the formulation is only suitable for the scalar case and the truncation error is of the first order at best. In his treatment of the semivectorial case, the structures were only allowed to have discontinuities directed along either the x or y axes, just like other semivectorial Formulations.

In this dissertation, improved FD formulations had been derived which can treat optical waveguides with step-index profiles. The formulations are full-vectorial ones and the interface can be oblique to the x and y axes. The process of derivation is similar to

Vassallo's [71] in that perform the Taylor series expansion and then match the interface conditions have been employed. To obtain a full-vectorial formulation that can treat the oblique interface, further the local coordinate transformation is introduced and a rigorous expressions for the interface conditions in the locally transformed coordinate is derived. Although matching interface conditions, the coupling between the two transverse polarization components of the field will be automatically included in the resultant FD formulae.

A general relation between the field $\varphi_s|_{(m,n)}, s = x \; or \; y$ at the sampled point (m, n) and the fields nearby, as shown in Fig. 4.6 for a linear oblique interface is derived in this section.

Starting from Maxwell's equations, the vector wave equation for the magnetic field vector, H, can be derived as $\nabla \times (\varepsilon^{-1} \nabla \times H) - \omega^2 \mu_0 H = 0$ (1)

$$\nabla \times (\varepsilon^{-1} \nabla \times H) - \omega^2 \mu_0 H = 0 \qquad (4.4)$$

where ω is the angular frequency, μ_0 is the permeability of free space, and ε is the permittivity tensor of the waveguide material which is given by $\varepsilon = \varepsilon_0 \varepsilon_r$ where ε_0 is the permittivity of free space, and ε_r is the relative permittivity tensor of the waveguide material. The formulation of the method is based on nine mesh points. The relation between the fields as shown in Fig. 4.6 at the nearby point $(m + 1, n + 1)$ with the fields $\overline{H}_x, \overline{H}_y$ and the their derivatives at the sampled mesh points (m, n) is

$$\overline{H}_{(m+1,n+1)} = \overline{\overline{D}}_{(m+1,n+1)} \cdot \overline{H}_{(m,n)} \qquad (4.5)$$

where

$$\overline{\overline{D}}_{(m+1,n+1)} = \overline{\overline{D}}_{(m+1,n+1)R} \cdot \overline{\overline{D}}_{RC} \cdot \overline{\overline{D}}_{RL} \cdot \overline{\overline{D}}_{CL} \cdot \overline{\overline{D}}_{L(m,n)} \qquad (4.6)$$

The relation between the above mentioned fields and their derivatives can be illustrated as [19]

$$\overline{H}_{(m+1,n+1)} \xleftrightarrow[\overline{\overline{D}}_{(m+1,n+1)R}]{TES} \overline{H}\Big|_R \xleftrightarrow[\overline{\overline{D}}_{RC}]{LCT} \hat{H}\Big|_R \xleftrightarrow[\overline{\overline{D}}_{RL}]{MBC} \hat{H}\Big|_L \xleftrightarrow[\overline{\overline{D}}_{CL}]{LCT} \overline{H}\Big|_L \xleftrightarrow[\overline{\overline{D}}_{L(m,n)}]{TES} \overline{H}_{(m,n)} \qquad (4.7)$$

where TES denotes Taylor series expansion, LCT denotes local coordinate transformation, and MBC denotes matching the boundary conditions. After connecting the fields and their derivatives at the mesh point (m, n) to the nearby eight mesh points and using equation (4.4) the following equation obtained:

$$D.\begin{bmatrix} H_x\big|_{(m-1,n+1)} \\ \vdots \\ H_x\big|_{(m+1,n-1)} \\ H_y\big|_{(m-1,n+1)} \\ \vdots \\ H_y\big|_{(m+1,n-1)} \end{bmatrix} + k_0^2 \varepsilon_{(m,n)} \begin{bmatrix} H_x\big|_{(m,n)} \\ H_y\big|_{(m,n)} \end{bmatrix} = \beta^2 \begin{bmatrix} H_x\big|_{(m,n)} \\ H_y\big|_{(m,n)} \end{bmatrix} \qquad (4.8)$$

where D is a 2×18 matrix containing entries obtained from the derived new FD formulae, and $\varepsilon_{(m,n)}$ denotes the relative permittivity at the point (m, n).

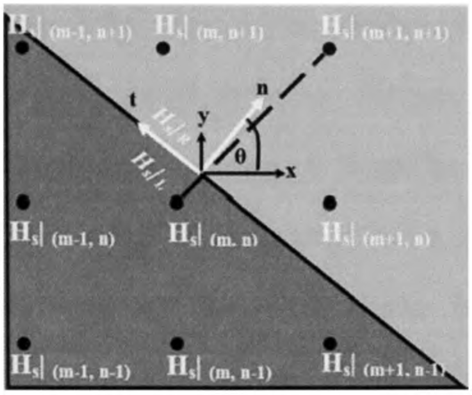

Figure 4.6 Cross section of Linear Oblique Interface

By assembling the fields at all sampled points in the computation domain as

$$\widetilde{H} = [H_x|_{(0,0)}, \ldots, H_x|_{(M,N)}, H_y|_{(0,0)}, \ldots, H_y|_{(M,N)}]^t \tag{4.9}$$

and applying (4.8) together with suitable boundary conditions, we obtain an algebraic eigenvalue equation

$$\begin{bmatrix} A_{xx} & A_{xy} \\ A_{yx} & A_{yy} \end{bmatrix} \begin{bmatrix} H_x \\ H_y \end{bmatrix} = \beta^2 \begin{bmatrix} H_x \\ H_y \end{bmatrix} \tag{4.10}$$

where β is the propagation constant and the differential operators Axx, Axy, Ayx and Ayy result from the operator $\partial^2/\partial x^2 + \partial^2/\partial y^2$ on H and their elements can be obtained from the elements of the matrix D. Equation (4.10) is a full-vector eigenvalue equation, which describes the modes of propagation for the optical waveguides. The two transverse field components H_x and H_y are the eigenvectors, and the corresponding eigenvalue is β^2. The differential operators can be approximated by using the finite difference methods [45] and the robust perfectly matched layer (PML) boundary condition [63] is employed at the edges of the computational window in order to account for the leakage property of the modes. In addition, non-uniform meshing is used in order to get accurate modelling results. It should be noted that the full vector eigenvalue equation is solved numerically for a set of modes, and the dominant mode is defined as the mode with the highest real effective index value. Since, $\nabla.H = 0$ and interface boundary conditions are automatically satisfied in the formulation, then there is no chance for spurious (nonphysical) modes to appear in the spectrum of the solution.

4.8 Summary

Through this chapter different meshing techniques have been presented. Meshing techniques in general can be divided into uniform mesh or non-uniform mesh. Non-uniform mesh decreases the computational time efficiently; but it is more complex to be implemented. A novel graded non-uniform mesh has been presented. This graded mesh provides a very fine mesh at metal/dielectric interface where the surface plasmon modes generated. While the mesh size increases gradually away from the interface to decrease the number of mesh points and hence decrease the computational time

Chapter 5

Channel and Wedge Plasmon Polaritons

5.1 Introduction

This chapter presents the electromagnetic modes guided by metallic grooves and wedges. Various approaches employed for the computation of the electromagnetic field in such structures are presented. The wave guiding properties are obtained by electrodynamics techniques. Dispersion, modal size, shape, polarisation, and propagation length of these modes is presented. It is concluded that both channel and wedge modes are well confined with reasonable losses, wedge structures being favourable in terms of modal size.

Channel plasmon polaritons (CPPs) are electromagnetic modes supported by grooves carved in metallic surfaces whereas wedge plasmon polaritons (WPPs) are the corresponding modes sustained by metallic wedges. One can say, without being too precise at this point, that the electromagnetic field of CPP and WPP modes is guided along the bottom of the groove or the edge of the wedge, respectively. For reasons discussed in the next paragraph, these modes have received quite a lot of attention in the last 10 years. This chapter is devoted to a description of the guiding properties of CPPs and WPPs.

There has been an interest in the behaviour of electromagnetic fields next to corners and edges for a long time. The first report dealing with these geometries within the context of surface plasmons was published by Maradudin and Coworkers [79]. The mentioned paper considers an idealized geometry in the electrostatic approximation. The next landmark, in 2002, was a complete treatment including retardation and for realistic geometries [80]. After this, the number of works, both theoretical and experimental, reporting on CPPs and WPPs increases rapidly. The following reasons for this late interest can be summarised as follows. First, from a general point of view, in the last ten years or so the field of plasmonics has blossomed and various SPP-based waveguiding schemes are being considered. The achievement of tightly confined modal fields and long propagation lengths count among the main design goals. CPPs and WPPs feature good confinement and a reasonable propagation length, and are therefore promising candidates. Secondly, the planar paradigm is preferred from a technological perspective, and the modes studied in this chapter fit well with planar metallic structures. In spite of the difficulties to fabricate narrow angle CPPs and WPPs, these have been already demonstrated and CPP-based functional devices have been reported [7]. Finally, from a more fundamental point of view, edges and corners appear whenever a flat surface is folded. In this sense CPPs and WPPs constitute building blocks that show up in other kinds of plasmonic guides such as stripes, trenches, gaps, and so on. Thus, understanding the properties of CPPs and WPPs is very useful for the design of most of the remaining plasmonic waveguides.

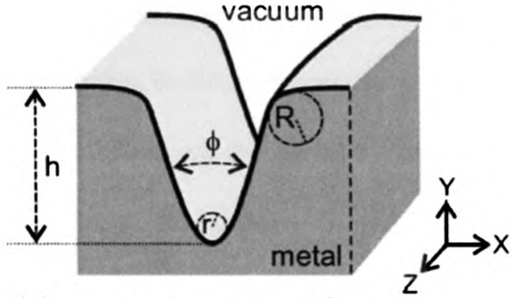

(a) groove carved in surface

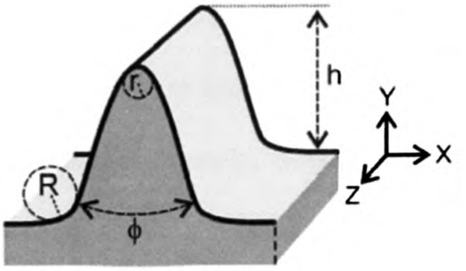

(b) wedge grown on surface

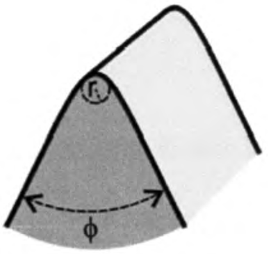

(c) infinite wedge

Figure 5.1 Schematics of structures support channel and wedge plasmon polaritons.

5.2 Approximate Approaches

Fig. 5.1 displays examples of the structures being analysed, and the definition of coordinates and geometric parameters. These structures of two different kinds: structures truncated at a certain height $y = h$ [Figs. 5.1(a) and (b)], and idealized non-truncated structures where $h \rightarrow \infty$ and the inclined sides of the groove or wedge are infinitely extended [Fig. 5.1(c)]. The modes corresponding to non-truncated structures called CPP(∞) and WPP(∞). In most cases the lateral sides of the groove or wedge are approximately flat and form an angle denoted by $\emptyset$. Corners and edges shall be rounded and the corresponding radii of curvature are denoted as r or R. The chosen radii are always larger than 5 nm. With this election, the minimum feature size of the structures is sufficiently large so as to use bulk dielectric functions in the metal. Notice that, for small feature sizes (radii smaller than about 2 nm), one has to take into account more complex effects in the dielectric function of the metal. Namely, a size-dependent damping due to electron scattering at the metal surface, or/and a non-local behaviour of the permittivity of the metal $\epsilon_r(\omega, k), \omega$ and k being the frequency and wave vector, respectively. In addition, it should be mentioned that smaller radii are extremely difficult to fabricate.

We shall be concerned with modes propagating along the Z axis and confined in the transverse XY plane. The determination of the modes supported by the considered structures requires the resolution of Helmholtz equation for the electromagnetic fields in vacuum and metal, supplemented by the boundary conditions at the interfaces.

5.3 The Electrostatic Limit

The simplest approximation consists in disregarding retardation. In this limit, Helmholtz equation is replaced by Laplace equation. There are some wedge (or groove) geometries for which the equation can be solved analytically, the easiest one being a sharp ($r = 0$) wedge, with flat sides and infinite height $\left(h \to \infty\right)$, see Fig. 5.1(c). Laplace equation for this configuration can be separated in polar coordinates and was considered in [79]. The corresponding solution is attractive of being very simple but it has two important problems. First, the fields are divergent at the tip of the structure, and second, the computed modes do not have a standard dispersion relation $\omega = \omega(k_z)$, where ω and k_z are the frequency and modal wave vector, respectively. It was soon realised [81] that both defects are due to the infinitely sharp tip. In the following years analytical solutions for wedges with rounded edges (corresponding to parabolic [82] and hyperbolic [83] cross sections) were computed, and it was shown that the mentioned difficulties no longer occur. However, it can be seen [9] that the dispersion relation obtained within this framework is not a good approximation when it is close to the light line. This regime turns out to be the most interesting one, and for this reason the remaining approaches take into account the finite propagation speed of the electromagnetic fields.

5.4 Geometric Optics Approximation and Effective Index Method

The geometric optics approximation (GOA) and the effective index method (EIM) have been used to understand several aspects of the behaviour of Electromagnetic fields in grooves and wedges. Their main merit is that they allow one to obtain important properties of the electromagnetic field and, moreover, they are not complex numerical techniques [84, 85].

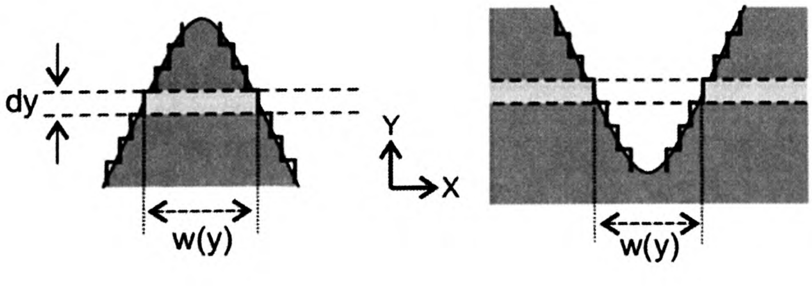

Figure 5.2 Stack of variable width metallic films (left) or gaps (right)

For both approaches it is useful to consider the wedge (respectively groove) as a vertical stack of metallic films (respectively vacuum gaps in a metal) with infinitesimal vertical thicknesses, and horizontal widths depending on the vertical coordinate $w(y)$, see Fig. 5.2.

The effect of the varying width of the wedge (or groove) is taken into account by considering the modes supported by the infinitesimal slices. The dispersion relations of the first modes supported by a metallic film or gap with constant width w is plotted in Fig. 5.3 for several widths (for the sake of simplicity the dielectric constant of the metal is represented by a Drude model with a typical plasma frequency $f_p = 1.91 \times 10^{15} s^{-1}$ and no absorption).

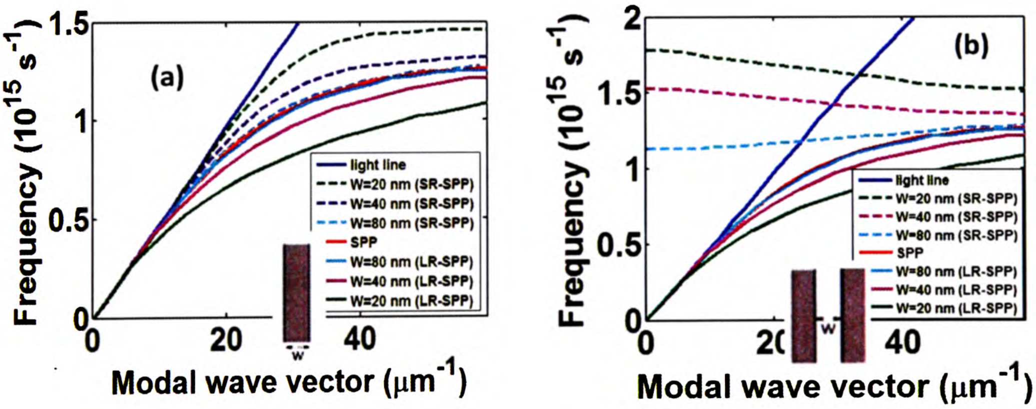

Figure 5.3 Dispersion relation for plasmonic modes supported by (a) film, and (b) gap, both of width w.

As it is well known, for increasing width the SPP modes at both interfaces decouple and the modal dispersion relation tends to that of a single SPP on a flat interface. In the case of the film, those modes below the SPP curve have even parity with respect to symmetry plane (they are named Short Range Plasmon Polaritons). On the other hand, the gap modes below the SPP curve have odd parity. For both configurations, the modes below the SPP curve become more and more separated from the dispersion relation of a SPP as the width w decreases. In other words, at a given frequency the modal effective index $n_{eff} = k_z/k_0$, k_0 being the wave vector in vacuum) of these modes depends on the width, $n_{eff}(w)$ increasing as the width decreases. This is the necessary behaviour to achieve field confinement at the bottom of the grooves (or the edge of the wedges), where the width is smaller. The reason is that the modes corresponding to a small width $w_<$ are outside the dispersion curve corresponding to a larger width $w_>$. Thus, the former modes are evanescent along the vertical direction in the gap (or film) of width $w_>$ and are therefore vertically confined.

The geometric optics approximation and the effective index method are based on the above explained behaviour of the effective index of the modes supported by a gap or a film. In both approaches the groove (or wedge) is replaced by a dielectric medium the refractive index N of which is non-homogeneous and is defined as follows: (i) N is constant in the horizontal (XZ) planes, and (ii) $N(y) = n_{eff}(w(y))$. Notice that the modal effective index $n_{eff} \rightarrow \infty$ as $w \rightarrow 0$ so that $N(y)$ diverges at a height y corresponding to the structure tip, Figs. 5.4(a) and (b).

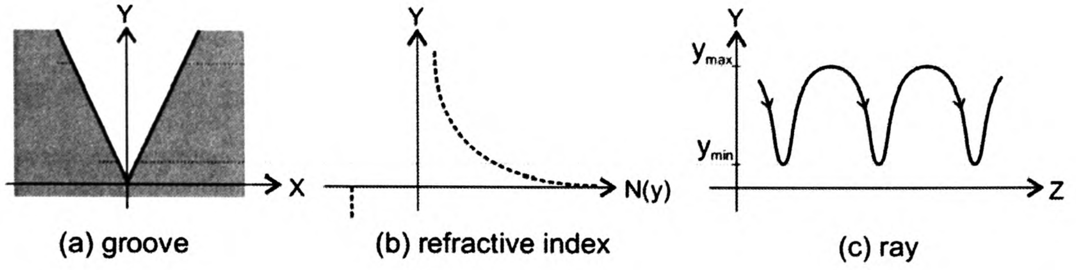

Figure 5.4 Geometric optics approximation: (a) groove geometry, (b) refractive index $N(y)$ of equivalent medium, (c) ray path corresponding to guided mode.

The GOA consists in the optics of rays (representing the propagation direction of gap plasmons) in the mentioned non-homogeneous dielectric medium. It predicts the important properties that the rays bend toward the tip, slowing down while the corresponding field amplitude increases, leading to a Nano focusing effect. Within this picture a guided mode corresponds to a ray progressing along the Z coordinate while bouncing back and forth between two heights y_{min}, y_{max} . The lower height y_{min} corresponds to the point where the adiabatic approximation of GOA breaks down and the ray is reflected, Fig. 5.4(c). Thus, guided modes are consistent with the GOA but their properties cannot be determined within this framework [86, 87].

The EIM solves numerically the one dimensional Helmholtz equation in the mentioned non-homogeneous dielectric medium. The basic formulation assumes that the electromagnetic field has the same vector components as the gap (or film) plasmonic mode, i.e., Hy, Ex, Ez, having transverse magnetic (TM) character. In this fashion a dispersion relation, propagation length, and vertical modal profile can be found [87, 88]. This is a very useful approach but there are a number of issues to be improved. First, the computed dispersion relation and propagation losses are approximate. For CPPs, in most cases, the results are surprisingly good, but for WPPs the approximation is worse. This is most likely due to the fact that the assumed polarisation is (approximately) the correct one for CPPs whereas it is not correct (near the tip) for WPPs.

Second, the two-dimensional modal shape and polarisation cannot be computed. This impedes the quantitative computation of the coupling of the mode with external incident fields. Third, for grooves truncated at a finite height $y = h$, two additional side edges appear that sustain WPP modes.

This effect, substantially modifies modal shape, size, polarisation, and propagation length, and cannot be accounted for within this approximation. Finally, the divergence of $N(y)$ at the tip of the structures leads to some questions (not yet definitively answered within the EIM) about the value of the field at this location [87].

For the explained reasons, the above described approximate techniques are not completely adequate to determine the properties of CPP and WPP modes.

5.5 Rigorous Techniques Basic Structures

There are a few rigorous methods that have been applied for the computation of CPPs and WPPs. The first one is using the finite-difference time-domain algorithm described in an early paper dealing with retarded WPP modes [85]. The technique is accurate, but it is designed for a very specific geometry (parabolic cross section cylinder). A method valid for generic geometries (based on Green's second integral identity) was presented by Maradudin and coworkers [79]. Since then various general purpose numerical techniques have been used to study CPPs and WPPs, such as the Multiple Multipole (MMP) method, the Finite Differences in Time Domain (FDTD) technique, and the (FE) method. In addition, a modal expansion method was reported in [88]. The structures are made of gold in vacuum. The dielectric constant of gold is represented by a Drude-Lorentz model (including absorption), which nicely fits the well-known experimental data of Johnson and Christy [69] in the spectral range considered here, $\lambda \in [0.6\mu m, 1.6\mu m]$ The structures considered in this section are not truncated $(h \to \infty)$.

5.6 Dispersion

Fig. 5.5 and 5.6 render the dispersion relation corresponding to CPP(∞) and WPP(∞) modes. There corresponds to bound modes and they are outside the light line and outside the dispersion curve of a SPP on a flat surface, i.e., outside the shaded regions in these figures (otherwise the mode would be radiated either to free space or along the metallic interface). The modes are very close to the SPP curve at telecom wavelengths rendering the electrostatic approximation inadequate to determine accurate values of the dispersion relation.

For high frequencies the dispersion relation is far from the light line which means that the modes are well confined at the tip of the structures. On the other hand the modal size increases for small frequencies. Let us mention that this behaviour imposes stringent conditions on the mesh size, and the size of the simulation window. For high frequencies a very fine mesh was needed (for FDTD the results were converged for a mesh size of 5 nm), whereas large simulation windows were needed for small frequencies (for MMP the size has to be much larger than the modal size). In the small frequency regime the size of the numerical problem rapidly increases, and for this reason it is very difficult to demonstrate numerically that the modes have no cut-off (and are asymptotic to the light line). However, we never found a cut-off and the exact electrostatic solutions suggest that none exists.

Fig. 5.5 displays the first two CPP(∞) modes but it is clear that the structure supports an infinite number of them, higher order modes having larger modal size. The modes corresponding to the curves have odd parity. On the other hand Fig. 5.6 displays a single WPP(∞) mode of even parity. Actually, higher WPP(∞) modes exist, but they appear for very high frequencies, outside the scale of the diagram. These higher order modes are very much confined at the tip (in the region where the structure is rounded) but, unfortunately, they are extremely lossy and thus useless for guiding purposes [89].

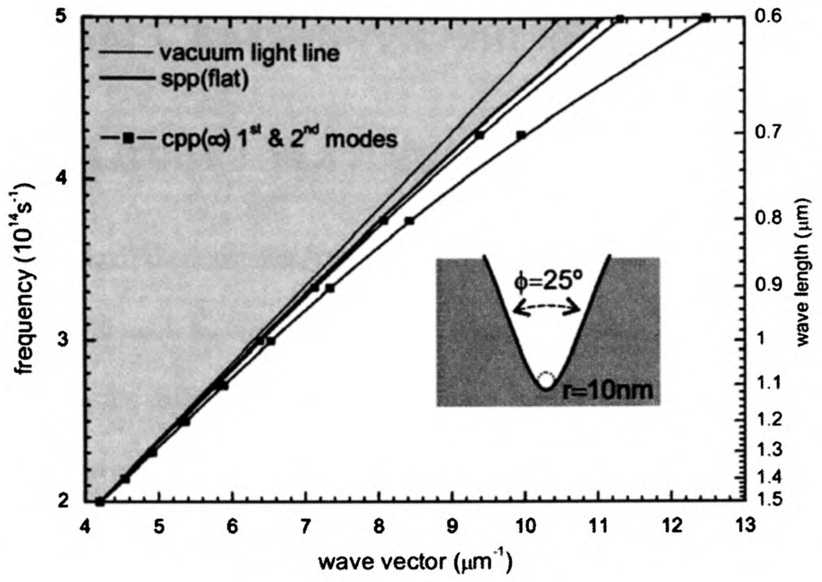

Figure 5.5 Dispersion relation of CPP(∞) modes. The groove angle is φ = 25. The radius of curvature of the tip is r = 10 nm.

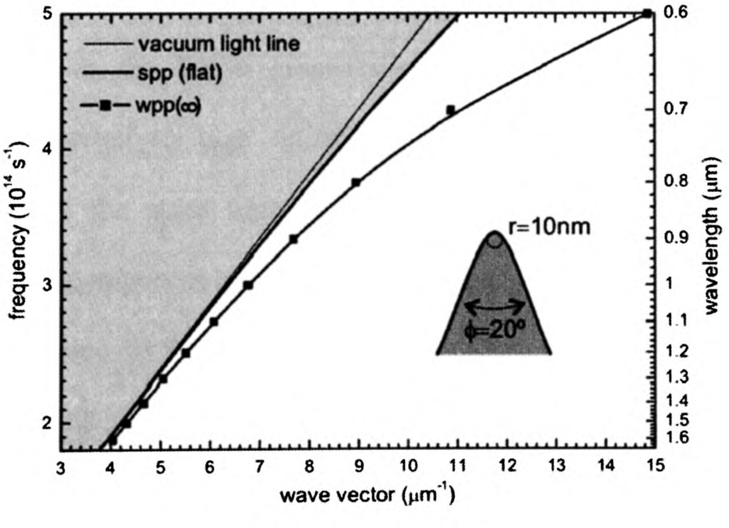

Figure 5.6 Dispersion relation of a WPP(∞) mode. The wedge angle is φ = 20. The radius of curvature of the tip is r = 10 nm

5.7 Accurate Characterisation of a Novel Three-Trenched Groove Waveguide

Many optical devices operate on telecommunication wavelength nowadays depends on the CPP such as waveguide bends, splitters, interferometers, and resonators [7, 90-94]. Among the different structures that have been proposed, there have been two representative groove types, triangular (V-shaped) groove and rectangular (trenched) groove [90]. The simplest structure of the CPP is the rectangular groove. In any CPP there is always a trade-off between confinement of the field inside the groove and the propagation loss [91]. The propagation loss of the wide groove CPP is smaller than that of the narrow groove CPP with the same depth. However, the field confinement factor of the narrow groove CPP is smaller than that of the wide groove CPP. On the other hand for fixed width, the deeper groove shows high confinement factor while the propagation loss is relatively high. So in order to get high field confinement and low propagation loss at the same time the trenched groove must be wide and deep. Therefore, the CPP component length will be increased and the ability of implementing ultra-compact photonic-device [90] will be limited. One of the most popular CPP is the V-shaped groove which is drilled in the top side of the metal [92]. Its popularity came from the fact that it is the most efficient groove which has well confined field inside the groove. However, it has a moderate propagation length.

In this thesis a novel full-vectorial finite difference method for linear oblique and curved interfaces (FVFD-LOCI) [78] is used to model the V-Shape groove, rectangular groove and the proposed structure. FVFD-LOCI method overcome the step index problem as well as the oblique or curved interface problem. In order to get accurate results a non-uniform meshing is used, so that a high condensed meshing is applied in the expected field regions and a low condensed meshing is applied in the empty field regions.

A comprehensive study has been done to investigate the dispersion characteristics of a novel design of CPP based on three-trenched-type groove. The simulation is performed by the full vectorial finite difference method (FVFDM-LOCI) [78] with non-uniform graded meshing capabilities. The analysed parameters are effective index n_{eff}, propagation length, lateral mode radius r_{3dB} and figure of merit (FOM). The suggested symmetric three trenched design shows a very good confinement behaviour which is relatively close to V-shape while the propagation length is greatly improved. The FOM can be adapted and controlled by changing the groove widths and depths. Therefore, a three trenched CPP waveguide with very high FOM can be implement at a certain band of frequency. In addition, the three trenched fabrication process is much easier than that of the V-shaped groove and narrow deep trenched groove. At the fabrication process V-shaped groove has a curved edges and a curved bottom. For $\lambda \in (0.6\,\mu m, 0.8\,\mu m)$, the dispersion relation is extremely sensitive to the fine details of the groove bottom.

5.8 Numerical Results

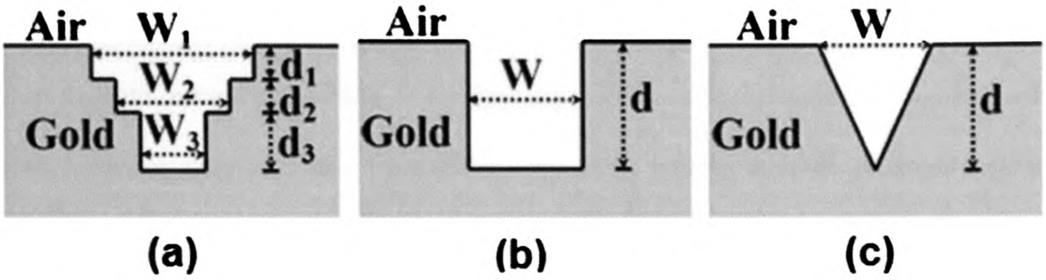

Figure 5.7 Schematic diagram of (a) novel three-trenched groove structure (b) conventional rectangular structure (c) V-shaped structure

Fig. 5.7(a) shows the suggested novel three-trenched groove CPP structure. The reported CPP consists of three-trenches drilled vertically on the top surface of the gold metal with three different widths $W_1, W_2\ and\ W_3$. The depths of each groove are $d_1, d_2, and\ d_3$. However, the conventional rectangular structure and V shape structure are shown in Fig. 5.7(b) and Fig. 5.7(c), respectively.

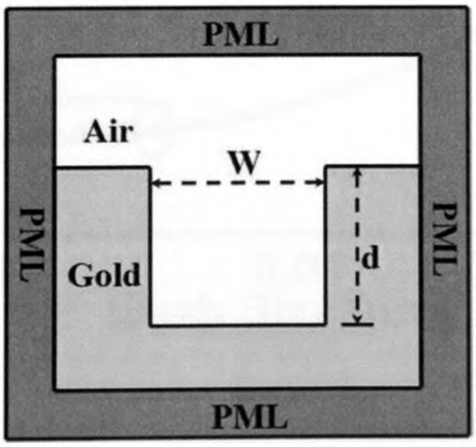

Figure 5.8 PML setting for trenched groove

In order to have fixed computational domain, all sides are truncated with the PML which plays an essential role in the calculation. The PML as shown in Fig. 5.8 is used to prevent any interference resulting from the radiating wave reflections at computational boundaries. PML is needed due to the wide difference in the refractive index between gold and air. In addition, the field widely spreads when the cut-off occurs and the mode transfers from CPP mode (gap mode) to another type of SPP mode (surface mode). FVFD-LOCI method [78] is used in order to get accurate results in a reasonable computational time specially when we do simulation for V-groove structure with oblique interface.

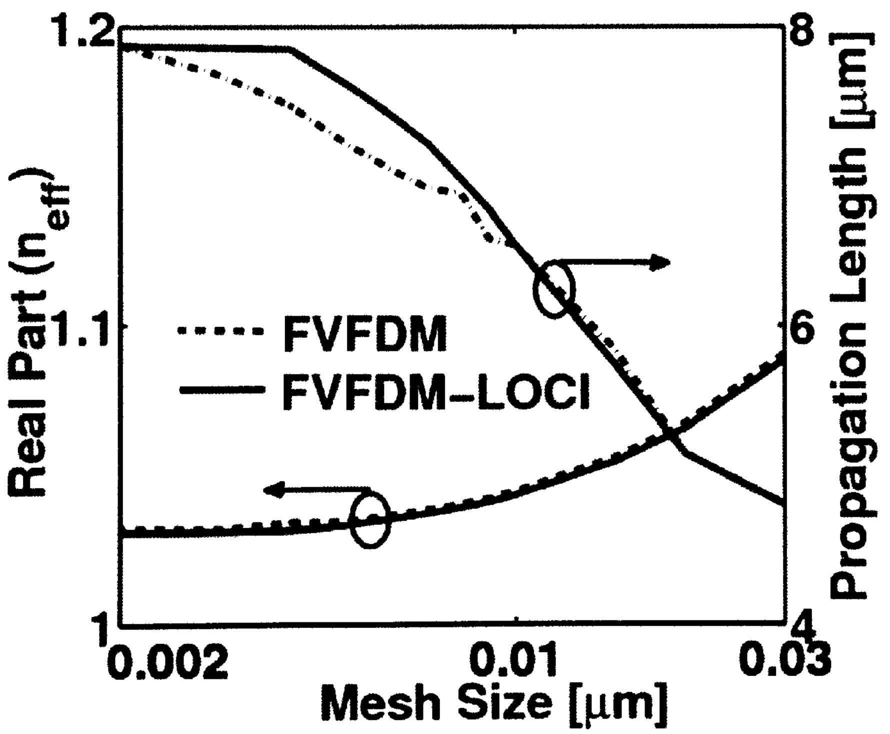

Figure 5.9 Variations of the propagation length and effective index of the V-shaped structure with the meshing size

Fig. 5.9 shows the variation of the propagation length and real part of complex effective index n_{eff} of the V-shaped structure with the meshing size using conventional FVFDM [45] and FVFDM-LOCI [78]. In this study, the meshing size Δx in x direction is equal to meshing size Δy in y direction. In addition, the width W and depth d of the V grove are taken as 0.5 μm, 1.2 μm, respectively. It is revealed from Fig. 5.9 that the FVFDM-LOCI is more accurate than the conventional FVFDM in studying the CPP with oblique interfaces. As the meshing size decreases, n_{eff} decreases while the propagation losses increases until convergence occurs at meshing size of $\Delta x = \Delta y = 0.003\ \mu m$. Therefore, meshing size $\Delta x = \Delta y = 0.003\ \mu m$ is used in the subsequent simulations throughout this work. The refractive index of Gold is calculated using extended Drude Model.

Throughout this work, the propagation length L_{prop} is defined as:

$$L_{prop} = \frac{1}{Im\left\{\frac{\beta}{k_0}\right\}} \tag{5.1}$$

In addition, the effective index n_{eff} can be calculated from the complex propagation constant β and free space wave number k_0 as follows

$$n_{eff} = Re\left\{\frac{\beta}{k_0}\right\} \tag{5.2}$$

5.8.1 Modal Analysis for Conventional CPP Waveguides

Initially, the V-groove and rectangular groove waveguides are considered and studied. In this evaluation, the depth of both waveguides are fixed to d = 1200 nm. In addition, the V-groove waveguide width is fixed to W = 500 nm. However, the rectangular groove waveguide is studied using three different widths; 120 nm, 300 nm and 500 nm. Fig. 5.10 (a) and (b) show the variation of real part of effective index n_{eff} and propagation length with the frequency for the V-groove and rectangular groove with three different widths, 120 nm, 300 nm, and 500 nm.

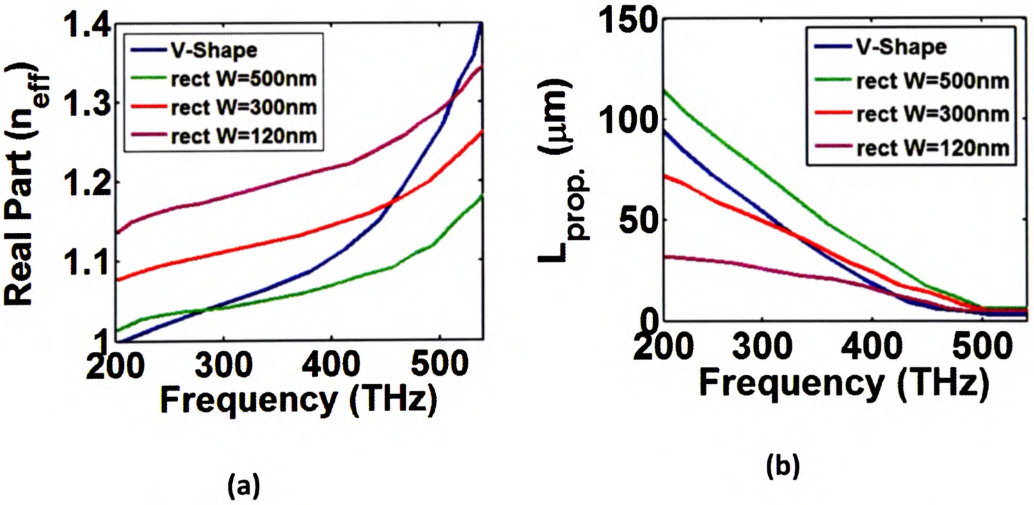

(a)

(b)

Figure 5.10 Variation of (a) real part of effective index n_{eff} and (b) propagation length with the frequency for the V-groove and rectangular groove with three different widths, 120 nm, 300 nm, and 500 nm.

It is revealed from Fig. 5.10 (a) that the real part of n_{eff} of the trenched groove decreases as the groove width increases. As the groove width increases the field starts to be less confined inside the groove. In addition, the field starts to go up towards the groove opening which has relatively less effective refractive index compared to the bottom zone of the groove. It is also evident from Fig.5.10 (a) that n_{eff} of the trenched and groove increases by increasing the frequency. As the frequency increases, at fixed groove width, the launched wave wavelength decreases and the field starts to be more confined inside the groove and hence n_{eff} increases.

Fig.5.10 (a) also reveals that n_{eff} of the V-shaped groove is bounded between that of the narrow trenched groove width W = 120 nm and that of the wide width W = 500 nm in the frequency range from 300 TH to 500 TH. However, n_{eff} for the V-shaped groove at low frequency $f < 300\,THz$ is smaller than that of wide trenched groove because the V-shaped becomes shallower than that of trenched groove. At high frequency $f > 500\,THz$, n_{eff} of the V groove is greater than that of the narrow groove because the field starts to be well confined inside the very small sharp groove.

It is also shown from Fig. 5.10 (b) that the propagation length for the wide trenched groove waveguide is greater than that of the narrow trenched groove. The mode of the wide groove is confined in the upper region of the groove at which the damping loss is smaller than that of the narrow groove. The damping loss at the bottom is higher than that of the top region of the groove. This is due to the high variation in refractive index between air and gold in the bottom region at which the air is surrounded by gold from three directions. As the frequency is increased the wavelength of the propagating wave is decreased. This means that the mode will be more confined inside the groove and has more damping loss. Fig. 5.10 (b) also reveals that the V-shaped groove shows a moderate propagation loss in the frequency range $f < 400THz$. However the propagation length at frequency $f > 400THz$ is smaller than that of narrow trenched groove. This is due to the high confinement of the field in the small cross section near the bottom of the groove which has high damping loss.

There is always a trade-off between the confinement of the field inside the groove and the propagation loss caused by that groove. So in order to choose the better groove, one must compromise between its propagation length and the confinement of the field inside the groove. The confinement of the field inside CPPs waveguides based on air groove can be well explained by studying the lateral (parallel to the x-axis) mode radius $r_{3\mathrm{dB}}$ which is defined as the distance of -3dB power drop point from the waveguide symmetrical plane. In addition, to compare between several configurations, figure of merit (FOM) has been used and defined as,

$$\mathrm{FOM} = \frac{\text{Propagation Length}}{\text{Lateral mode radius}} = \frac{L_{prop}}{r_{3dB}} \tag{5.3}$$

Fig. 5.11 shows the variation of lateral mode radius $r_{3\mathrm{dB}}$ with the frequency for the V-groove waveguide and for trenched groove at different widths; 120 nm, 300 nm, and 500 nm. It is revealed from this figure that the trenched groove mode radius is almost constant with the frequency variation. This is due to the fixed uniform width of the groove. However, the mode lateral radius $r_{3\mathrm{dB}}$ of the V-shaped groove is approximately constant at 271.1 nm in the frequency range from f = 200 THz to f = 350 THz. If the frequency is further increased to 550 THz, the lateral mode radius r_{3dB} of the V-shaped groove decreases below 50 nm. This is because the field starts to be confined inside the groove and the field moves toward the bottom region.

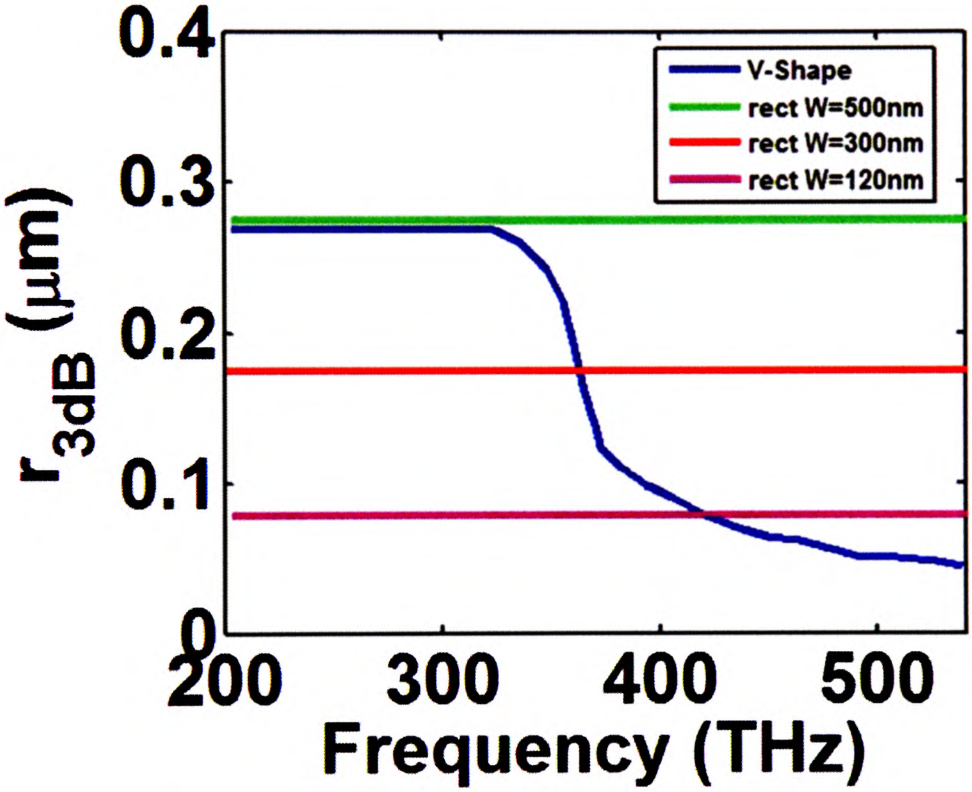

Figure 5.11 variation of the lateral mode radius r_{3dB} with the frequency for the V-groove waveguide and for the rectangular groove at different widths; 120 nm, 300 nm and 500 nm.

Fig. 5.12 shows the FOM variation with the frequency for the V-groove waveguide and for trenched groove at different widths; 120 nm, 300 nm and 500 nm. The narrow groove of width W=120 nm has very small r_{3dB} compared to the wide groove of width W=500 nm as shown in Fig. 5.11. Therefore, FOM for narrow groove is greater than that of the wide groove as shown in Fig. 5.12. However, the propagation length of the narrow groove is smaller than that of the wide groove. The $r_{3\mathrm{dB}}$ of the V-shaped groove in the frequency range from f=200 THz to f=350 THz is approximately constant and it is slightly smaller than that of the wide groove. However, the propagation length of the V groove has much smaller than that of the wide groove. Therefore, FOM of the V groove is smaller than that of the wide groove. Through the frequency range from 350 THz to 500 THz, $r_{3\mathrm{dB}}$ decreases sharply compared to the decreasing rate of the propagation length. However, the FOM of the V groove is bounded by the wide and narrow trenched groove curves as shown in Fig. 5.11. If the frequency is further increased, the FOM of the V-shaped groove is slightly better than those of the wide and narrow trenched groove.

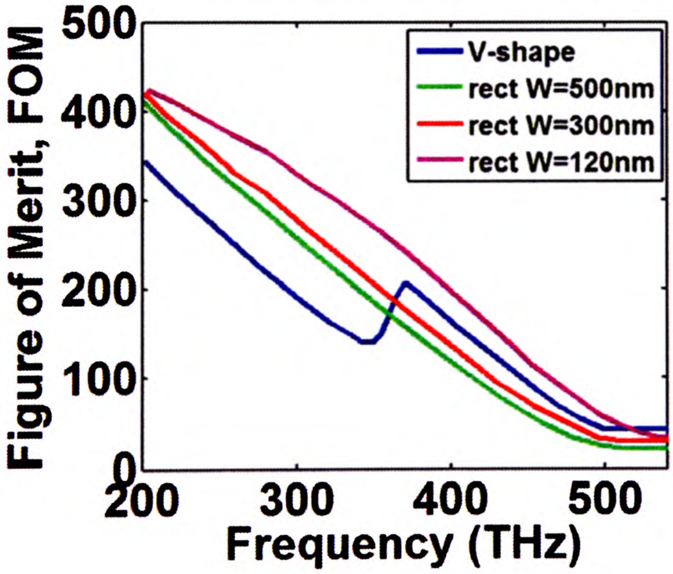

Figure 5.12 Variation of the figure of merit with the frequency for the V-groove waveguide and for the rectangular groove at different widths; 120 nm, 300 nm and 500 nm.

5.8.2 Modal Analysis for The Novel Three-Trenched CPP Waveguide

Next, the suggested three-trench CPP is studied and analysed. A schematic diagram of the reported three-trench waveguide is shown in Fig. 5.7 (a). The reported structure can be understood as three trenches with different widths W_1, W_2 and W_3 forming a simple stack in the direction oriented vertically to the metal surface. The depths of each groove are taken as d_1, d_2, and d_3. In this study, d_1 is fixed to 200 nm, while d_2 and d_3 are varied so that $d_2 + d_3$ = 1000 nm.

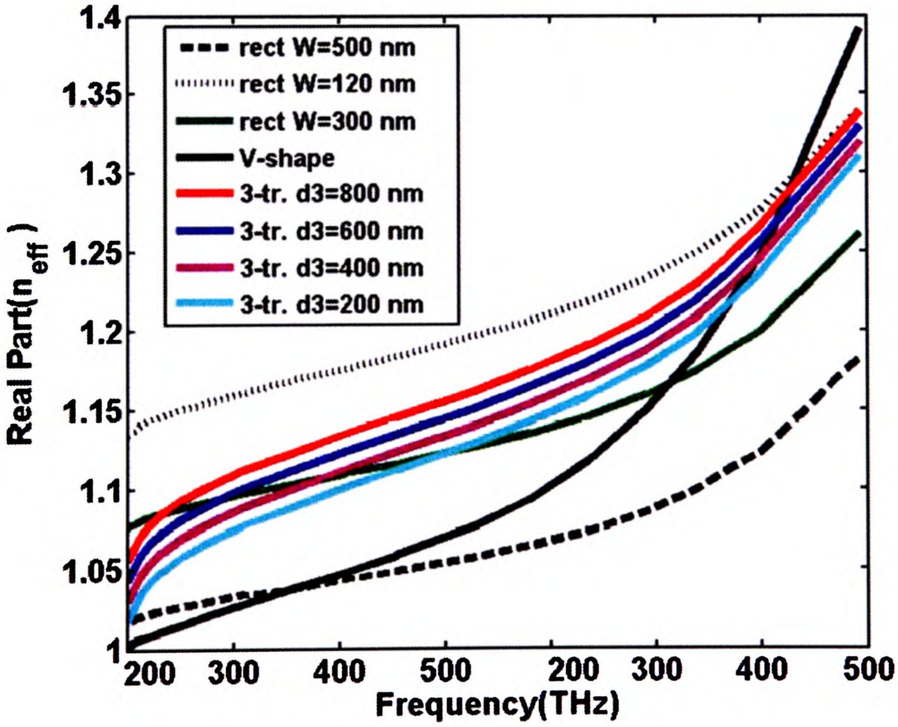

Figure 5.13 The frequency dependent n_{eff} for the suggested three trenched CPP waveguide, V-groove CPP, rectangular groove CPP

The frequency dependent n_{eff} and propagation length for the suggested three trenched CPP waveguide, V-groove CPPs, and rectangular groove CPP are shown in Fig.5.13 and Fig. 5.14, respectively. In this investigation, the widths of the 3-trenched groove W_1, W_2 and W_3 are fixed to 500 nm, 300 nm and 120 nm, respectively while the depth d_1 is fixed to 200 nm. The depth d_3 takes four different values 200 nm, 400 nm, 600 nm and 800 nm and the depth $d_2 = 1000 - d_3$. It is evident from Fig. 5.13 and Fig. 5.14 that most of n_{eff} and propagation lengths values for the three-trenched CPP waveguides are bounded between those values of the narrow and wide trenched groove waveguide. In addition, the suggested three-trenched CPP waveguides with shorter d_3, 200 nm, 400 nm and 600 nm show a great improvement in the propagation length compared to the V-groove waveguide. As the depth d_3 increases the propagation length decreases and it becomes smaller than that of the V-groove for d_3 = 800 nm.

Variation of the lateral mode radius $r_{3\mathrm{dB}}$ with frequency for the 3-trenched groove waveguides with different d_3 depths, 200 nm, 400 nm, 600 nm and 800 nm are shown in Fig. 5.15. In addition, $r_{3\mathrm{dB}}$ variation of the V-groove and trenched groove with different widths, 120 nm, 300 nm and 500 nm are also shown in Fig.5.15. It is evident from this figure that for each studied 3-trenched groove $r_{3\mathrm{dB}}$ remains almost constant at a certain level over a specific range of frequency. At a specific frequency the lateral mode radius of the three trenched groove starts to change in a step form. This occurs because the field starts to be more confined inside the narrow bottom groove by increasing the frequency. Therefore, the value of $r_{3\mathrm{dB}}$ can be controlled by changing the frequency of the incident wave. In addition, Fig.5.15 reveals that $r_{3\mathrm{dB}}$ values of the three trenched groove with different d_3 depths are bounded between those of the wide and narrow trenched groove.

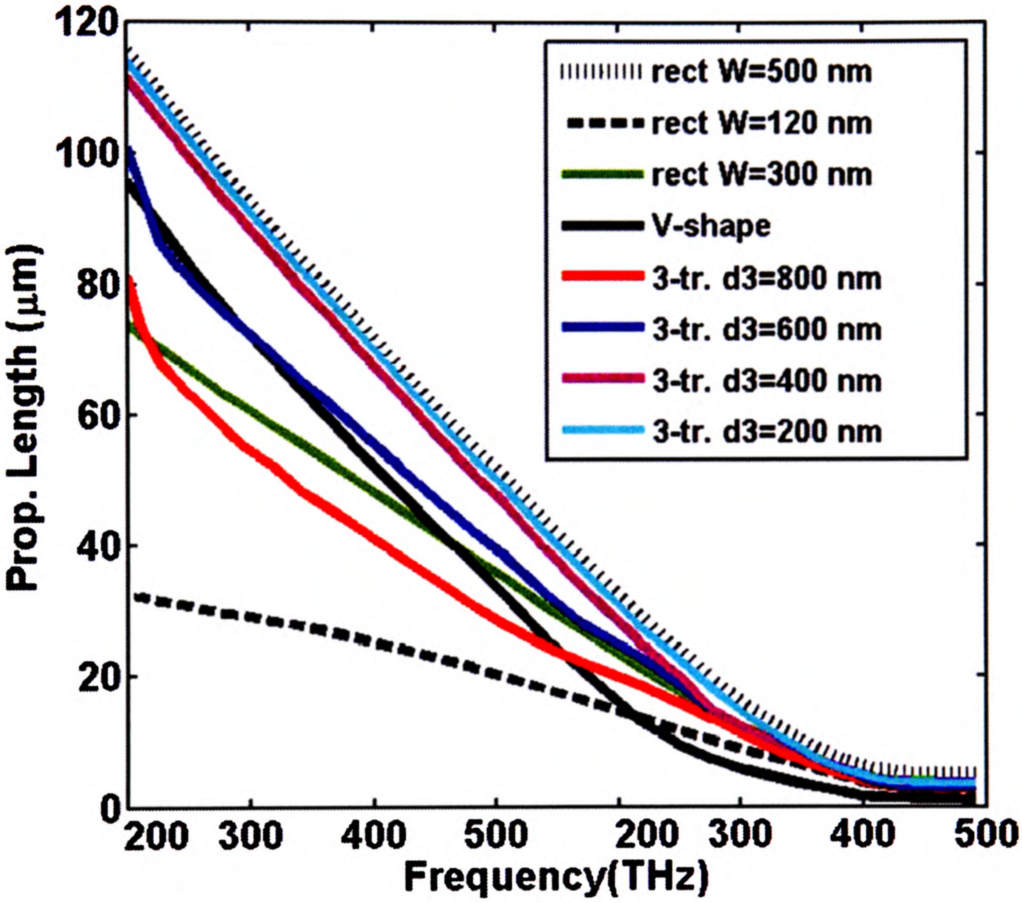

Figure 5.14 Variation of propagation length for the suggested three trenched CPP waveguide, V-groove CPP, rectangular groove CPP

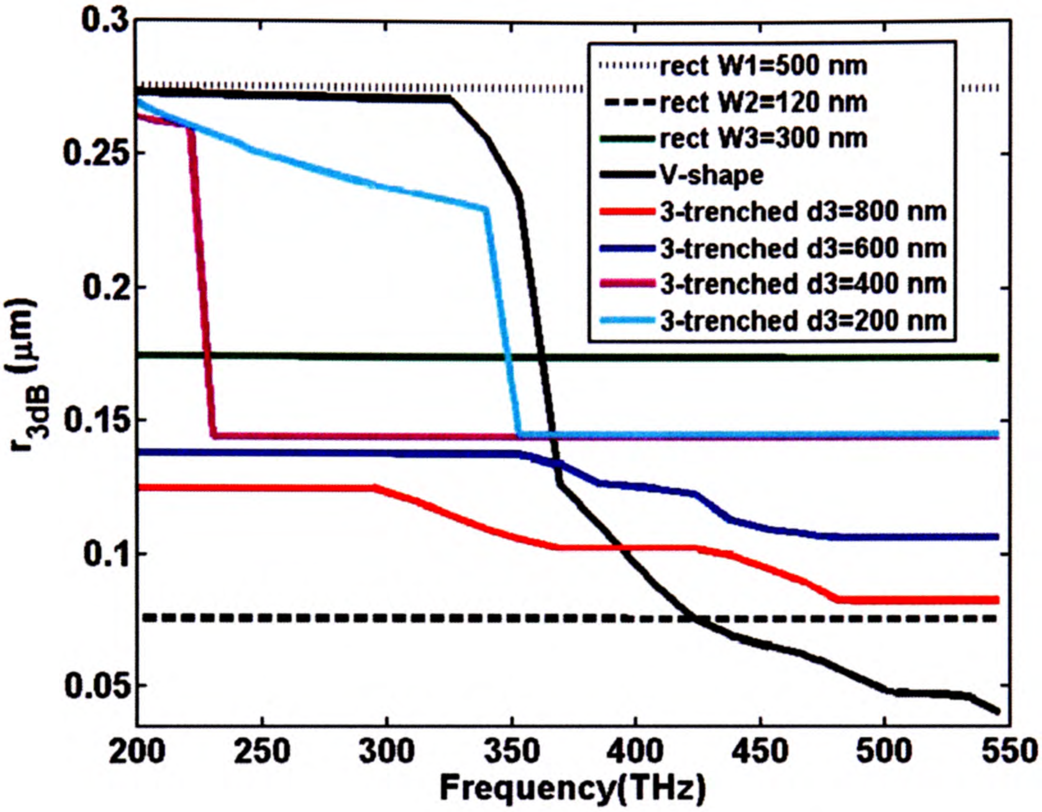

Figure 5.15 Variation of the frequency dependent lateral mode radius $r_{3\mathrm{dB}}$ for the trenched groove, V-groove and the three trenched groove waveguides with different d_3 depths,

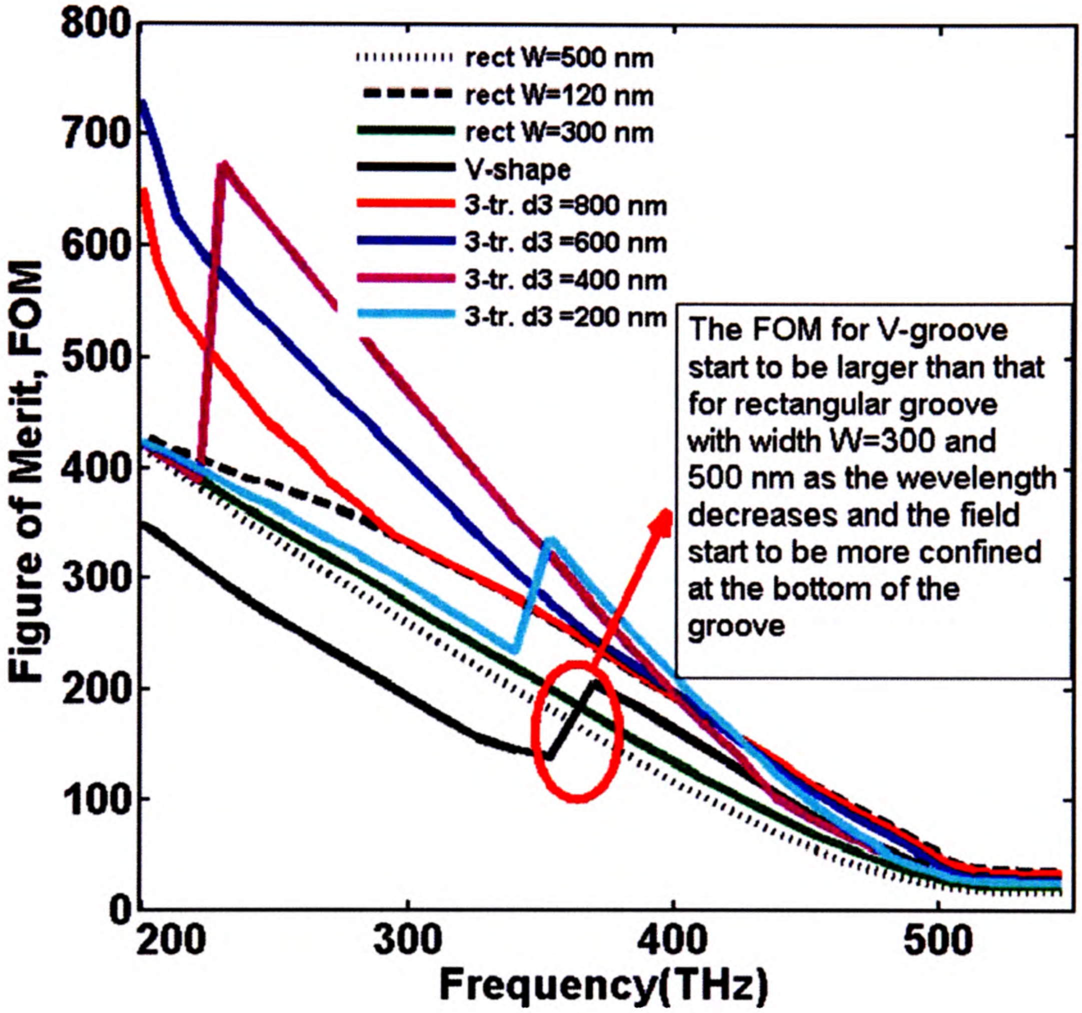

Figure 5.16 Variation of frequency dependent FOM for the trenched groove, V-groove, and three trenched groove waveguides with different d_3 depths.

The variation of FOM for the three trenched groove waveguides with the frequency at different d_3 depths is shown in Fig. 5.16. The frequency dependent FOM of the V-groove and rectangular groove are also shown in Fig. 5.16. It is revealed from this figure that the V-groove is the most efficient groove with the highest FOM for frequency greater than 500 THz. However, in the frequency range from 350 to 400 THz the propagation length for the 3-tenched groove with d_3 = 200 nm is greater than that of all other grooves. However, $r_{3\text{dB}}$ is small and near to that of W=300 nm as it is the longest depth d_2 = 800 nm. Therefore, FOM increases by decreasing d_3. When the frequency decreases below f = 350 THz, $r_{3\text{dB}}$ for the three trenched groove with a short d_3 = 200 nm starts to increase causing the FOM to drop down suddenly. The same effect occurs for the three trenched groove with d_3=400 THz which has a sudden drop at f = 225 THz. Therefore, a great improvement in the FOM of the suggested groove has been accomplished

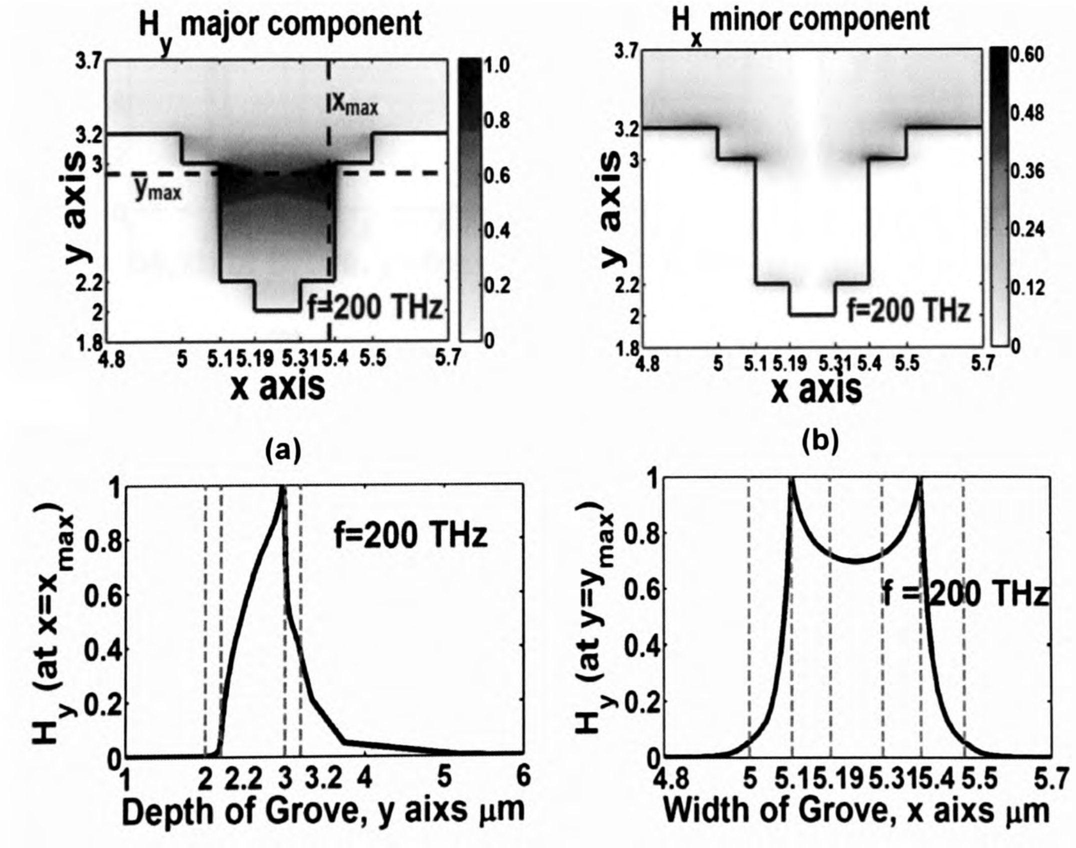

(a) (b)

(c) (d)

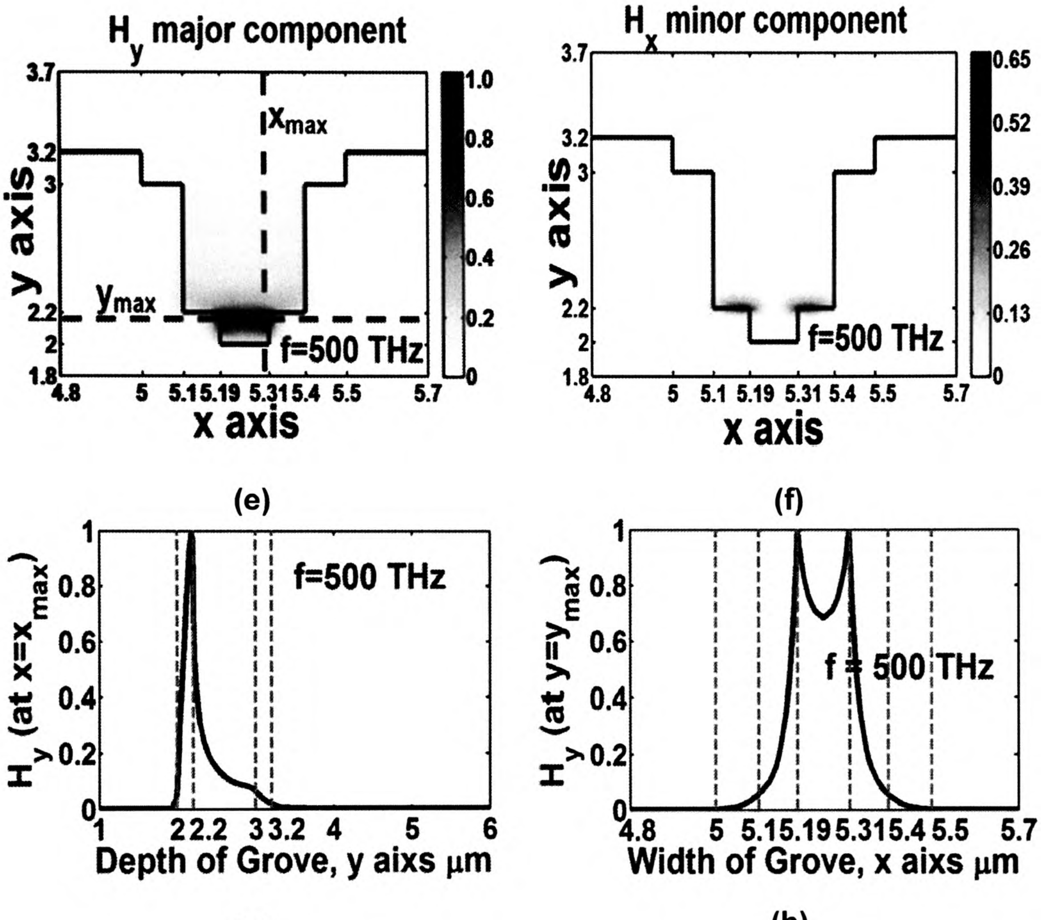

(e) (f)

(g) (h)

Figure 5.17 (a), (b), (e) and (f) the field profiles of the fundamental TE mode of suggested three-trenched CPP, at two different frequencies, 200 THz, and 500 THz. Figure 10 (c), (d), (g) and (h) shows the variation of the major field component H_y for the TE fundamental mode at the maximum plane in x and y directions

Fig. 5.17 (a), (b), (e) and (f) show the field profiles of the fundamental TE mode of the suggested three-trenched CPP, at two different frequencies, 200 THz and 500 THz. As shown from these figures, the field leaks to the widest channel groove at low frequency 200 THz while the field is confined to the narrow groove at high frequency of 500 THz. Fig. 5.17 (c), (d), (g) and (h) shows the variation of the major field component Hy for the TE fundamental mode at the maximum plane in x and y directions. In order to get the maximum plane, the point (x_{max}, y_{max}) at which H_y maximum occurs is first obtained. Then the variation of H_y through the planes $x = x_{max}$ and $y = y_{max}$ is plotted. It should be noted that there is two maximum points (x_{max1}, y_{max}) and (x_{max2}, y_{max}) because the field is symmetric around the plane x=5.25 µm. The second maximum plane in Fig.5.17 (c) and (g) is selected at $x= x_{max2}$ where x_{max2}=5.3952 and 5.3081 for Fig. 5.17 (c) and (g) respectively.

The FOM is greatly affected by the variation of widths of the three-trenched groove. The numerical results reveal that the narrow groove W_3 has a great impact on the FOM of the suggested structure. Therefore, a comprehensive study has been done in order to investigate the proper width for W_3 which maximizes the FOM. First, the effect of the width W_3 on n_{eff} and propagation length is investigated. Fig. 5.18 (a) and (b) show the variation of the propagation length with W_3 of the reported three trenched structure at two different frequencies 200 and 500 THz with different d_3, 200 nm, 400 nm, 600 nm and 800 nm. However, the other parameters are fixed to W_1=500 nm, W_2 = 300 nm, d_1 =200 nm. It should be noted that the groove width d_3 of 200 nm is very short compared to the wavelength of the incident wave. Therefore, the propagation length of the three-trenched groove with d_3=200 nm at f=200 THz is almost constant as revealed from Fig. 5.18 (a). However, the propagation lengths at d_3 = 400 nm, 600 nm and 800 nm, increase significantly by increasing the width W_3 from 90 to 120 nm. If the W_3 is further increased from 120 nm to 150 nm, the propagation lengths slightly increase. This is because the smallest groove becomes wide compared to the wavelength. At f=500 THz, the propagation lengths for d_3=200 nm and d_3=400 nm are approximately constant. However, the propagation lengths for the wide three trenched structures of d_3=600 nm and d_3=800 nm increase by increasing W_3.

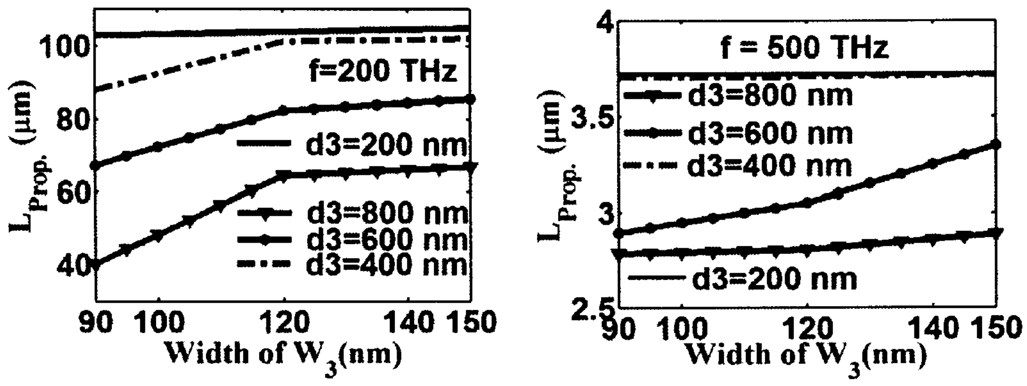

(a) (b)

Figure 5.18 Variation of propagation length with W_3 of the suggested three trenched structure at different d_3 at two different frequencies (a) f=200 and (b) f=500 THz

Fig. 5.19 (a) and (b) show the variation of the r_{3dB} of the suggested three trenched structure with W_3 at two different frequencies 200 and 500 THz at different d_3, 200 nm, 400 nm, 600 nm and 800 nm. It is evident from Fig. 5.19 (a) that the lateral mode radius r_{3dB} of the three trenched structure with d_3= 400 nm, 600 nm and 800 nm at low frequency of 200 THz increases with increasing W_3. However, the trench with d_3= 200 nm shows a different behaviour. At d_3= 200 nm, the depth is short (shallow). Therefore, as the width W_3 decreases below a certain width of 120 nm at f = 200 THz, the field cannot confined itself inside the groove. In addition the field starts to go out of the bottom part of the groove. This causes the lateral mode radius r_{3dB} to increase as we are so close to the cut-off of the single mode. It should be noted that the width of the rectangular groove cannot be decreased forever as at a certain width the channel cannot support single mode anymore. At high frequency f = 500 THz, when W_3 is increased from 90 to 120 nm the lateral mode radius slightly increases due to the well confinement of most of the field inside the narrow groove as shown in Fig 5.19(b). When W_3 is further increased, W_3 starts to be close to W_2 and part of the field starts to go up towards W_2. Therefore, when W_3 is increased from 120 to 150 nm r_{3dB} increases rapidly. Fig. 5.20 (a) and (b) show the variation of FOM with the width W_3. From these figures it is found that the optimum W_3 width of the suggested structure with maximum FOM in the studied frequency range is equal to 120 nm.

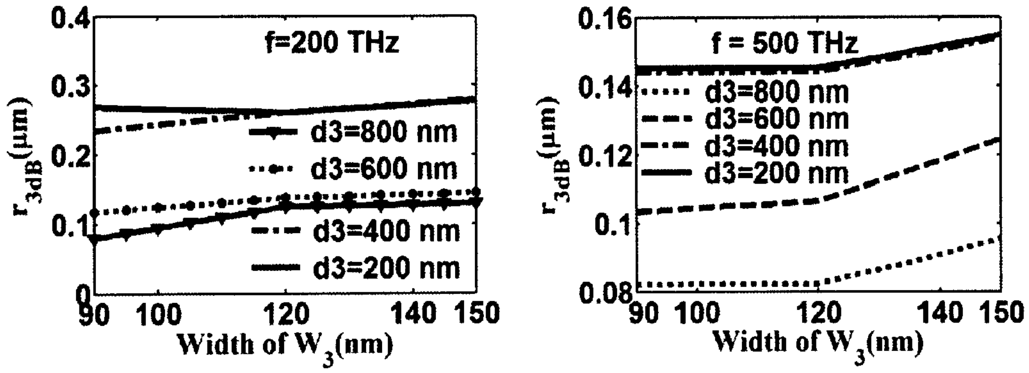

(a) (b)

Figure 5.19 Variation of the lateral mode radius r_{3dB} of the suggested three trenched structure with W_3 at different d_3 at two different frequencies (a) f=200 and (b) f=500 THz.

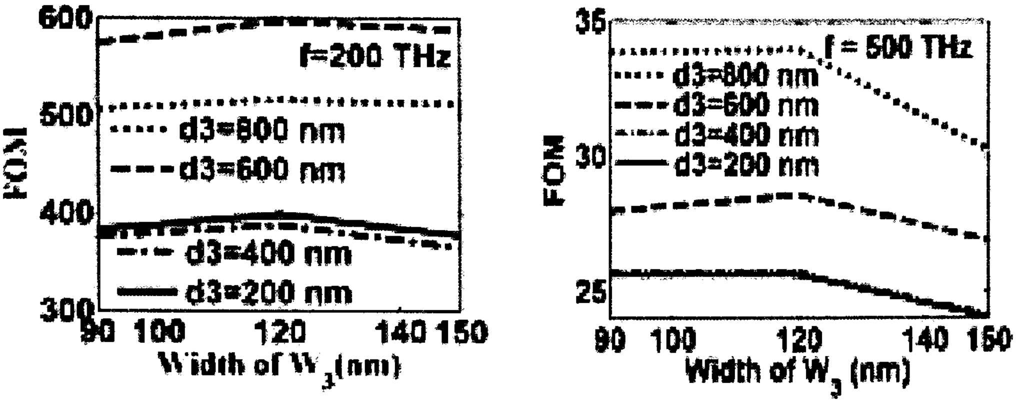

(a) (b)

Figure 5.20 Variation of the FOM with the width W_3 at different d_3 at two different frequencies (a) f=200 and (b) f=500 THz at different d_3.

5.9 Summary

The channel plasmonic waveguides (metallic groove or wedges) have been studied. Through this study V-groove has the best confinement; while the rectangular groove with same width and depth has a better propagation length (i.e. less metal damping losses). As there is always a trade-off between the confinement of the mode inside the groove and the propagation length, the figure of merit FOM has been used to decide which groove has the best performance at a certain range of frequency. A novel three trenched plasmonic groove has been presented. Such groove has a good confinement as well as V-groove, however it has a better propagation length. So, this structure can provide high FOM compared to V-groove or rectangular groove.

Chapter 6

Hybrid Long-Range Plasmonic Waveguide

6.1 Introduction

In SPP, electromagnetic waves can be confined in a small cross-section located perpendicular to their direction of propagation while most of the power is confined to the interface. One of the amazing applications of plasmonics is the implementation of nano-photonic integrated circuits on conventional electronic devices. Therefore, several nano-plasmonic waveguides based on metallic channel, wedge, and gap structures have been analysed [93-98]. However, the loss due to internal damping of radiation in metal limits the progress of practical application. Many SPP waveguide structures have been introduced with highly confined electromagnetic waves and a moderate loss [97, 98]. In addition, Long-range SPP (LRSPP) based on thin metal films or stripes have been investigated by Berini [38]

Owing to the SPP dispersion, the SPP is a wave accumulating energy from the incident light and providing field enhancement near the metal interface. Therefore, the SPP wave can be localised beyond the diffraction limit and opens huge opportunity to subwavelength optics [99]. As a result of ohmic losses in metal, SPPs have a finite propagation distance that depends on the geometry of the supporting structure [100].

Metal-dielectric-metal (MDM) and dielectric-metal dielectric (DMD) structures have two types of super SPP modes of even and odd symmetries. These two super-modes show opposite characteristics. The odd super-mode called short range SPP mode (SRSPP) shows good confinement as the metal layer gets thinner. However confinement of the even super-mode, called long range (LRSPP), gets looser for the thinner metal layer and hence, its propagation length increases [99-103]. The LRSPPs can propagate for several millimetres [101] and are very sensitive to changes of the dielectric environment. Therefore, the LRSPP has a lot of applications in biosensor optical devices [102].

Since those planar SPP-supporting structures composed of dielectric-metal, MDM, and DMD provide field confinement only in one dimension, an additional means to confine light in the direction parallel to the metal surface is needed to implement two-dimensional confinement. Various SPP-based waveguide structures have been proposed with different additional confinement means. In waveguide structures such as metal channel waveguides [98], metal hetero waveguides [99], and MDM waveguides with high-index cores [104], the additional confinement means are based on index-guiding, that is, light is confined in a high-effective index region. There have been proposed other approaches such as thin dielectric film loaded-SPP waveguides [97] and MDM waveguides with low-index cores [105], in which light is confined in a low-effective-index region. In these waveguides, the additional confinement relies on the difference of the dispersion characteristics of SPP modes between the low- and the high-index regions. The high-index regions are designed not to have propagation modes so that the addition confinement is quite strong. In some other proposed waveguide structures, the additional confinement is achieved by modifying metal geometry itself, which include metal grooves [101].

Recently, a type of hybrid plasmonic waveguide, with high-index-contrast dielectric material and plasmonic waveguide has attracted intensive research interest because of its ability to balance the propagation distance and modal size. This is due to the coupling between the dielectric waveguide and plasmonic modes [106-111]. The hybrid plasmonic waveguide with a metal cap has been presented in [106], to realise a low-voltage compact optical modulator when the nano-layer material between the Si layer and the metal layer has high electro-optical coefficient. However, silicon-based 3-D hybrid long-range plasmonic waveguide that not only supports long-range propagation, but also has a compact modal size is introduced by Chen et al. [111].

In this work, comprehensive study has been done to investigate the dispersion characteristics and bending analysis of a novel design of hybrid long-range plasmonic waveguide with Si cap. The suggested design is based on a metal strip embedded in a dielectric rib. In addition, a very thin high index dielectric cap is placed on the top of the dielectric rib. The high-index Si cap decreases the propagation loss for the hybrid plasmonic waveguide. Moreover, the coupling between the straight dielectric waveguide and straight hybrid plasmonic waveguide is studied. Finally, the coupling between straight hybrid plasmonic waveguide and bent hybrid plasmonic waveguide is calculated. The suggested structure can be used to construct various functional devices in nanophotonic integrated circuits.

In general, SPP-based waveguides show a trade-off between the field confinement and the propagation loss: a waveguide has a good confinement, has a high propagation loss due to Ohmic loss of metal. In terms of the propagation loss, waveguides based on the LR-SPP such as the metal-stripe waveguides are preferred.

6.2 Numerical Model

Modal solutions are very useful for the characterisation and design of plasmonic waveguides. To calculate accurately vector modal field profiles of plasmonic waveguide, a full vectorial modal solution approach is necessary. Many modal solution techniques have been proposed in the past few years such as the finite element method (FEM) [46], finite element based imaginary distance beam propagation method (IDBPM) [49], finite difference method (FDM) [45], and multipole method [47]. In this study, the full vectorial finite difference method (FVFDM) [45] with perfect matched layer (PML) boundary conditions [63] is used to calculate the full vectorial quasi transverse electric (TE) and quasi transverse magnetic (TM) modes for the suggested waveguide. In order to get accurate results a non-uniform meshing is used, so that a high condensed meshing is applied in the expected field regions and a low condensed meshing is applied in the empty field regions.

The simulation is performed by the FVFDM [45] with non-uniform meshing capabilities. The analysed parameters are effective index n_{eff}, propagation loss (insertion loss), optimal bending radius r and coupling coefficient. The reported design shows a very good confinement behaviour and a great reduction for the propagation loss.

6.3 Novel Hybrid Long-Range Plasmonic Waveguide

Fig. 6.1 (a) and (b) illustrate the suggested novel hybrid long-range plasmonic waveguide. In this study, the wave is coupled from a dielectric waveguide (Benzocyclobutene (BCB) on SiO_2 with Si cap) over a straight hybrid plasmonic waveguide to a uniformly bent hybrid plasmonic waveguide.

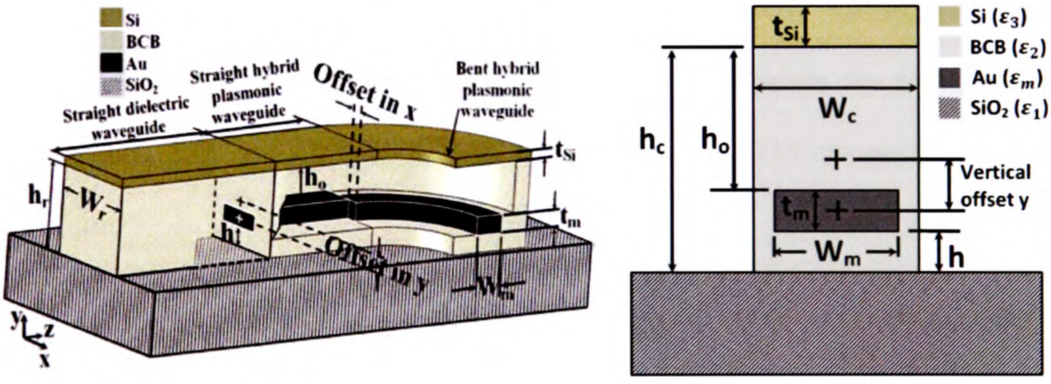

(a)

(b)

Figure 6.1 (a) Illustration of the considered dielectric and hybrid plasmonic waveguide structure. The wave couples from a dielectric waveguide (BCB on SiO_2 with Si cap) over a straight hybrid plasmonic waveguide to a uniformly bent hybrid plasmonic waveguide. Fig. 1 (b) Schematic diagram of hybrid long range plasmonic waveguide.

The hybrid plasmonic waveguide consists of a gold strip of thickness $t_m = 20$ nm and width W_m embedded in BCB rib of fixed width $W_r = 6.5$ μm and height h_r=1.6 μm. In addition, high-index Si cap of thickness t_{si} covers the BCB rib to decrease the propagation loss. In order to obtain the maximum coupling between the straight dielectric waveguide and the straight hybrid plasmonic waveguide, the metal strip centre is shifted from the centre of the BCB rib (in y direction). Moreover, to achieve maximum coupling between the straight hybrid plasmonic waveguide and the bent hybrid plasmonic waveguide only a shift (in x-direction) is needed. Furthermore, the metal strip height from the SiO_2 substrate is taken as h while the distance between the Si cap and metal strip is defined as h_o.

In this paper, all simulation results are obtained at the telecommunication wavelength λ=1.55μm where the gold metal has a permittivity ε_m= -131.95+j12.65 which is calculated using extended Drude model [112]. However, the permittivity of BCB, Si and SiO_2 are taken as 2.356225, 12.0409 and 2.0736 respectively [113] at λ=1.55μm.

In order to have fixed computational domain, all sides are truncated with the PML which plays an essential role in the calculation. The PML is used to prevent any interference resulting from the radiating wave reflections at computational boundaries.

The top cap thickness must be chosen carefully due to its effect on the coupling characteristic and propagation loss of the reported design. If the thickness of the cap layer is increased above a certain value it starts to work as a second core due to its high refractive index. The thickness of the cap layer depends on the cap refractive index and the rib geometrical parameter.

Fig. 6.2 shows the effect of the cap thickness t_{si} on the effective index and propagation loss for the straight hybrid plasmonic waveguide with metal strip of width W_m= 3μm and metal strip height h = $(h_r-t_m)/2$ = 0.79μm. It is revealed from this figure that as the thickness t_{si} increases the effective index increases while the propagation loss decreases. This is due to the field movement towards the high index cap region away from the metal strip which decreases metal loss.

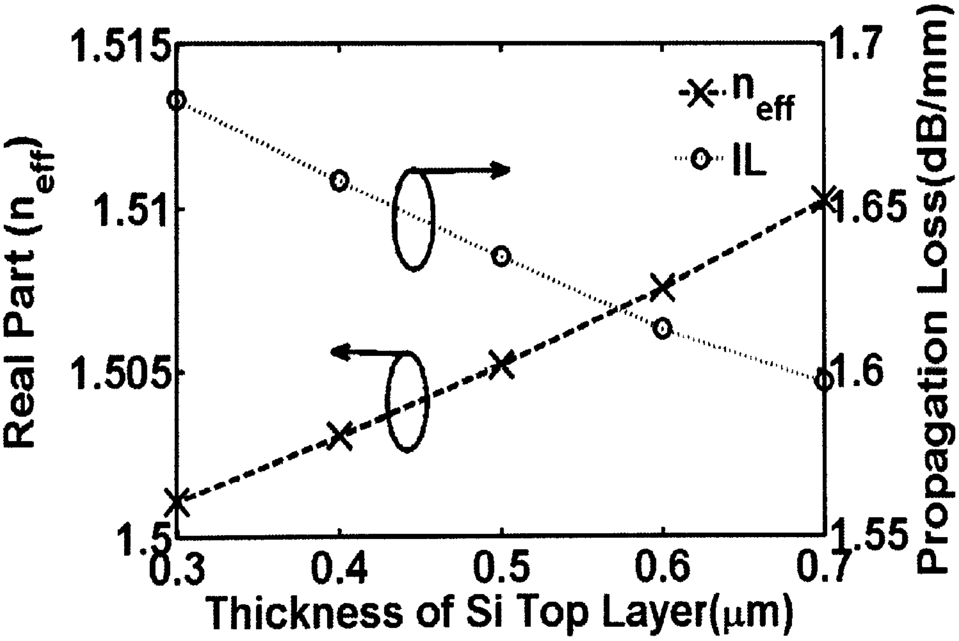

Figure 6.2 Variation of the real part of n_{eff} and propagation loss with the thickness t_{si} of Si top layer

It is evident from Fig. 6.3 (a) and Fig. 6.3 (b) that at t_{si} = 0.7 μm the mode is not pure SPP mode. The maximum value of the minor field component H_y will be in the top layer away from the metal strip as shown in Fig. 6.3 (b) and (f). Therefore, part of the field propagates as a slab mode. However, at t_{si} = 0.3 μm as shown in Fig. 6.3 (g) and Fig. 6.3 (h), both minor and major field components propagate at metal-BCB interface. Therefore, in order to have pure plasmonic mode and to prevent this effect t_{si} is fixed to 0.3 μm in the subsequent simulation.

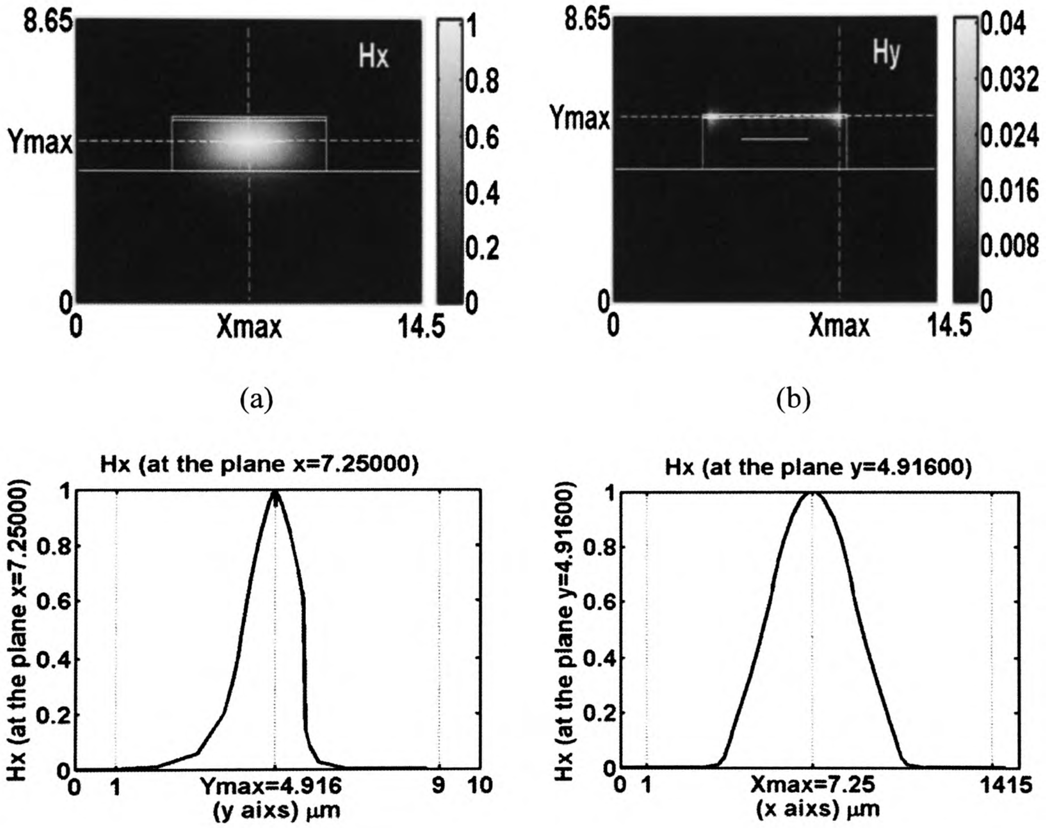

(a) (b)

(c) (d)

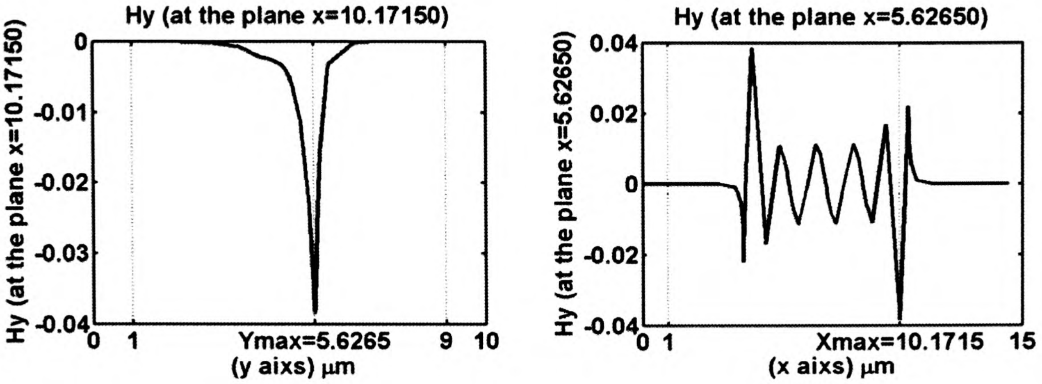
Hy (at the plane x=10.17150)
Hy (at the plane x=10.17150)
0
-0.01
-0.02
-0.03
-0.04
0 1 Ymax=5.6265 9 10
(y aixs) μm
Hy (at the plane x=5.62650)
Hy (at the plane x=5.62650)
0.04
0.02
0
-0.02
-0.04
0 1 Xmax=10.1715 15
(x aixs) μm

(e) (f)

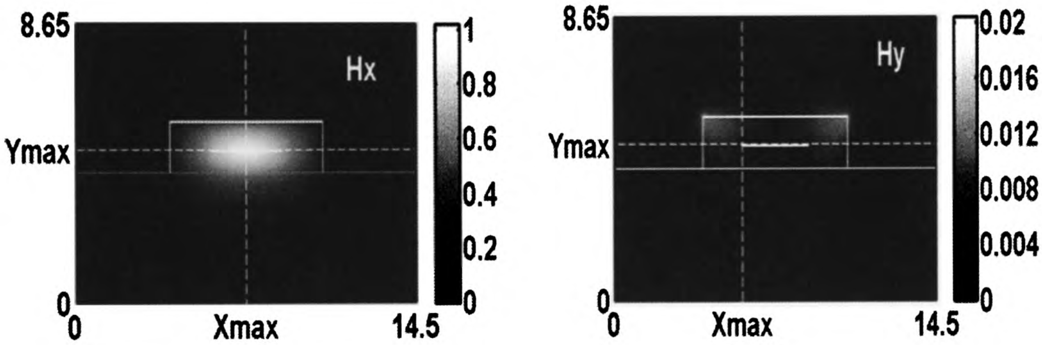
8.65
Ymax
0
0
Xmax
14.5
Hx
1
0.8
0.6
0.4
0.2
0
8.65
Ymax
0
0
Xmax
14.5
Hy
0.02
0.016
0.012
0.008
0.004
0

(g) (h)

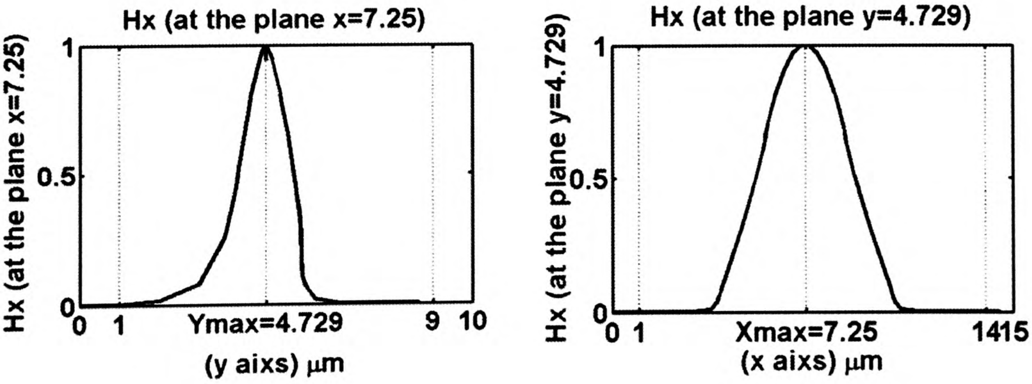
Hx (at the plane x=7.25)
Hx (at the plane x=7.25)
1
0.5
0
0 1 Ymax=4.729 9 10
(y aixs) μm
Hx (at the plane y=4.729)
Hx (at the plane y=4.729)
1
0.5
0
0 1 Xmax=7.25 1415
(x aixs) μm

(i) (j)

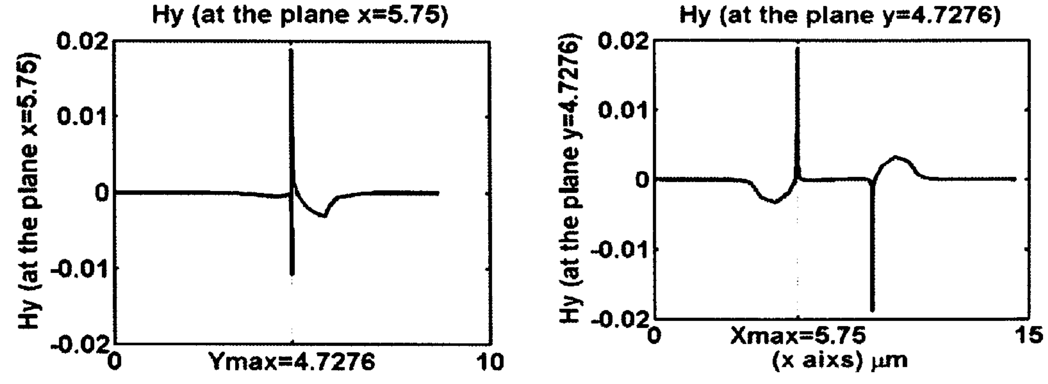

(k) (l)

Figure 6.3 (a), (b), (c), (d), (e) and (f) field profile for the magnetic field component H_x and H_y at t_{si} = 0.7 μm, W_m =3 μm and h=0.684 μm while Fig.3 (g), (h), (i), (j), (k) and (l) show field profile at t_{si} =0.3 μm, W_m = 3 μm and h = 0.724 μm

The height h of the metal strip above the SiO_2 substrate affects the value of effective index and the propagation loss. The field on top and bottom sides of the metal faces of different materials (Si on top and SiO_2 on bottom) and at a certain height $h=h_{opt}$ a minimal loss occurs. As the metal strip moves down and up the field starts to be more or less symmetric. It should be noted that symmetric field distribution of the asymmetric multilayer structure decreases the propagation losses [102].

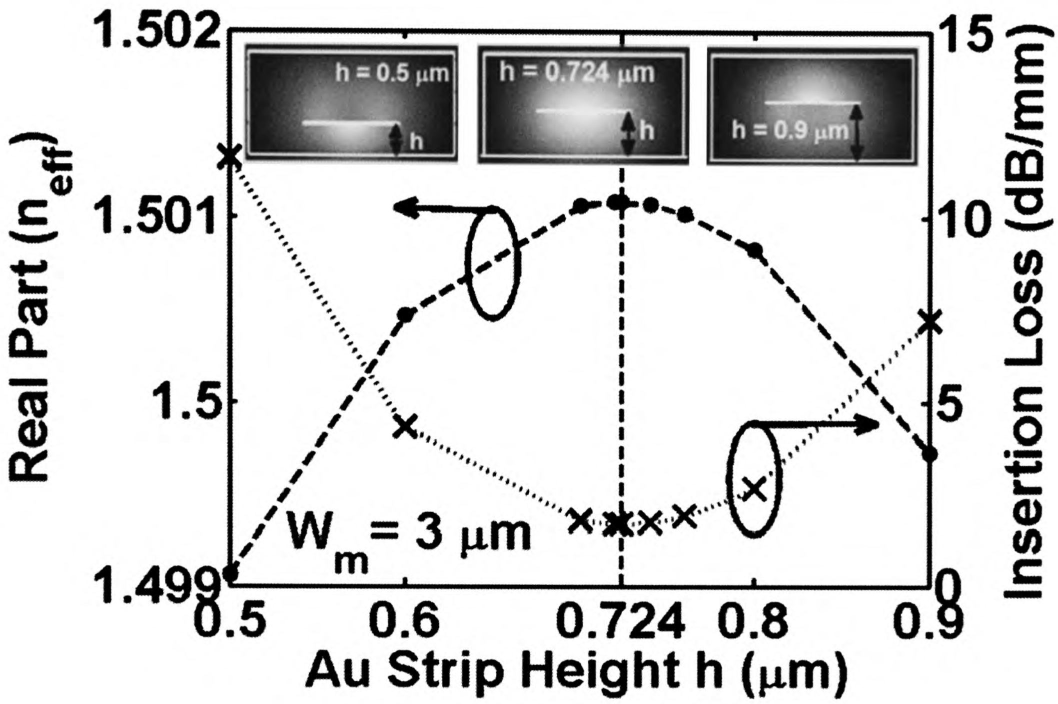

Figure 6.4 Variation of the real part of n_{eff} and propagation loss with the metal strip height at W_m=3 for straight hybrid plasmonic waveguide.

In Fig. 6.4 the effect of changing the metal strip height h of width W_m=3 μm on the effective index n_{eff} and propagation loss for only the straight hybrid long-range plasmonic waveguide structure (no coupling and no bent is considered in this case) has been studied. For h < (h_{opt} =0.724 μm) as h decreases the field starts to be more confined between metal strip and substrate. So the effective index decreases and propagation loss increases. For h > h_{opt} as h increases the field starts to be more confined at top region between cap and metal and also effective index decreases and propagation loss increases. At a certain optimal height h_{opt} the field is confined symmetrically around the strip which minimises propagation loss and maximizes the effective index.

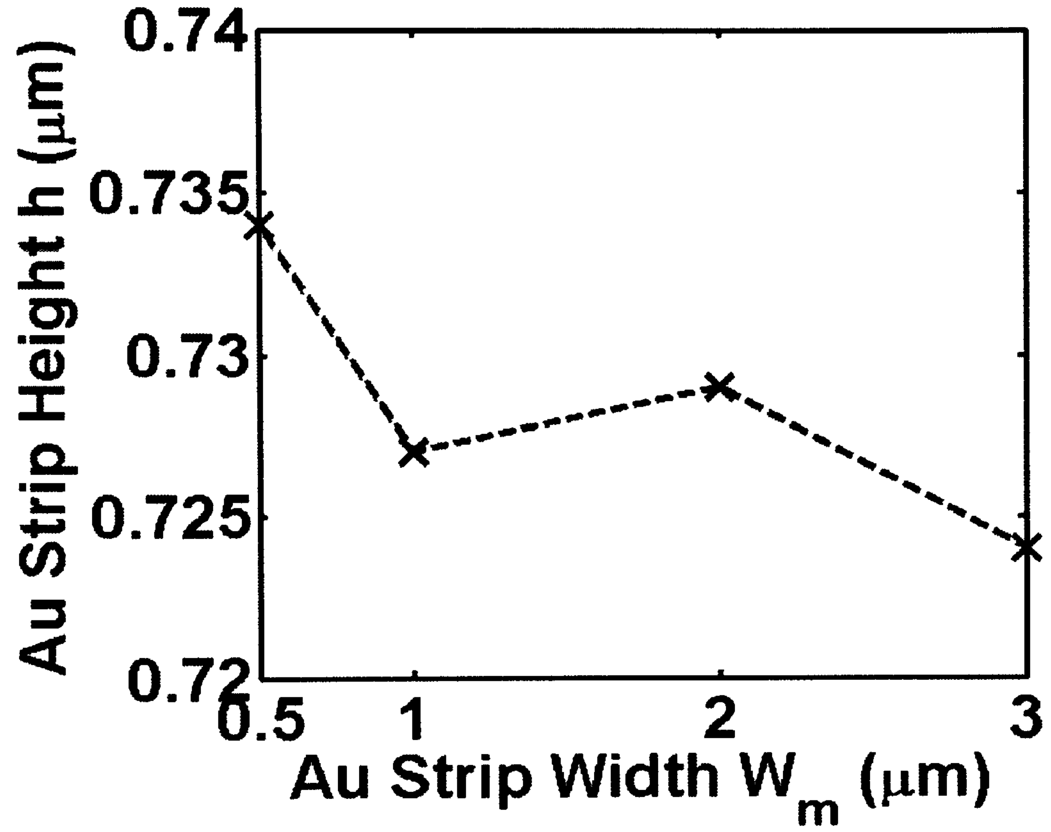

Figure 6.5 Variation of the optimal metal strip height with metal width W_m

Fig. 6.5 shows variation of the optimal metal strip height with the metal width W_m. It may be clear from this figure that this height is slightly affected by the metal width by few nanometres. As the width W_m changes from 0.5 to 3 μm, the optimal height h_{opt} changes from 72.4 nm to 73.4 nm, respectively.

6.4 Bending Analysis

Waveguide bend analysis is essential for the design of integrated plasmonic circuits. As mentioned by Berini *et al.* [114], an optimal radius r_{opt} for a given plasmonic waveguide exists, where the radiation and propagation losses are minimised.

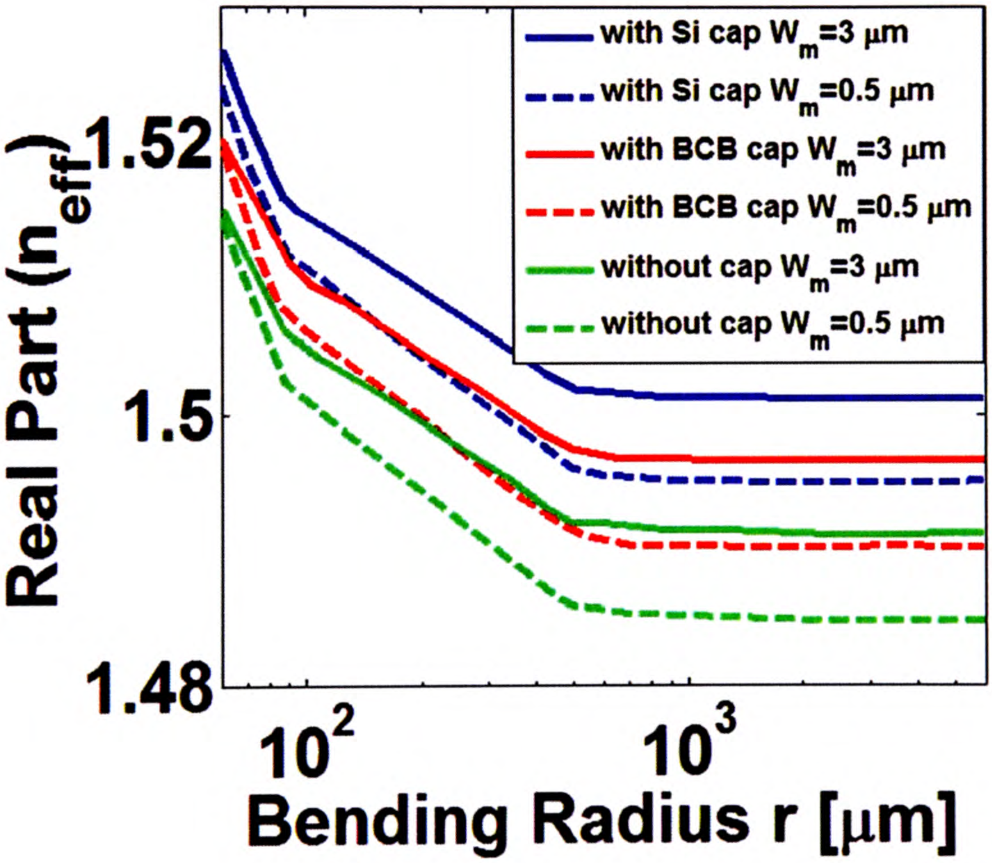

Figure 6.6 Variation of real part (n_{eff}) with the bending radius r

Fig. 6.6 and 6.7 illustrate the variation of the effective index n_{eff} and propagation loss L_{prop} with the bending radius, respectively with Si cap, with BCB cap and without cap at two different widths W_m, 0.5 μm and 3.0 μm.

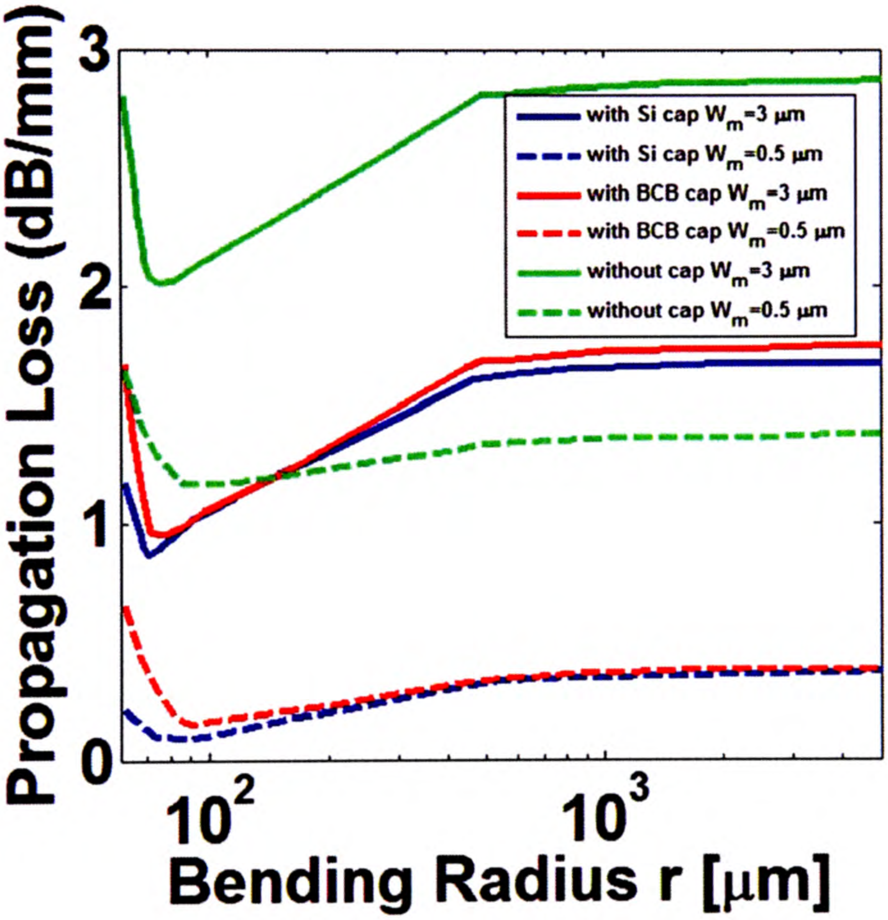

Figure 6.7 Variation of propagation loss (L_{prop}) with the bending radius r

It is evident from Fig. 6.7 that the high index Si cap decreases the propagation loss, at r > 1000 μm, by 11-20% compared to without cap case at W_m = 3 μm. However, the Si cap is very useful when metal width is small and small bending radius is considered, as at r<100 μm and W_m=0.5 μm, the propagation loss decreases by 41-86% compared to without cap case. In addition, the propagation loss is decreased by increasing the refractive index of the cap. Therefore, the propagation loss without cap is higher than that with BCB cap and Si cap. It is also revealed from Fig. 6.6 and Fig.6.7 that the effective index of the suggested structure with Si cap is greater than that with BCB cap. Moreover, the propagation loss and optimum bending radius r_{opt} with Si cap with minimum propagation length, is smaller than that with BCB cap. At W_m = 3 μm, L_{prop} = 0.91 dB/mm and r_{opt} = 90 μm are obtained with BCB cap while L_{prop} = 0.77 dB/mm and, r_{opt} = 80 μm are achieved with Si cap. The numerical results also reveal that the effective index and propagation loss at W_m=3.0 μm are greater than those of W_m= 0.5 μm as shown in Fig 6.6 and Fig.6.7. It is also shown from Fig. 6.6 that the effective index n_{eff} decreases by increasing the bending radius from r =70 μm to 1000 μm. If the bending radius is further increased, n_{eff} starts to be constant.

Fig. 6.8, Fig. 6.9 and Fig. 6.10 shows the effect of varying the width of metal strip Wm on the refractive index, propagation loss and bending loss for the bent hybrid plasmonic waveguide (when the Si cap is considered) respectively. The results has been obtained at four different widths Wm = 0.5 μm, 1 μm, 2 μm and 3 μm.

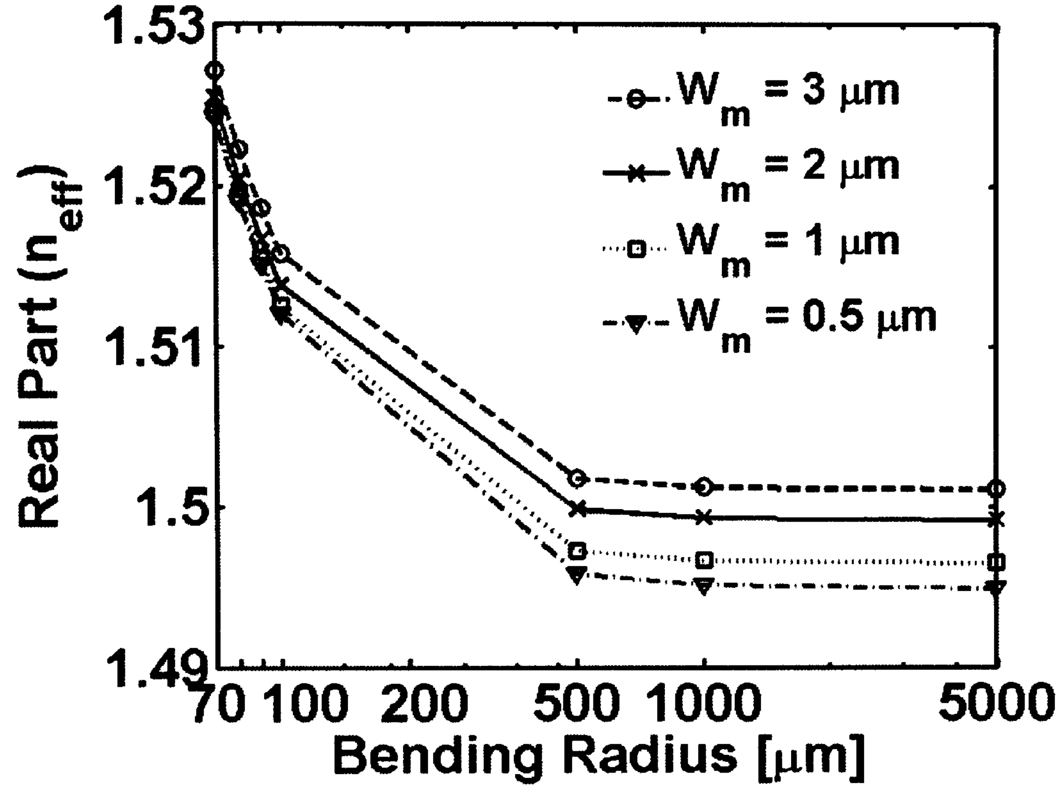

Figure 6.8 Variation of real part (n_{eff}) with the bending radius r

It may be clear from Fig. 6.8 that the effective index at different W_m decreases by increasing the bending radius from 70 μm to 1000 μm. If the bending radius is further increased the effective index will be approximately invariant.

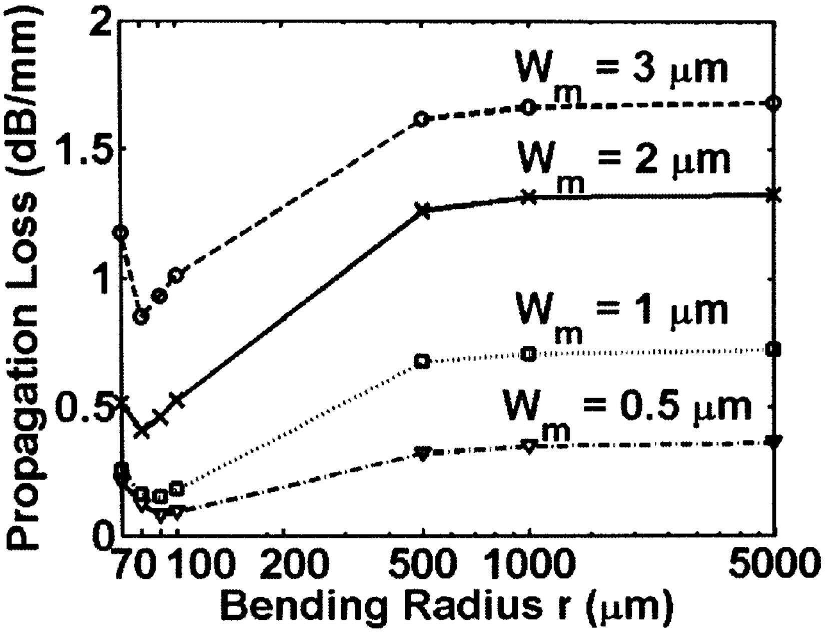

Figure 6.9 Variation of propagation loss (L_{prop}) with the bending radius r

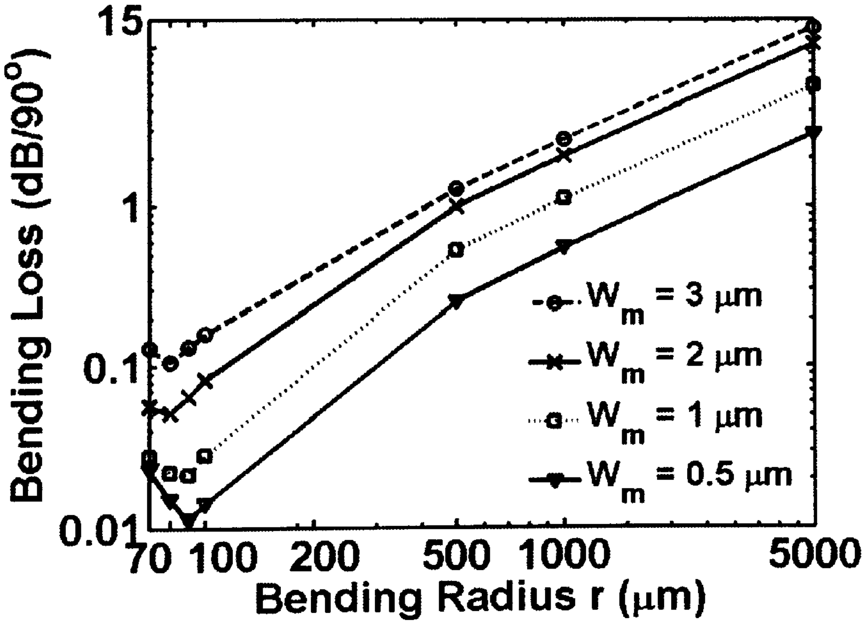

Figure 6.10 Variation of Bending loss with the bending radius r

6.5 Coupling Characteristic

Now consider the coupling between straight dielectric waveguide and straight hybrid waveguide is considered. The coupling coefficient can be calculated through the following formula [115]

$$C = \frac{\iint_{\Omega} E_{y1} E_{y2}^{*} d\Omega}{\sqrt{\iint_{\Omega} E_{y1} E_{y1}^{*} d\Omega \iint_{\Omega} E_{y2} E_{y2}^{*} d\Omega}} \tag{6.1}$$

where E_{y1}, E_{y2} are the electric field distribution for the two waveguide.

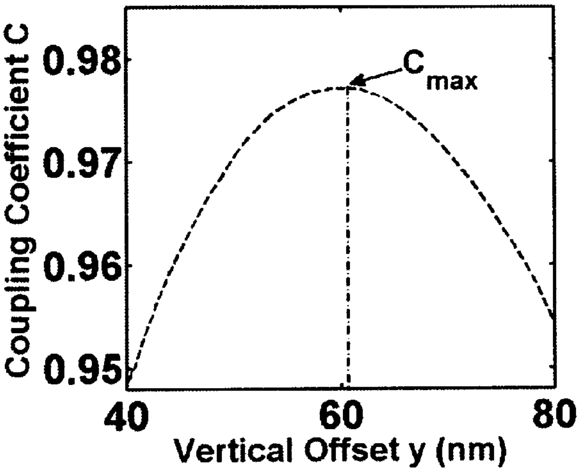

Figure 6.11 Variation of Coupling Coefficient C with the Vertical offset y (nm)

It should be noted that as both waveguides are straight waveguide there is no need to realign both waveguides horizontally in x-direction because the field centres in both waveguides are in the same x-plan. However, it was previously mentioned that in hybrid waveguide the propagation loss decreases when the field is symmetric around the metal strip. This occurs at a certain optimum metal strip height h_{opt}. Therefore, at a certain vertical offset y_{opt} the coupling coefficient between these two waveguides is maximised as shown in Fig. 6.11. Fig. 6.11 shows the variation of the coupling coefficient C with the vertical offset y. The metal width W_m=3 μm and the metal strip height $h=h_{opt}$

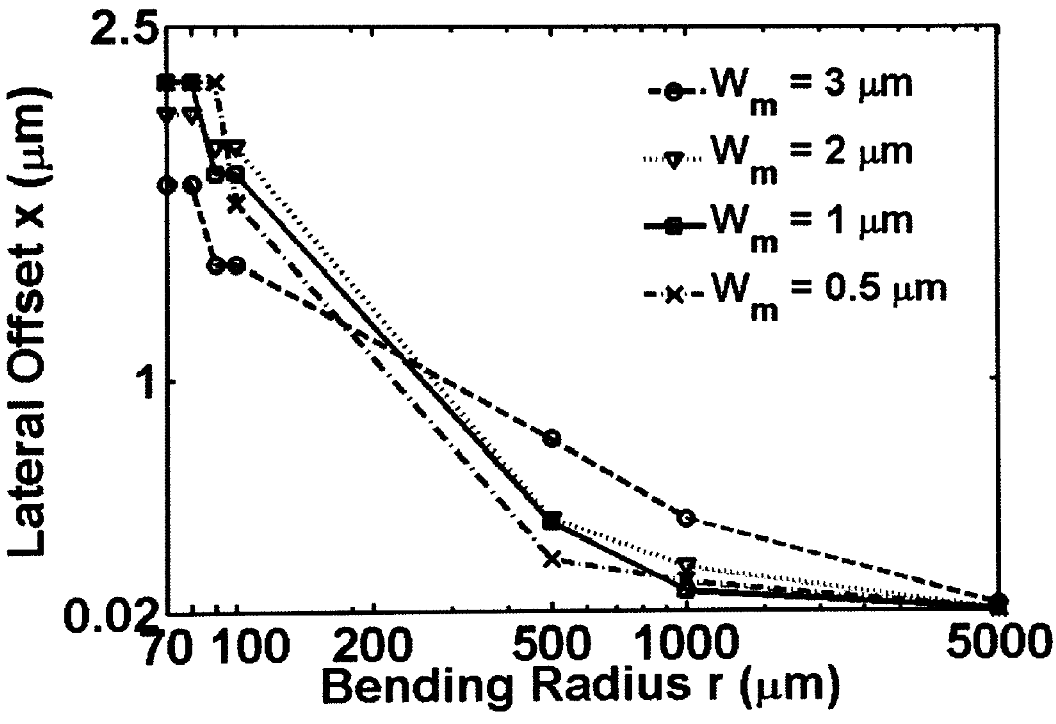

Figure 6.12 Variation of the optimum values of lateral offset x_{opt} with the bending radius r for different metal width W_m

Finally, coupling between straight hybrid waveguide and bent hybrid waveguide is investigated. As both waveguides are hybrid waveguides there is no need for vertical offset y. However, due to the bending effect the coupling efficiency between two waveguides is not optimum. This is because the field in the bent waveguide is shifted slightly from the centre towards the left side or right side depending on the bend direction. Therefore, a lateral offset x is needed in order to overcome this misalignment. Fig. 6.12 shows the variation of the optimum values of the lateral offset x_{opt} with the bending radius r at different metal widths W_m, 0.5, 1.0, 2.0, and 3.0 μm. It is revealed from this figure that as the bending radius r decreases the optimum lateral offset x_{opt} increases. However, at $r \leq r_{opt}$, x_{opt} starts to be constant as shown in Fig. 6.12. For the fabrication of the hybrid plasmonic, a thick SiO_2 is selected as substrate. After sputtering SiO_2 layer, a BCB layer with thickness h (μm) is fabricated by sputtering and plasma enhanced chemical vapor deposition (PECVD) methods. Then, a metal (Au) strips with different widths W_m are made by cover lithography, Au magnetic sputtering and lift-off process. Finally, another BCB layer is deposited on the top of the waveguide by sputtering and PECVD and the core width W_r is formed by UV lithography and reactive ion etching [111].

6.6 Summary

In this chapter a novel hybrid plasmonic waveguide with high index Si cap has been presented. Such waveguide can be integrated on electronic chip and it provides a good matching interface between conventional dielectric waveguides and electronic circuits. Also, this waveguide has small bending radius with small bending loss. Using the high index Si cap in such waveguide decrease the metal damping loss and provide better performance. Finally, the coupling characteristic of the hybrid waveguide has been studied. The maximum coupling between the dielectric waveguide and the straight hybrid plasmonic waveguide can be utilized by changing the vertical offset y. While, coupling between the straight hybrid plasmonic waveguide and the bent one can be maximised by changing the literal offset x.

Chapter 7

Conclusion and Future Research Directions

7.1 Conclusion

In this thesis, the investigation has been focused on the numerical modelling in frequency domain for plasmonic waveguide and its application. Objectives that have been presented in Chapter 1 have been satisfied as follow:

a. A novel graded nonuniform orthogonal mesh has been introduced and this kind of mesh enables accurate model of metallic nanostructures surrounded by dielectric mirostructures.
b. A full-vectorial finite difference mode solver that can deal with linear oblique and curved interfaces has been developed based on the novel graded nonuniform orthogonal mesh.
c. The mode solver capability for calculating calculate different parameters for that nanosturctures such as electromagnetic field component, effective index n_{eff}, propagation length L_{prop} and attenuation has been examined by studying different structures presented in chapter 5 and chapter 6.

d. The bending analysis for plasmonic waveguide has been presented in chapter 6 and the novel hybrid plasmonic waveguide that has been introduced shows a very small bending radius with a moderate bending loss.

e. Coupling characteristic for plasmonic waveguide has been introduced in chapter 6 and coupling coefficient can be maximised by align the plasmonic waveguide with conventional dielectric waveguide.

A novel three-trenched symmetric groove has been presented and analysed in chapter 5. Numerical simulation has been performed to analyse the reported structure, which reveals that it has a good confinement behaviour similar to the V-groove structure while it is easier in fabrication and design. In addition the propagation loss is better than that of the V-groove structure. Moreover, the FOM of suggested structure can be adjusted by controlling widths and depths of the three trenched groove. Therefore, the propagation length and the field confinement can be controlled and maximised using the reported structure.

In chapter 6, a novel design of hybrid long-range plasmonic waveguide is introduced and analysed using full-vectorial finite difference method. The reported design with high index material (Si) as a thin cap decreases the propagation loss, at bending radius $r > 1000$ μm, by 11-20% compared to without cap case at $W_m = 3$ μm. In addition, the propagation loss is decreased further by 41-86% compared to without cap case at small bending radius $r < 100$ μm and small metal width $W_m = 0.5$ μm. In addition, the optimum bending radius is reduced. The numerical results reveal that optimum bending radius, r_{opt} = 90 nm is achieved with Si cap while r_{opt}= 100 nm is obtained with BCB cap.

7.2 Future Research Directions

The application of the FDFD method to various theoretical test structures illustrated the accuracy and flexibility of the method. However, it would be beneficial to carry out a controlled experiment to further validate the method. This could be done, for example, by depositing various thicknesses of a lossy material, such as gold, onto a waveguide near the waveguide core. Deposition of a material layer that is very close to the core could be achieved using a side-polished fiber, or an integrated waveguide fabricated with a custom, thin cladding. The benefit of using the side-polished fiber would be that the geometry and distance to the core could be well characterised, and the thickness of each thin layer could be accurately measured, using ellipsometry for example. The insertion losses due to lossy layers of various thickness could be measured, and the comparison of these measurements to results obtained using the FDFD method would provide another verification of the accuracy of the method.

If the guided modes of a waveguide are of primary interest, the FDFD method is more appropriate, as the modes are directly solved without multiple propagation steps or post-processing. Another invaluable tool for waveguide analysis is the finite difference beam propagation method (FD-BPM). Whereas the FDTD method provides the "transient response" of a waveguide structure to a time-limited electromagnetic pulse, the BPM utilises a given input field to solve for the steady-state behaviour of an arbitrary waveguide, as long as the paraxial approximation holds. The major benefit of the BPM is that it clearly shows the evolution of the electromagnetic fields through waveguide junctions, discontinuities, or other structural variations along the direction of propagation. It would therefore be beneficial if the FD method could be integrated into a BPM algorithm. This would allow the study of the evolution of the fields and such phenomena as intermode coupling caused by the presence of the thin layers.

It would also be interesting to investigate alternative plasmonic sensor and coupler geometries. Coupled waveguide-cavity systems which are widely implemented in dielectric waveguide sensors could also be considered for plasmonic sensors.

Appendix

A. Maxwell's Equations

Maxwell's equations are a powerful tool to account for the propagating electromagnetic waves in dielectric media. There are mainly four electromagnetic field vectors that govern the electromagnetic phenomena. These four electromagnetic vectors describe the relationship between electric and magnetic fields that are function of both position r [m] and time t [s]. In their differential form, Maxwell's equations for EM propagating are written as:-

$$\nabla \times E = -\frac{\partial B}{\partial t} + M \tag{A.1}$$

$$\nabla \times H = \frac{\partial D}{\partial t} + J \tag{A.2}$$

$$\nabla . D = \rho \tag{A.3}$$

$$\nabla . B = 0 \tag{A.4}$$

where E is the vectorial electric field, in V/m, H is the vectorial magnetic field, in A/m, D is the electric flux density, in Coul/m^2, B is magnetic flux density, in Wb/m^2, M is the (fictitious) equivalent magnetic current density, in V/ m^2, J is the current density, in A/m^2, ρ is the free charge density, in Coul/m^3.

The physical background behind theses equations is that according to (A.1) the origin of the electrical field vortices ($\nabla \times E$) is the time-dependent change of magnetic field (

$-\partial B/\partial t$). At the same time as (A.2), the magnetic field vortices ($\nabla \times H$) can be either time-dependent change of the electric flux density ($\partial D/\partial t$) or a result of the current density in the material (J).

In order for a linear, homogeneous, and isotropic medium, the following constitutive relations are written

$$B = \mu H \tag{A.5}$$

$$D = \varepsilon E \tag{A.6}$$

$$J = \sigma E \tag{A.7}$$

$$M = \sigma^* H \tag{A.8}$$

where ϵ is the dielectric permittivity, in F/m, μ is the magnetic permeability of the medium, in H/m, σ is the electric conductivity, in S/m, σ^* is the equivalent magnetic loss, in Ω/m.

By handling equations (A.1) and (A.2), the following system of six scalar equations in Cartesian coordinate are obtained from Maxwell's equations for electromagnetic propagation theory, as expressed below:-

$$\frac{\partial E_x}{\partial t} = \frac{1}{\varepsilon}\left(\frac{\partial H_z}{\partial y} - \frac{\partial H_y}{\partial z} - \sigma E_x\right) \tag{A.9}$$

$$\frac{\partial E_y}{\partial t} = \frac{1}{\varepsilon}\left(\frac{\partial H_x}{\partial z} - \frac{\partial H_z}{\partial x} - \sigma E_y\right) \tag{A.10}$$

$$\frac{\partial E_z}{\partial t} = \frac{1}{\varepsilon}\left(\frac{\partial H_y}{\partial x} - \frac{\partial H_x}{\partial y} - \sigma E_z\right) \tag{A.11}$$

$$\frac{\partial H_x}{\partial t} = \frac{1}{\mu}\left(\frac{\partial E_y}{\partial z} - \frac{\partial E_z}{\partial y} - \sigma^* H_x\right) \tag{A.12}$$

$$\frac{\partial H_y}{\partial t} = \frac{1}{\mu}\left(\frac{\partial E_z}{\partial x} - \frac{\partial E_x}{\partial z} - \sigma^* H_y\right) \tag{A.13}$$

$$\frac{\partial H_z}{\partial t} = \frac{1}{\mu}\left(\frac{\partial E_x}{\partial y} - \frac{\partial E_y}{\partial x} - \sigma^* H_z\right) \tag{A.14}$$

B. Finite Difference Frequency Domain

When deriving the finite difference equations, it is assumed that the dielectric tensor is piecewise uniform, with boundaries constrained to coincide with the finite difference grid points, as depicted in Fig. B.1. In addition, the spacing between mesh points need not be uniform. After some algebraic simplification, the finite difference operators representing A_{xx} and A_{xy} can be expressed in terms of the transverse magnetic fields at the point under consideration (P) and at the eight neighbouring grid points as follows

$$\begin{aligned}
&a_{xx}^{(NW)}H_x^{(NW)} + a_{xx}^{(N)}H_x^{(N)} + a_{xx}^{(NE)}H_x^{(NE)} + a_{xx}^{(W)}H_x^{(W)} + a_{xx}^{(P)}H_x^{(P)} + a_{xx}^{(E)}H_x^{(E)} + a_{xx}^{(SW)}H_x^{(SW)} \\
&+ a_{xx}^{(S)}H_x^{(S)} + a_{xx}^{(SE)}H_x^{(SE)} + a_{xy}^{(NW)}H_y^{(NW)} + a_{xy}^{(N)}H_y^{(N)} + a_{xy}^{(NE)}H_y^{(NE)} + a_{xy}^{(W)}H_y^{(W)} + a_{xy}^{(P)}H_y^{(P)} \\
&+ a_{xy}^{(E)}H_y^{(E)} + a_{xy}^{(SW)}H_y^{(SW)} + a_{xy}^{(S)}H_y^{(S)} + a_{xy}^{(SE)}H_y^{(SE)} = \beta^2 H_x^{(P)}
\end{aligned} \tag{B.1}$$

and similarly for A_{yx} and A_{yy}

$$a_{yx}^{(NW)}H_x^{(NW)} + a_{yx}^{(N)}H_x^{(N)} + a_{yx}^{(NE)}H_x^{(NE)} + a_{yx}^{(W)}H_x^{(W)} + a_{yx}^{(P)}H_x^{(P)} + a_{yx}^{(E)}H_x^{(E)} + a_{yx}^{(SW)}H_x^{(SW)}$$
$$+ a_{yx}^{(S)}H_x^{(S)} + a_{yx}^{(SE)}H_x^{(SE)} + a_{yy}^{(NW)}H_y^{(NW)} + a_{yy}^{(N)}H_y^{(N)} + a_{yy}^{(NE)}H_y^{(NE)} + a_{yy}^{(W)}H_y^{(W)} + a_{yy}^{(P)}H_y^{(P)}$$
$$+ a_{yy}^{(E)}H_y^{(E)} + a_{yy}^{(SW)}H_y^{(SW)} + a_{yy}^{(S)}H_y^{(S)} + a_{yy}^{(SE)}H_y^{(SE)} = \beta^2 H_x^{(P)} \qquad \text{(B.2)}$$

The expressions for the finite difference coefficients a_{jk} are summarised as follows

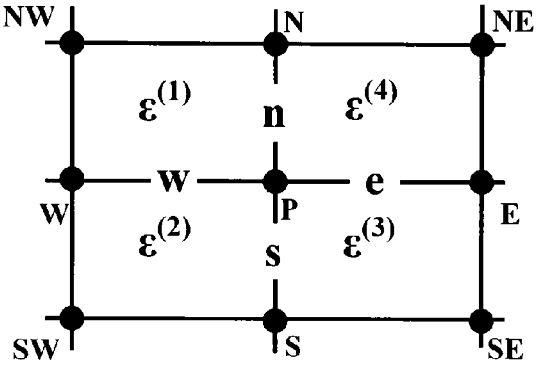

Figure B.1 The mesh points used in the finite difference equations . The superscripts P, N, S, E, W, NW, NE, SW, SE are used to label the point under consideration and its nearest neighbours to the north, south, east, west, northwest, northeast, southwest and southeast, respectively. The quantities n, s, e, and w denote the distance between P and the nearest mesh points in the north, south, west and east directions, respectively. The symbols $\varepsilon^{(1)}$, $\varepsilon^{(2)}$, $\varepsilon^{(3)}$ and $\varepsilon^{(4)}$ indicate the dielectric permittivity tensors, which are assumed to be homogeneous within each rectangular region between mesh points.

$$a_{xx}^{(N)} = \frac{\varepsilon_{yy}^{(3)}}{\varepsilon_{zz}^{(4)}} \frac{2e\varepsilon_{yy}^{(4)} - n\varepsilon_{yx}^{(4)}}{v_{34}n(e+w)} + \frac{\varepsilon_{yy}^{(2)}}{\varepsilon_{zz}^{(1)}} \frac{2w\varepsilon_{yy}^{(1)} + n\varepsilon_{yx}^{(1)}}{v_{21}n(e+w)} \qquad \text{(B.3)}$$

$$a_{xx}^{(S)} = \frac{\varepsilon_{yy}^{(4)}}{\varepsilon_{zz}^{(3)}} \frac{2e\varepsilon_{yy}^{(3)} - s\varepsilon_{yx}^{(3)}}{v_{34}s(e+w)} + \frac{\varepsilon_{yy}^{(1)}}{\varepsilon_{zz}^{(2)}} \frac{2w\varepsilon_{yy}^{(2)} + s\varepsilon_{yx}^{(2)}}{v_{21}s(e+w)} \qquad \text{(B.4)}$$

$$a_{xx}^{(E)} = \frac{2}{e(e+w)} + \frac{\varepsilon_{yy}^{(4)}\varepsilon_{yx}^{(3)}/\varepsilon_{zz}^{(3)} - \varepsilon_{yy}^{(3)}\varepsilon_{yx}^{(4)}/\varepsilon_{zz}^{(4)}}{v_{34}(e+w)} \qquad \text{(B.5)}$$

$$a_{xx}^{(W)} = \frac{2}{w(e+w)} + \frac{\varepsilon_{yy}^{(2)}\varepsilon_{yx}^{(1)} / \varepsilon_{zz}^{(1)} - \varepsilon_{yy}^{(1)}\varepsilon_{yx}^{(2)} / \varepsilon_{zz}^{(2)}}{v_{21}(e+w)} \tag{B.6}$$

$$a_{xx}^{(NE)} = \frac{\varepsilon_{yx}^{(4)}\varepsilon_{yy}^{(3)}}{\varepsilon_{zz}^{(4)} v_{34}(e+w)} \tag{B.7}$$

$$a_{xx}^{(SE)} = \frac{-\varepsilon_{yx}^{(3)}\varepsilon_{yy}^{(4)}}{\varepsilon_{zz}^{(3)} v_{34}(e+w)} \tag{B.8}$$

$$a_{xx}^{(SW)} = \frac{\varepsilon_{yx}^{(2)}\varepsilon_{yy}^{(1)}}{\varepsilon_{zz}^{(2)} v_{21}(e+w)} \tag{B.9}$$

$$a_{xx}^{(NW)} = \frac{-\varepsilon_{yx}^{(1)}\varepsilon_{yy}^{(2)}}{\varepsilon_{zz}^{(1)} v_{21}(e+w)} \tag{B.10}$$

$$\begin{aligned} a_{xx}^{(P)} &= -a_{xx}^{(N)} - a_{xx}^{(S)} - a_{xx}^{(E)} - a_{xx}^{(W)} - a_{xx}^{(NE)} - a_{xx}^{(SE)} - a_{xx}^{(SW)} - a_{xx}^{(NW)} \\ &\quad + k^2 \frac{n+s}{e+w}\left(\varepsilon_{yy}^{(4)}\varepsilon_{yy}^{(3)} \frac{e}{v_{34}} + \varepsilon_{yy}^{(1)}\varepsilon_{yy}^{(2)} \frac{w}{v_{21}} \right) \end{aligned} \tag{B.11}$$

$$a_{xy}^{(N)} = \frac{\dfrac{s\varepsilon_{yy}^{(2)}\varepsilon_{yy}^{(4)}}{v_{21}v_{34}} - \dfrac{s\varepsilon_{yy}^{(1)}\varepsilon_{yy}^{(3)}}{v_{21}v_{34}} + \dfrac{\varepsilon_{yy}^{(3)}\varepsilon_{yy}^{(4)}}{\varepsilon_{zz}^{(4)}v_{34}} - \dfrac{\varepsilon_{yy}^{(4)}\varepsilon_{yy}^{(1)}}{\varepsilon_{zz}^{(1)}v_{21}}}{(e+w)} \tag{B.12}$$

$$a_{xy}^{(S)} = \frac{\dfrac{n\varepsilon_{yy}^{(2)}\varepsilon_{yy}^{(4)}}{v_{21}v_{34}} - \dfrac{n\varepsilon_{yy}^{(1)}\varepsilon_{yy}^{(3)}}{v_{21}v_{34}} + \dfrac{\varepsilon_{yy}^{(1)}\varepsilon_{yy}^{(2)}}{\varepsilon_{zz}^{(2)}v_{21}} - \dfrac{\varepsilon_{yy}^{(4)}\varepsilon_{yy}^{(3)}}{\varepsilon_{zz}^{(3)}v_{34}}}{(e+w)} \tag{B.13}$$

$$a_{xy}^{(E)}=\frac{\varepsilon_{yy}^{(4)}\left(1-\varepsilon_{yy}^{(3)}/\varepsilon_{zz}^{(3)}\right)-\varepsilon_{yy}^{(3)}\left(1-\varepsilon_{yy}^{(4)}/\varepsilon_{zz}^{(4)}\right)}{v_{34}(e+w)}-\frac{2}{e(e+w)^2}\times\left[\frac{nw\varepsilon_{yx}^{(1)}\varepsilon_{yy}^{(2)}}{\varepsilon_{zz}^{(1)}v_{21}}+\frac{sw\varepsilon_{yx}^{(2)}\varepsilon_{yy}^{(1)}}{\varepsilon_{zz}^{(2)}v_{21}}+\right.$$

$$\left.\frac{ne\varepsilon_{yx}^{(4)}\varepsilon_{yy}^{(3)}}{\varepsilon_{zz}^{(4)}v_{34}}+\frac{se\varepsilon_{yx}^{(3)}\varepsilon_{yy}^{(4)}}{\varepsilon_{zz}^{(3)}v_{34}}+\frac{w^2\varepsilon_{yy}^{(1)}\varepsilon_{yy}^{(2)}}{v_{21}}\left(\frac{1}{\varepsilon_{zz}^{(1)}}-\frac{1}{\varepsilon_{zz}^{(2)}}\right)+\frac{ew\varepsilon_{yy}^{(3)}\varepsilon_{yy}^{(4)}}{v_{34}}\left(\frac{1}{\varepsilon_{zz}^{(4)}}-\frac{1}{\varepsilon_{zz}^{(3)}}\right)\right]$$

(B.14)

$$a_{xy}^{(W)}=\frac{\varepsilon_{yy}^{(2)}\left(1-\varepsilon_{yy}^{(1)}/\varepsilon_{zz}^{(1)}\right)-\varepsilon_{yy}^{(1)}\left(1-\varepsilon_{yy}^{(2)}/\varepsilon_{zz}^{(2)}\right)}{v_{21}(e+w)}-\frac{2}{w(e+w)^2}\times\left[\frac{ne\varepsilon_{yx}^{(4)}\varepsilon_{yy}^{(3)}}{\varepsilon_{zz}^{(4)}v_{34}}+\frac{se\varepsilon_{yx}^{(3)}\varepsilon_{yy}^{(4)}}{\varepsilon_{zz}^{(3)}v_{34}}\right.$$

$$\left.+\frac{nw\varepsilon_{yx}^{(1)}\varepsilon_{yy}^{(2)}}{\varepsilon_{zz}^{(1)}v_{21}}+\frac{sw\varepsilon_{yx}^{(2)}\varepsilon_{yy}^{(1)}}{\varepsilon_{zz}^{(2)}v_{21}}+\frac{e^2\varepsilon_{yy}^{(4)}\varepsilon_{yy}^{(3)}}{v_{34}}\left(\frac{1}{\varepsilon_{zz}^{(3)}}-\frac{1}{\varepsilon_{zz}^{(4)}}\right)+\frac{ew\varepsilon_{yy}^{(2)}\varepsilon_{yy}^{(1)}}{v_{12}}\left(\frac{1}{\varepsilon_{zz}^{(2)}}-\frac{1}{\varepsilon_{zz}^{(1)}}\right)\right] \tag{B.15}$$

$$a_{xy}^{(NE)}=\frac{\varepsilon_{yy}^{(3)}-\dfrac{\varepsilon_{yy}^{(3)}\varepsilon_{yy}^{(4)}}{\varepsilon_{zz}^{(4)}}}{v_{34}(e+w)} \tag{B.16}$$

$$a_{xy}^{(SE)}=\frac{\dfrac{\varepsilon_{yy}^{(4)}\varepsilon_{yy}^{(3)}}{\varepsilon_{zz}^{(3)}}-\varepsilon_{yy}^{(4)}}{v_{34}(e+w)} \tag{B.17}$$

$$a_{xy}^{(NW)}=\frac{\dfrac{\varepsilon_{yy}^{(2)}\varepsilon_{yy}^{(1)}}{\varepsilon_{zz}^{(1)}}-\varepsilon_{yy}^{(2)}}{v_{21}(e+w)}$$

(B.18)

$$a_{xy}^{(SW)}=\frac{\varepsilon_{yy}^{(1)}-\dfrac{\varepsilon_{yy}^{(1)}\varepsilon_{yy}^{(2)}}{\varepsilon_{zz}^{(2)}}}{v_{21}(e+w)} \tag{B.19}$$

$$a_{xy}^{(P)} = -a_{xy}^{(N)} - a_{xy}^{(S)} - a_{xy}^{(E)} - a_{xy}^{(W)} - a_{xy}^{(NE)} - a_{xy}^{(SE)} - a_{xy}^{(SW)} - a_{xy}^{(NW)}$$
$$-k^2\left(\frac{w(n\varepsilon_{yx}^{(1)}\varepsilon_{yy}^{(2)} + s\varepsilon_{yx}^{(2)}\varepsilon_{yy}^{(1)})}{v_{21}(e+w)} + \frac{e(s\varepsilon_{yx}^{(3)}\varepsilon_{yy}^{(4)} + n\varepsilon_{yx}^{(4)}\varepsilon_{yy}^{(3)})}{v_{34}(e+w)}\right) \tag{B.20}$$

$$v_{21} = n\varepsilon_{yy}^{(2)} + s\varepsilon_{yy}^{(1)} \tag{B.21}$$

$$v_{34} = n\varepsilon_{yy}^{(3)} + s\varepsilon_{yy}^{(4)} \tag{B.22}$$

The remaining 18 finite difference coefficients describing A_{yx} and A_{yy} can be obtained by applying the following transformations to (B.1)–(B.22)

$$x \leftrightarrow y$$
$$n, N \leftrightarrow e, E$$
$$s, S \leftrightarrow w, W$$
$$\varepsilon^{(3)} \leftrightarrow \varepsilon^{(1)}$$
$$v_{21} = n\varepsilon_{yy}^{(2)} + s\varepsilon_{yy}^{(1)} \rightarrow h_{23} = e\varepsilon_{xx}^{(2)} + w\varepsilon_{xx}^{(3)}$$
$$v_{34} = n\varepsilon_{yy}^{(3)} + s\varepsilon_{yy}^{(4)} \rightarrow h_{14} = e\varepsilon_{xx}^{(1)} + w\varepsilon_{xx}^{(4)} \tag{B.23}$$

If $\varepsilon_{xx} = \varepsilon_{yy} = \varepsilon_{zz} = \varepsilon$ and $\varepsilon_{xy} = \varepsilon_{yx} = 0$, these finite difference equations will be reduced to those of isotropic waveguide.

References

[1] M. T. Bohr, "Interconnect Scaling–The Real Limiter to High Performance ULSI," Tech. Dig. IEDM. 95, 241–244 (1995).

[2] K. Banerjee, A. Amerasekera, G. Dixit, and C. Hu, "The effect of interconnect scaling and low-k dielectric on the thermal characteristics of the IC metal," Tech. Dig. IEDM. 96, 65-68 (1996).

[3] H. Raether, "Surface Plasmons on Smooth and Rough Surfaces and on Gratings", (Springer, 1998).

[4] E. N. Economou, "Surface plasmons in thin films," Phys. Rev. 182, 539–554 (1969).

[5] M. Quinten, A. Leitner, J. R. Krenn, and F. R. Aussenegg, "Electromagnetic energy transport via linear chains of silver nanoparticles," Opt. Lett. 23, 1331–1333 (1998).

[6] S. A. Maier, P. G. Kik, H. A. Atwater, S. Meltzer, E. Harel, B. E. Koel, and A. A. G. Requicha, "Local detection of electromagnetic energy transport below the diffraction limit in metal nanoparticle plasmon waveguides," Nat. Mater. 2, 229–232 (2003).

[7] S. I. Bozhevolnyi, V. S. Volkov, E. Devaux, J. Y. Laluet, and T. W. Ebbesen, "Channel plasmon subwavelength waveguide components including interferometers and ring resonators," Nature 440, 508–511 (2006).

[8] M. Yan and M. Qiu, "Guided plasmon polariton at 2D metal corners," J. Opt. Soc. Am. B. 24, 2333–2342 (2007).

[9] A. D. Boardman, G. C. Aers, and R. Teshima, "Retarded edge modes of a parabolic wedge," Phys. Rev. B. 24, 5703–5712 (1981).

[10] G. Veronis and S. Fan, "Bends and splitters in subwavelength metal-dielectricmetal plasmonic waveguides," Appl. Phys. Lett. 87, 131102 (2005).

[11] J. S. White, G. Veronis, Z. Yu, E. S. Barnard, A. Chandran, S. Fan, and M. L. Brongersma, "Extraordinary optical absorption through subwavelength slits," Opt. Lett. 34, 686–688 (2009).

[12] W. L. Barnes, A. Dereux, and T. W. Ebbesen, "Surface plasmon subwavelength optics," Nature 424, 824–830 (2003).

[13] R. Zia, J. A. Schuller, A. Chandran, and M. L. Brongersma, "Plasmonics: the next chip-scale technology," Materials Today 9, 20–27 (2006).

[14] E. Ozbay, "Plasmonics: Merging photonics and electronics at nanoscale dimensions," Science 311, 189–193 (2006).

[15] S. A. Maier and H. A. Atwater, "Plasmonics: localization and guiding of elec-tromagnetic energy in metal/dielectric structures," J. Appl. Phys. 98, 011101 (2005).

[16] Maier, "Plasmonics: metal nanostructures for subwavelength photonic devices," IEEE J. Sel. Topics Quantum Electron., vol. 12, pp. 1214-1220, 2006.

[17] R. Zia, M. D. Selker, P. B. Catrysse and M. L. Brongersma, "Geometries and

materials for subwavelength surface plasmon modes," J. Opt. Soc. Amer. A, vol. 21, pp. 2442-2446, 2004.

[18] J. Takahara, S. Yamagishi, H. Taki, A Morimoto and T. Kobayashi, "Guiding of a one-dimensional optical beam with nanometer diameter," Optics Lett., vol. 22, pp. 475-477, 1997.

[19] T. W. Koo, S. Chan and A. A. Berlin, "Single-molecule detection of biomolecules by surface-enhanced coherent anti-stokes raman scattering," Optics Lett., vol. 30, pp. 1024-1026, 2005.

[20] B. Rothenhausler and W. Knoll, "Surface-plasmon microscopy," Nature, vol. 232, pp. 615-617, 1998.

[21] Z. Liu, Y. Wang, J. Yao, H. Lee, W. Srituravanich and X. Zhang, "Broad band two-dimensional manipulation of surface plasmons," Nano Lett., vol. 9, pp. 462-466, 2009.

[22] S. Maier, M. L. Brongersma, P. G. Kik, S. Meltzer, A. A. G. Requicha and H. A. Atwater, "Plasmonics- a route to nanoscale optical devices," Adv. Mater., vol. 13, pp. 1501-1505, 2001.

[23] K. H. Yoon, M. L. Shuler and S. J. Kim, "Design optimization of nano-grating surface plasmon resonance sensors," Optics Express, vol. 14, pp. 4842-4849, 2006.

[24] J. J. Burke, G. I Stegeman, T Tamir, "Surface-plasmon-like waves guided by thin, lossy metal lms," Phys. Rev. B, vol. 33, pp. 5186-5201, 1986.

[25] S. J. Al-Bader and M. Imtaar, "Azimuthally uniform surface-plasma modes

in thin metallic cylindrical shells," IEEE J. Quantum Electron., vol. 28, pp. 525-533, 1992.

[26] S. J. Al-Bader and M. Imtaar "Optical fiber hybrid-surface plasmon polaritons," J. Opt. Soc. Am. B, vol. 10, pp. 83-88, 1993.

[27] P. Berini, "Optical waveguide structures," U.S. patent 6,741,782, May 25, 2004.

[28] M. S. Tomas and Z. Lenac, "Long-range surface polaritons in a supported thin metallic slab," Solid State Commun., vol. 50, pp. 915-918, 1984.

[29] M.S. Tomaš, Z. Lenac "Coupled surface polariton with guided wave polariton modes in asym-metric metal clad dielectric waveguides," Opt. Commun., vol. 55, pp. 267-270, 1985.

[30] Z. Lenac and M. S. Tomas, "Attenuation of long-range surface polaritons in a thin metallic slab with a dielectric coating," Surf. Sci., vol. 154, pp. 639-657, 1985.

[31] F. Yang, Z. Cao, L. Ruan, and J. Fang, "Long-range surface modes of metalclad four-layer waveguides," Appl. Opt., vol. 25, pp. 3903-3908, 1986.

[32] J. Guo and R. Adato, "Extended long range plasmon waves in nite thickness metal lm and layered dielectric materials," Opt. Express, vol. 14, pp. 12 409-12 418, 2006.

[33] R. Adato and J. Guo, "Characteristics of ultra-long range surface plasmon waves at optical frequencies," Opt. Express, vol. 15, pp. 5008-5017, 2007.

[34] J. T. Kim, "Characteristics analysis of hybrid plasmonic waveguide for low-

loss lightwave guiding," Opt. Commun., May 2011.

[35] B. Yun, G. Hu, and Y. Cui, "Bound modes analysis of symmetric dielectric loaded surface plasmon-polariton waveguides," Opt. Express, vol. 17, pp. 3610-3618, 2009.

[36] P. Berini, "Plasmon-polariton modes guided by a metal film of finit width bounded by different dielectrics," Opt. Express, vol. 7, pp. 329-335, 2000.

[37] P. Berini, "Plasmon-polariton waves guided by thin lossy metal films of finit width: bound modes of asymmetric structures," Phys. Rev. B, vol. 63, p. 125417, 2001.

[38] P. Berini, "Plasmon-polariton modes guided by a metal film of finit width," Opt. Lett., vol. 24, pp. 1011-1013, 1999.

[39] P. Berini, "Plasmon-polariton waves guided by thin lossy metal films of finite width: bound modes of symmetric structures," Phys. Rev. B, vol. 61, pp. 10 484-10 503, 2000.

[40] R. Charbonneau, P. Berini, E. Berolo, and E. Lisicka-Skrzek, "Experimental observation of plasmon-polariton waves supported by a thin metal film of finit width," Opt. Lett., vol. 25, pp. 844-846, 2000.

[41] A. Degiron, C. Dellagiacoma, J. C. McIlhargey, G. Shvets, O. J. F. Martin, and D. R. Smith, "Simulations of hybrid long-range plasmon modes with application to 90 bends," Opt. Lett., vol. 32, pp. 2354-2356, 2007.

[42] J. Guo and R. Adato, "Control of 2d plasmon-polariton mode with dielectric nanolayers," Opt. Express, vol. 16, pp. 1232-1237, 2008.

[43] R. Adato and J. Guo, “Modication of dispersion, localization, and attenuation of thin metal stripe symmetric surface plasmon-polariton modes by thin dielectric layers," J. Appl. Phys., vol. 105, p. 034306, 2009.

[44] J. Gosciniak, T. Holmgaard, and S. I. Bozhevolnyi, “Theoretical analysis of long-range dielectric-loaded surface plasmon polariton waveguides," OSA/IEEE J. Lightw. Tachnol., vol. 29, pp. 1473-1481, 2011.

[45] A. B. Fallahkhair, K. S. Li, and T. E. Murphy, "Vector Finite Difference Mode solver for Anisotropic Dielectric Waveguides," J. Lightwave Technol., vol. 26 (11), pp. 1423-1431, 2008.

[46] S. S. A. Obayya, B. M. A. Rahman, and K. T. V. Grattan, "Accurate finite element modal solution of photonic crystal fibres. Optoelectronics," IEE Proceedings vol. 152, pp. 241- 246, 2005.

[47] S. Campbell, R. C. McPhedran, C. Martijn de Sterke, and L. C. Botten, "Differential multipole method for microstructured optical fibers," J. Opt. Soc. Am. B., vol. 21(21), pp. 1919-1928, 2004.

[48] C. A. De Francisco, B. V. Borges, and M. A. Romero, "A Semivectorial method for the modeling of photonic crystal fibers," Microwave Opt. Technol Lett., vol. 38(5), pp. 418–421, 2003.

[49] S. S. A. Obayya, B. M. Azizur Rahman, Kenneth T. V. Grattan, and H. A. El-Mikati, "Full Vectorial Finite-Element-Based Imaginary Distance Beam Propagation Solution of Complex Modes in Optical Waveguides," J. Lightwave Technol. , vol. 20, p. 1054, 2002.

[50] S. A. Maier, Plasmonics: Fundamentals and Applications (Springer, New York, 2007).

[51] L. Novotny, B. Hecht, and D. W. Pohl,"Interference of locally excited surface plasmons," J. Appl. Phys. 81, 1798–1806 (1997).

[52] E. Prodan, P. Nordlander, and N. J. Halas, "Effects of dielectric screening on the optical properties of metallic nanoshells," Chem. Phys. Lett. 368, 94–101 (2003).

[53] C. F. Bohren, D. R. Huffman, Absorption and Scattering of Light by Small Particles, (Wiley, New York, 1983).

[54] E. D. Palik, Handbook of Optical Constants of Solids, (Academic, New York, 1985).

[55] A. Taflove, Computational Electrodynamics, (Artech House, Boston, 1995).

[56] A. D. Rakic, A. B. Djurisic, J. M. Elazar, and M. L. Majewski,"Optical properties of metallic films for vertical cavity optoelectronic devices," Appl. Opt. 37, 5271–5283 (1998).

[57] A. Vial, A. S. Grimault, D. Macias, D. Barchiesi, and M. L. De la Chapelle, "Improved analytical fit of gold dispersion: application to the modeling of extinction spectra with a finite-difference time-domain method," Phys. Rev. B. 71, 85416 (2005).

[58] J. D. Jackson, Classical Electrodynamics, (Wiley, New York, 1999).

[59] J. Jin, The Finite Element Method in Electromagnetics, (Wiley, New York, 2002).

[60] J. Berenger, "A perfectly matched layer for the absorption of electromagnetic waves," Journal of Computational Physics, vol. 114, pp. 185–200, 1994.

[61] S. D. Gedney, "An anisotropic perfectly matched layer absorbing media for the truncation of FDTD latices," Antennas and Propagation, IEEE Transactions, vol. 44, pp. 1630–1639, 1996.

[62] W. C. Chew and W. H. Weedon, "A 3d perfectly matched medium from modified Maxwell's equations with stretched coordinates," Microwave Optical Tech. Letters, vol. 7, pp. 590–604, 1994.

[63] W. C. Chew, J. M. Jin, and E. Michielssen, "Complex Coordinate Stretching as a Generalized Absorbing Boundary Condition," Microwave and Opt. Technol. Lett., vol. 15(6), pp. 363–369, 1997.

[64] J. L. Young and R. O. Nelson, "A summary and systematic analysis of FDTD algorithms for linearly dispersive media," IEEE Antennas Propag. Mag. 43, 61–77 (2001).

[65] M. N. O. Sadiku, Numerical Techniques in Electromagnetics, (CRC Press, Boca Raton, 2001).

[66] P. Monk and E. Suli, "A convergence analysis of Yee's scheme on non-uniform grids,"SIAM J. Num. Analysis, vol. 31, pp. 393–412, 1994.

[67] P. Monk, "Error estimates for Yee's method on non-uniform grids,"IEEE Trans. Magnetics, vol. 30, pp. 3200–3203, 1994.

[68] M. J. Berger and J. Oliger, "Adaptive mesh refinement for hyperbolic partial differential equations,"J. Comp. Phys., vol. 53, pp. 484–512, 1984.

[69] J. F. Thompson, B. K. Soni, and N. P. Weatherill, Eds., Handbook of Grid Generation. CRC Press, 1999.

[70] M. S. Stern, "Semivectorial polarized finite difference method for optical waveguides with arbitrary index profiles," Proc. Inst. Elect. Eng., pt. J, vol. 135, pp. 56–63, 1988.

[71] C. Vassallo, "Improvement of finite difference methods for step-index optical waveguides," Proc. Inst. Elect. Eng., pt. J, vol. 139, pp. 137–142, 1992.

[72] J. Yamauchi, M. Sekiguchi, O. Uchiyama, J. Shibayama, and H. Nakano, "Modified finite-difference formula for the analysis of semivectorial modes in step-index optical waveguides," IEEE Photon. Technol. Lett., vol. 9, pp. 961–963, July, 1997.

[73] A. P. Ansbro and I. Montrosset, "Vectorial finite difference scheme for isotropic dielectric waveguides: Transverse electric field representation," Proc. Inst. Elect. Eng., pt. J, vol. 140, pp. 253–259, 1993.

[74] C. L. Xu,W. P. Huang, M. S. Stern, and S. K. Chaudhuri, "Full-vectorial mode calculations by finite difference method," Proc. Inst. Elect. Eng., pt. J, vol. 141, pp. 281–286, 1994.

[75] G. R. Hadley and R. E. Smith, "Full-vector waveguide modeling using an iterative finite-difference method with transparent boundary conditions,"J. Lightwave Technol., vol. 13, pp. 465–469, Mar. 1995.

[76] S. Sujecki, T. M. Benson, P. Sewell, and P. C. Kendall, "Novel vectorial analysis of optical waveguides," J. Lightwave Technol., vol. 16, pp. 1329–

1335, July 1998.

[77] J. Yamauchi, G. Takahashi, and H. Nakano, "Full-vectorial beam-propagation method based on the McKee-Mitchell scheme with improved finite-difference formulas," J. Lightwave Technol., vol. 16, pp. 2458–2464, Dec. 1998.

[78] Y. P. Chiou, Y. C. Chiang, and H. C. Chang, "Improved three-point formulas considering the interface conditions in the finite-difference analysis of step-index optical devices," J. Lightwave Technol., vol. 18, pp. 243–251, Feb., 2000.

[79] L. Dobrzynski, A.A. Maradudin, "Electrostatic Edge Modes in a Dielectric Wedge," Phys. Rev. B 6, 3810. (1972)

[80] I. V. Novikov and A. A. Maradudin, "Channel polaritons," Phys. Rev. B 66, 035403 (2002).

[81] L. C. Davis, "Electrostatic edge modes of a dielectric wedge," Phys. Rev. B 14, 5523-5525 (1976)

[82] A. Eguiluz, A.A. Maradudin, "Electrostatic edge modes along a parabolic wedge," Phys. Rev. B 14, 5526. (1976)

[83] A.D. Boardman, R. Garcia–Molina, A. Gras–Marti, E. Louis, "Electrostatic edge modes of a hyperbolic dielectric wedge: Analytical solution," Phys. Rev. B 32, 6045 (1985).

[84] D. K. Gramotnev, "Adiabatic nanofocusing of plasmons by sharp metallic grooves: Geometrical optics approach," J. Appl. Phys. 98, 104302 (2005).

[85] S. I. Bozhevolnyi, "Effective-index modeling of channel plasmon polaritons," Opt. Express 14, 9467-9476 (2006)

[86] D. K. Gramotnev and K. C. Vernon, "Adiabatic nano-focusing of plasmons by sharp metallic wedges," Appl. Phys. B 86, 7-17 (2007)

[87] S. I. Bozhevolnyi, V.S. Volkov, E. Devaux and T.W. Ebbesen "Channel plasmon-polariton guiding by subwavelength grooves" Phys. Rev. Lett. 95, 046802 (2005)

[88] C. Hafner, Post-Modern Electromagnetics (Wiley, Chichester, 1999).

[89] E. Moreno, S. G. Rodrigo, S. I. Bozhevolnyi, L. Martín-Moreno, and F. J. García-Vidal, "Guiding and focusing of electromagnetic fields with wedge plasmon polaritons," Phys. Rev. Lett. 100, 023901 (2008).

[90] E. Moreno, F. J. Garcia-Vidal, S. G. Rodrigo, L. Martin-Moreno, and S. I. Bozhevolnyi, "Channel plasmonpolaritons: modal shape, dispersion, and losses," Opt. Lett., vol.31, pp.3447-344, 2006

[91] K. Tananka, M. Tanaka, "Simulations of nanometric optical circuits based on surface plasmon polariton gap waveguide," Appl. Phys. Lett., vol. 82, pp.1158-1160, 2003.

[92] D. K. Gramotnev, and D. F. P. Pile, "Single-mode subwavelength waveguide with channel plasmonpolaritons in triangular grooves on a metal surface," Appl. Phys. Lett. 85, 6323-6325 (2004).

[93] D. K. Gramotnev and S. I. Bozhevolnyi, "Plasmonics beyond the diffraction limit", Nat. Photonics, vol. 4, pp.83-91, 2010

[94] J. Pan, K. He, Z. Chen, Z. Wang "Realization of subwavelength guiding utilizing coupled wedge plasmon polaritons in splitted groove waveguides" Optics Express, Vol. 18, Issue 16, pp. 16722-16732, 2010 .

[95] M. Wu, Z. Han, and V. Van, "Conductor-gap-silicon plasmonic waveguides and passive components at subwavelength scale", Opt. Express, vol. 18, pp.11728-11736, 2010.

[96] S. Y. Zhu, T. Y. Liow, G. Q. Lo, and D. L. Kwong, "Silicon-based horizontal nanoplasmonic slot waveguides for on-chip integration", Opt. Express, vol. 19, pp.8888- 8902, 2011.

[97] X. Li, T. Jiang, L. Shen, X. Zheng, "Channel Plasmon Polaritons Guiding by a Partial-Dielectric-Loaded Metallic Groove", IEEE Photonics Technology Letters, vol. 24, no. 24, 2012.

[98] I. Avrutsky, R. Soref, and W. Buchwald, "Sub-wavelength plasmonic modes in a conductor-gap-dielectric system with a nanoscale gap," Optics Express, Vol. 18, Issue 1, 348-363, 2010.

[99] Lee. Sangjun, Kim. Sangin " Plasmonic mode-gap waveguides using hetero-metal films " , Optics Express, vol. 18, issue 3, p. 2197, 2009.

[100] M. Kauranen & A. V. Zayats "Nonlinear plasmonics" Nature Photonics vol. 6, p. 737–748, 2012.

[101] W. Mu and J. B. Ketterson , "Long-range surface plasmon polaritons propagating on a dielectric waveguide support", Optics Letters, Vol. 36, Issue 23, pp. 4713-4715 (2011)

[102] Q. Min, C. Chen, P. Berini, and R. Gordon, "Long range surface plasmons on asymmetric suspended thin film structuresfor biosensing applications," Opt. Express 18, 19009-19019, 2010

[103] G. Magno, M. Grande, V. Petruzzelli, and A. D'Orazio," Numerical analysis of the coupling mechanism in long-range plasmonic couplers at 1.55 μm", Optics Letters, Vol. 38, Issue 1, pp. 46-48 , 2013.

[104] F. Kusunoki, T. Yotsuya, J. Takahara, and T. Kobayashi, "Propagation properties of guided waves in index-guided two-dimensional optical waveguides," Appl. Phys. Lett. 86, 211101-211103 , 2005.

[105] F. Kusunoki, T. Yotsuya, and J. Takahara, "Confinement and guiding of two-dimensional optical waves by low refractive-index cores," Opt. Express 14(12), 5651–5656, 2006.

[106] D. Dai and S. He "A silicon-based hybrid plasmonic waveguide with a metal cap for a nano-scale light confinement", Optics Express, Vol. 17, Issue 19, pp. 16646-16653 , 2009.

[107] J. Chen, Z. Li, S. Yue, and Q. Gong, "Hybrid long-range surface plasmon-polariton modes with tight field confinement guided by asymmetrical waveguides," Opt. Exp., vol. 17, pp. 23603–23609, 2009.

[108] A. V. Krasavin and A. V. Zayats, "Numerical analysis of long-range surface plasmon polariton modes in nanoscale plasmonic waveguides," Opt. Lett., vol. 35, pp. 2118–2120, 2010.

[109] R. F. Oulton, V. J. Sorger, D. A. Genov, D. F. P. Pile, and X. Zhang, "A hybrid plasmonic waveguide for subwavelength confinement and long-range propagation," Nature Photon., vol. 2, pp. 496–500, 2008.

[110] R. Salvador, A. Martinez, C. Garcia-Meca, R. Ortuno, and J. Marti, "Analysis of hybrid dielectric plasmonic waveguides," IEEE J. Sel. Topics Quantum Electron., vol. 14, no. 6, pp. 1496–1501, Nov.–Dec. 2008.

[111] L. Chen, X. Li, G. Wang; W. Li, S. Chen, L. Xiao, D. Gao, "A Silicon-Based 3-D Hybrid Long-Range Plasmonic Waveguide for Nanophotonic Integration" IEEE Journal of lightwave technology, Vol. 30, No. 1, 2012.

[112] Shoichi Kubo, Andres Diaz, Yan Tang, Theresa S. Mayer, Iam Choon Khoo, and Thomas E. Mallouk, "Tunability of the Refractive Index of Gold Nanoparticle Dispersions", Nano Letters, vol. 7, no. 11, pp. 3418-3423, 2007

[113] Marvin J. Weber, Handbook of Optical Materials (CRC 2003).

[114] P. Berini and J. Lu, "Curved long-range surface plasmon-polariton waveguides," Opt. Express 14, 2365–2371 (2006).

[115] C. Dellagiacoma, T. Lasser, O. J. F. Martin, A. Degiron, J. J. Mock, D. R. Smith, "Simulation of complex plasmonic circuits including bends," Optics Express, Vol. 19, Issue 20, pp. 18979-18988 (2011)